Driven flow of droplets and bubbles

Driven flow of droplets and bubbles

By Carmen L. Lee, B.Sc., M.Sc.

A Thesis Submitted to the School of Graduate Studies in the Partial Fulfillment of the Requirements for the Degree Doctor of Philosophy

McMaster University © Copyright by Carmen L. Lee B.Sc., M.Sc.
August 22, 2022

McMaster University
Doctor of Philosophy (2022)
Hamilton, Ontario (Physics and Astronomy)

TITLE: Driven flow of droplets and bubbles
AUTHOR: Carmen L. LEE (McMaster University)
SUPERVISOR: Dr. Kari DALNOKI-VERESS
NUMBER OF PAGES: xiii, 125

Abstract

The work contained in this thesis presents four research manuscripts concerning the flow and motion of drops and bubbles in different geometries.

The first project explores the geometry of a totally wetting droplet on a conical fiber. A droplet on a fiber undergoes spontaneous motion toward the base of the fiber due to capillary forces, and viscous dissipation opposes the motion. In the first paper (Chapter 3), it was found that balancing the viscous shear force with the driving capillary force describes the motion of the droplet along the fiber. However, in nature, if fibers are coated with a liquid, there is rarely one droplet present; the second paper (Chapter 4) studies a conical fiber coated with multiple droplets. A liquid film coating a fiber will break up into droplets and it is found that the spacing of droplets depends on the shape of the fiber. The merging of droplets was studied and the dynamics well matches numerical simulations. The third paper (Chapter 5) studies the fluid film that a droplet will leave behind as it moves along the fiber. Using asymptotic matching to film deposition theory, this study found that the film thickness is affected by the curvature of the droplet. These studies show that the conical geometry and droplet curvature play an important role in droplet motion and film deposition.

The last project (Chapter 6) in this thesis concerns a chain of uniform sticky bubbles that rise through an aqueous bath. It is found that the chain of bubbles will buckle regularly as it moves through a liquid bath, much like a solid rope will buckle when impacting a surface. As the bubble chain rises through the bath, a compressive force develops due to an imbalance between the buoyancy of the chain and the viscous drag of the liquid surrounding it. Unlike solid ropes, there is no bending to stabilize the bubble chain and the regular buckling pattern is unexpected. Using scaling arguments, it is found that the viscous bath both stabilizes the chain and introduces the compressive force. The geometry of the buckling can be described from a force balance between the compressive and stabilizing forces.

Drops and bubbles prove to be useful experimental tools to probe driven flow in different geometries and provide valuable insight into fundamental and applied physics systems.

Acknowledgements

A short acknowledgements section cannot do justice to the gratitude to those who have supported me during this degree, I appreciate all of you!

First, to Kari: you've been an academic supervisor, a teacher, a colleague, a mentor, and a friend. We joke in the lab about how you use words like 'fantastic' and 'phenomenal' liberally; but I think this sums up your endless enthusiasm for science and your unwavering support of your students. Thank you for always having my back when bringing progressive ideas to the department. You're a role model in mentorship. Thank you for indulging me in my endless project ideas. I have learned so much from you, thank you.

To the members of the KDV lab, both past and present, thank you for being fantastic colleagues: Adam, Lauren, Clementine, John, Johnathan, Hamza, Yasmin, Sara, Raffi, JC, and Ben. I will always remember the APS shenanigans, working together during a pandemic, and all the professional and personal chats in the lab. Thanks for putting up with me snooping around your projects! Additional thanks to the undergrad students that I've worked with over the last number of years. To members of PIPA, thank you for all of your hard work over the years. It's been a joy to work, push, discuss, and learn. I've grown so much and become a better person for it in our work together.

To my family, my parents, my brothers, and Nova, thank you for all of your love. Thank you to my Henry House sisters: Emma for being a ray of sunshine, Gill for answering my weird, late night animal questions and Jocelyn for being my buddy in anything to do with crafts. Thank you to my fellow grad students for commiserating with me and for finding joy in what we do (Jacqueline, Wyatt, Joey, James, Sarah, Blake, Claude, John and many more).

To Thanassis, thank you for being my partner and best friend. You've helped me through so many ups and downs, and you've been steadfast, unconditional support the whole way through. To many more adventures!

Love and thanks to you all.

Contents

List of Figures

For my family

Chapter 1

Introduction

1.1 Introduction

Fundamentally, this thesis falls into a category of dissertations that study fluid mechanics, which is easy because fluid mechanics is a broad field that spans length scales from galaxy dynamics all the way down to the flow of microscopic amoebae in a pond. The study of fluid mechanics is also easy to motivate because fluids, especially moving fluids, are all around us, from the air we breathe to the water in our drinking glass to blood flow in our veins. In addition, if fluid systems include components of self-assembly, pattern formation, mesoscopic system sizes, and if thermal energy is important, then the systems are part of the study of soft condensed matter. Soft matter is a multidisciplinary field that includes components of biophysics, granular physics, fluid mechanics, complex fluids, polymer physics, colloids, chemical physics, and many others [1].

At the intersection of fluid mechanics and soft matter, we must look no farther than some examples in nature to understand why this is such a rich area of physics. Dry sand behaves very differently than wet sand, as those who have tried to build a sandcastle know of the importance of adding water. The water in wet sand fills the volume between the grains, creating small capillary bridges that hold the particles and allow for an intrepid builder to create shapes that would revert to a pile without the presence of the liquid [2, 3]. Along with acting like glue, liquids can also act as a lubricating layer; snails, slugs and other gastropods secrete a mucus that not only prevents their desiccation, but also allows them to change the friction between their bodies and the surface upon which they are moving [4, 5]. Nature has also come up with clever ways to remove liquid from surfaces where it is not desired. For example, water striders rely on tiny hydrophobic hairs coating their legs to spontaneously repel water, a key feature that allows them to skate across the surface of a lake [6]. A combination of the hydrophobicity and the geometry of the hairs are responsible for this effect. Lotus leaves are famous for their hydrophobic nature causing raindrops to easily bead up and roll off the leaf surface [7, 8]. This thesis aims to follow examples given by nature to understand how droplets and bubbles form, move, and interact in different geometries.

Along with systems created in nature, there are many biological and technological applications that benefit from understanding droplets. Inkjet printing, for instance, relies on both the break up of a jet of liquid into droplets (see the Plateau-Rayleigh instability addressed in section 1.6.2) [9] and on the wetting of the ink on the paper (see section 1.3.3) [10, 11]. In our changing environment due to climate change, reliable potable water sources are an urgent necessity, and one possible solution is the development of fog harvesting devices. Fog harvesting is the act of catching moisture from the air, and many devices takes inspiration from water striders; however, rather than coating the hairs with a hydrophobic surface, the goal is to transport water towards the base of the hair faster than the water can evaporate [12, 13, 14]. Droplet interactions with slender bodies have also been of particular interest in recent literature, where droplets have been wrapped in slender sheets [15, 16, 17, 18], used to bend fibers [19, 20, 21, 22] and transported along surfaces of varying composition and structure [23, 24].

In this chapter, I will provide the relevant physics to understanding several interactions between fluids and materials. First I will start by broadly defining fluid dynamics and the governing equations in section 1.2, before examining what happens when the system length scale is decreased to the point when capillary forces dominate in section 1.3. I will briefly discuss ways of comparing forces to understand which forces are dominant in fluid systems in section 1.4. After laying the framework of the relevant physics concepts in the first three sections, I will derive the shapes of droplets in different geometries in section 1.5 which will be used in the later chapters that contain the research conducted for this doctoral thesis.

Specific interactions between capillarity and hydrodynamics will be presented in section 1.6, where the interplay between surface tension and viscosity can develop a coating of a liquid film and also facilitate a break up of a film. Sections 1.7 and 1.8 will show some applications of the physics learned in the previous sections including creating adhesive bubbles and coiling of slender structures. In chapter 2, I will discuss the experimental techniques used in this thesis including pipette pulling, droplet production, bubble production and image analysis.

The following chapters in this “sandwich thesis” will include four papers, three of the papers investigate a system of a droplet moving on a conical fiber. Chapter 3 discusses a simple surface tension driven model to describe the motion of a droplet on a conical fiber. The formation, motion and merging of these droplets is presented in Chapter 4 and Chapter 5 will discuss the relevant physics of the film left behind a droplet as it self-propels along a fiber. In a slight side-step away from droplets moving on fibers, in Chapter 6 we will take inspiration from both air bubbles in carbonated drinks, and the coiling of honey on toast. This final paper studies drag-induced buckling of a chain of bubbles. Finally, Chapter 7 will contain general conclusions.

1.2 Fluid dynamics

One of the beautiful things about physics is that you can usually start from first principles to come up with a set of equations that includes all the physics to describe a system. Sometimes the resulting equations are solvable, sometimes they are not. In fluid dynamics, we can describe the relevant phenomena using the Navier-Stokes equations. First, I will walk the reader through the general ingredients to the equations, and then discard the parts of the equation that are not relevant to topics in this thesis and subsequently simplify the mathematics. In this section, we will start off broadly with the Navier-Stokes equations before introducing assumptions and ways to simplify the equations into an analytically solvable form using the lubrication approximation. Relevant to the three papers presented in Chapters 3-5, the lubrication approximation describes the flow of a thin film of liquid on a solid surface. We see the effect of the lubrication approximation in a thin film when a droplet of fluid glides along the conical fiber because of the lubricating layer of a pre-wetting film. At the end of this section, I will explain the origins of viscous dissipation, which moderates the flow of the drops. Finally, I will derive viscous drag forces for objects moving through a fluid, like the air bubbles moving through an aqueous bath, as presented in Chapter 6.

1.2.1 Navier-Stokes equations

The Navier-Stokes equations are the most general set of equations that can be used to describe fluid flow. From compressible gases with turbulence to viscous liquids like honey or molasses, from ocean currents to the fluids in our cells, the Navier-Stokes covers it all [25]. The Navier-Stokes equations describe motion in three-dimensions and accounts for inertia, compressibility, pressure, gravity and more through two simple ideas: conservation of momentum and conservation of mass [25]. There is currently no general analytical solution for the Navier-Stokes equations and famously there is an award for those who discover the general solution [26].

The first relationship we will consider is the conservation of momentum. To begin deriving the Navier-Stokes equations for a fluid, it is informative to consider one small volume of the fluid at one point in time in a fluid body. At an instantaneous point in time, this infinitesimal section of fluid will behave as a confined volume. A volume of fluid will respond to any potential forces acting on it according to Newton's second law of motion [27]. Generally, a volume will have a force $\vec{F}$ acting on it, and it will respond with an acceleration $\vec{a}$ according to the mass m, which we can express in an equation that some may recognize from beginner physics courses,

$$\vec{F} = m\vec{a}. \tag{1.1}$$

This equation is incredibly general and based on the specifics of the system we can provide a more detailed analysis. Starting with the right-hand side of equation 1.1, any acceleration can be attributed to different changes in momentum, where momentum $\vec{p}$ is the mass of an object multiplied by the velocity. This means the right hand side of equation 1.1 can be rewritten to consider momentum $\vec{p}$, where $m\vec{a} = d\vec{p}/dt$, where for an unchanging density ρ and volume V, the momentum changes as a function of time t. The first type of momentum to consider is the change in momentum of the parcel itself, just like if the parcel were a block being pushed along a surface beginning from rest. We will refer to this as the *variational term*$= \rho\partial\vec{u}/\partial t$ expressed per unit volume, where $\vec{u}$ is the three-dimensional velocity of the parcel, and t is time. Another momentum component to consider is the momentum change due to the fluid surrounding the parcel, which is similar to the idea of a stick floating down a river. The stick moves and changes direction according to the flow of the river rather than the internal inertia of the stick. In a similar argument, because the parcel is passing along a streamline through the fluid, the passing fluid also carries momentum, this is known as the *convective term* $= \rho\left(\vec{u}\cdot\nabla\right)\vec{u}$ per unit volume. The convective term is non-linear in $\vec{u}$ and can make calculations difficult.

To understand the left-hand side of equation 1.1, we can consider the forces that the parcel might be experiencing, both internally and externally. One of the forces that can act on the fluid parcel is an internal force, meaning it results not from an external source, but from stresses inside of the fluid body. One of these internal forces is from pressure gradients that can arise in the fluid, a common surface related pressure is discussed in section 1.3.4. Any difference in pressure P across the fluid body will cause flow. Fluid flows from high to low pressure, just like air does when you inhale. When you expand your chest to inhale, you are increasing the volume available in your chest and thus decreasing the pressure relative to atmospheric pressure. The pressure difference between your expanded chest and the atmosphere causes to air flow into your lungs. Flow due to pressure differences will be referred to as *pressure driven* $= \nabla P$ per volume of liquid.

Another internal force present in a liquid is the viscous dissipation. In this case, viscosity opposes any motion that the parcel might be feeling due to friction between the liquid particles. Viscosity is the way that a liquid resists motion and is often indicated with a viscous coefficient η. The origins and specifics of viscosity are discussed in section 1.2.4 because it is particularly relevant to this thesis. The viscosity term will oppose motion and will be referred to as *viscous dissipation* $= -\eta\nabla^2\vec{u}$ per volume of fluid.

Any external forces, like gravity or magnetic fields, are grouped into one term.

We can write this as an acceleration $\vec{g}$ for a fluid with density ρ as *external forces* $= \rho\vec{g}$ for a given volume of fluid.

Combining all of these components into equation 1.1, the general form of Newton's second law becomes the first equation of the Navier-Stokes equations, here written for a unit volume of liquid

$$\underbrace{\frac{\rho\partial\vec{u}}{\partial t}}_{\text{variational}} + \underbrace{\rho\left(\vec{u}\cdot\nabla\right)\vec{u}}_{\text{convection}} - \underbrace{\eta\nabla^2\vec{u}}_{\text{viscous dissipation}} = \underbrace{\nabla P}_{\text{internal forces}} + \underbrace{\rho\vec{g}}_{\text{external forces}} . \tag{1.2}$$

This is statement is written for incompressible fluids like the fluids considered in this thesis, If we were to consider compressible fluids, several more terms would be needed to account for the changing density. This is a field particularly relevant to engineers, aerodynamicists and astrophysicists [28, 29]. One of the common techniques used to solve compressible fluid dynamics problems is to use computational fluid dynamics [30].

Along with the conservation of momentum, we can also assume that conservation of mass holds true. The conservation of mass states that for any mass entering any given volume requires that either an equal mass must exit or a change of density ρ must occur. This relationship is described mathematically as

$$\frac{\partial\rho}{\partial t} + \nabla\cdot(\rho\vec{u}) = 0, \tag{1.3}$$

which says that any change of density over time, requires that the divergence of the momentum must also change [31]. For an incompressible fluid, the density stays constant with time, and equation 1.3 reduces to

$$\nabla\cdot\vec{u} = 0, \tag{1.4}$$

indicating that any amount of material flowing into a section of space requires the same amount must be flowing out. Figure 1.1 shows some examples of possible divergence patterns in two-dimensions that are valid for an incompressible fluid that has a divergence of zero. Equation 1.4 is the second of the Navier-Stokes equations. Now that we have discussed the Navier-Stokes equations in their most

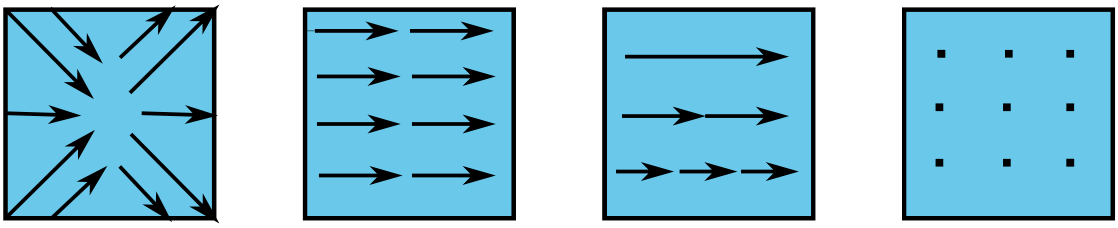

Figure 1.1: Examples of flow patterns with zero divergence, arrows indicate flow velocity.

general form, the following sections will look toward ways to simplify them to match the requirements of the systems in this thesis.

1.2.2 Simplifying the Navier-Stokes equations

In this section, we will walk through some simplifications that are relevant to the projects in this thesis, namely that we assume slow flows. Assuming slow flows means that the fluid is in a regime where the convection component of the flow is small. Because convection depends on the velocity squared (eq. 1.2) it highly complicates the already difficult equation, and by assuming it is small relative to the other terms in the Navier-Stokes equation allows for it to be neglected.

Another simplification that can be done primarily in terms of notation is to convert a body force into a pressure. For instance, a gravitational force often can be written as a hydrostatic pressure and therefore can be grouped into the pressure driven term. By dealing with slow velocities to disregard inertial components and converting the body forces to pressures, we can simplify the Navier-Stokes equations into

$$\frac{\rho \partial \vec{u}}{\partial t} - \eta \nabla^2 \vec{u} = \nabla P, \tag{1.5}$$

where the variational acceleration is driven by pressure gradients across the fluid but is slowed by viscous dissipation.

One useful example of this is to consider microfluidic chambers. Microfluidic chambers are small versatile devices that flow small amounts of liquid through a confined chamber using pressure gradients across the device. The flow is relatively

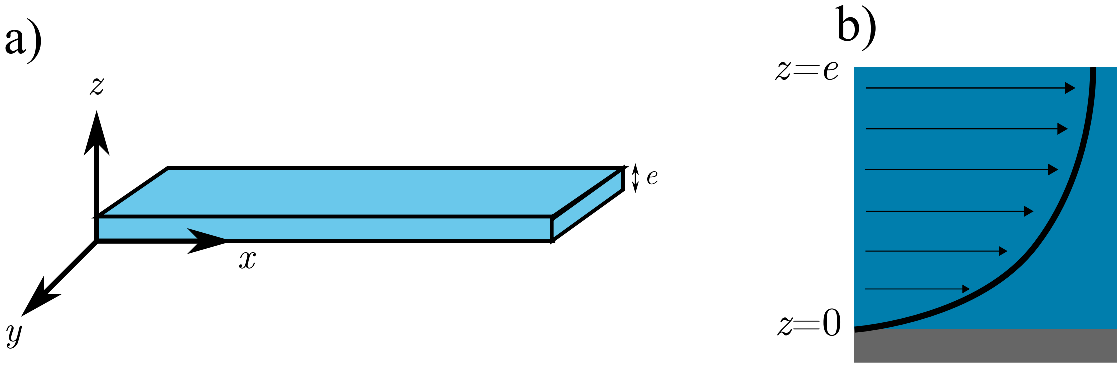

FIGURE 1.2: a) A thin liquid film that extends in the $x - y$ plane and is confined in the z-direction. b) A sample parabolic flow profile for a thin film of thickness e on a solid substrate.

slow and so any acceleration of the fluid is driven by the pressure gradients. Here, the viscous dissipation will slow motion of the items in the device [32, 33].

1.2.3 Thin film hydrodynamics

Even considering slow flows, equation 1.5 is still quite complicated as it is a three-dimensional set of equations. Relevant to this thesis in Chapters 3-5, we will now consider the lubrication approximation. The lubrication approximation makes a couple of assumptions based on the geometry of the fluid system. We first assume that the flow is steady, so there is no acceleration in the film and $\partial \vec{u}/\partial t = 0$. For a thin film where one direction is much smaller than the other two, it is reasonable to assume that the fluid will flow in in the lateral direction more than the direction corresponding to the small height, which reduces the three-dimensional vector problem into a two-dimensional. Following the schematic in figure 1.2a), if the film thickness is small in the z-direction, we can assume that the majority of flow will happen in the $x - y$ plane, with a small, but non-zero flow in the vertical direction.

The second assumption is that the film can sustain a flow. For the thin films present in this thesis (Chapters 3-5) there is a no-slip boundary where the film comes in contact with the solid substrate and a no-shear boundary condition at the free interface. These two boundary conditions require that at the solid-liquid interface the velocity of the film is zero relative to the boundary, *i.e.* $u = 0$ at $z = 0$

and at the liquid-air interface when the film thickness is $z = e$, there is no shear force and $\partial u/\partial z = 0$ at $z = e$. For flow with these boundary conditions, there must be a velocity gradient over the thickness of the film, $\partial u/\partial z \neq 0$ for general z, and that there is a viscous force opposing the flow in the diffusion term. The flow is pressure driven and moves liquid from areas of high to low pressure in one direction. Here we assume that the pressure gradients are constant or independent of the z-direction. The viscous dissipation opposes flow due to gradients in velocity in the z-direction, we can now write down the lubrication approximation,

$$-\frac{\partial P}{\partial x} + \eta\frac{\partial^2 u}{\partial z^2} = 0. \tag{1.6}$$

Finally, it is possible to integrate this equation analytically with the boundary conditions. The double integration required from the velocity gradients in the vertical direction indicates that the flow will be parabolic in z. Integrating once with respect to z gives

$$-z\frac{\partial P}{\partial x} + \eta\frac{\partial u}{\partial z} + C = 0, \tag{1.7}$$

where C is an integration constant that will be solved in a later step. Integrating again, we find

$$-\frac{z^2}{2}\frac{\partial P}{\partial x} + \eta u + Cz + D = 0, \tag{1.8}$$

with D being another integration constant. Using the no-slip boundary condition, when $u = 0$ at $z = 0$, we see that $D = 0$. At the top of the film, when $z = e$, we know that $\partial u/\partial z = 0$ to ensure a no-stress boundary condition. Implementing the boundary condition, we find that $C = -e\frac{\partial P}{\partial x}$. For a thin film that has a no-slip boundary and a free interface, the resulting equation is

$$-(\frac{z^2}{2} + ze)\frac{\partial P}{\partial x} + \eta u = 0. \tag{1.9}$$

Solving for the velocity of the film, we find that the velocity is parabolic in z. Figure 1.2b) shows a sample parabolic flow profile for this film, and is often referred to as Poisueille flow or pipe flow [25].

Other boundary conditions can cause other flow patterns. For example, two no-shear interfaces on either side of the film will result in a uniform flow across the film. This is known as plug flow and is often present in the drainage of soap films [34]. Another example consists of two no-slip boundary conditions, with one boundary moving relative to the other. These conditions create a linear flow profile known as Couette flow [25].

Furthermore, equation 1.6 can be understood from scaling arguments, the average velocity U of the fluid flow should depend on the thickness of the film and the pressure gradients, as well as a characteristic horizontal length scale L [34],

$$U \propto \frac{e^2}{\eta}\frac{\Delta P}{L}, \tag{1.10}$$

where L is a value that depends on the geometry of the problem. In addition, we can define the flow rate Q as the flow through a section of film due to this pressure in the x-direction

$$Q = eU \propto \frac{e^3}{\eta}\frac{\partial P}{\partial x}. \tag{1.11}$$

The relationship between flow rate and film thickness can therefore be directly related to the pressure gradient that drives the flow of the fluid [35].

1.2.4 Viscous dissipation

Common descriptions of fluids often hold clues to their viscosity: gooey honey, thick cream, runny milk. In everyday life we use relative terms to describe the viscosity of a liquid by comparing it to known liquids, like ‘more runny than whipping cream, but thicker than whole milk’. Viscosity is something that many people have an intuition for without a scientific definition. The definition of viscosity is formed through an understanding how of a liquid will flow in response to a shear stress. For instance, a volume of liquid that touches two flat plates on opposite sides of the liquid, with a contact area A, is sheared when the top plate is moved with a constant velocity u with respect to the bottom plate. The shearing is shown schematically in figure 1.3. The shearing motion will be resisted by a force F that is due to the viscosity of the fluid. Assuming that there is a constant deformation $\Delta x\left(t\right)$ in response to the shear after some time, we can define a constant shear

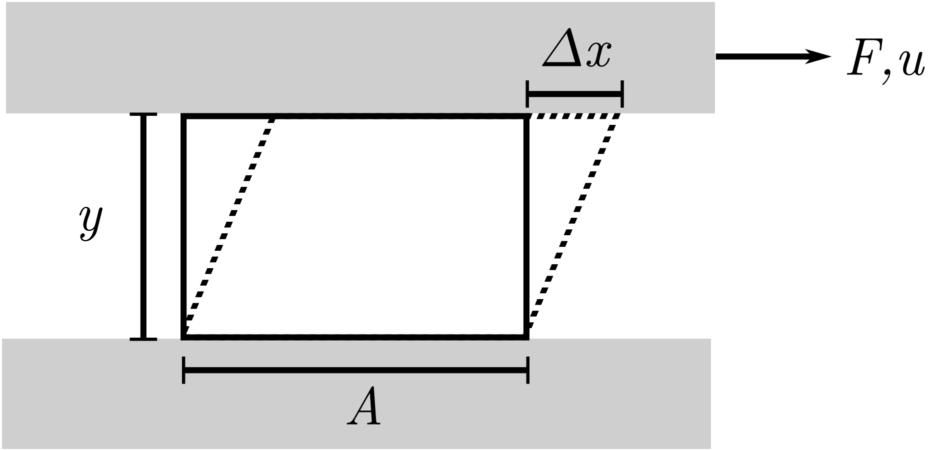

FIGURE 1.3: A schematic of a volume of fluid in contact with two plates touching with area A. The top plate is moved a distance Δx at a constant velocity u with a force F. The separation between the plates is a distance y.

strain $\epsilon = \Delta x\left(t\right)/y$. For a Newtonian liquid, which has constant viscosity regardless of the shear strain rate $\dot{\epsilon} = u/y$, we expect that the viscosity will appear as a proportionality constant between the shear strain rate and the force for a given area,

$$\frac{F}{A} = \eta\frac{u}{y} = \eta\dot{\epsilon}. \tag{1.12}$$

Non-Newtonian fluids exhibit non-constant viscosity depending on the applied shear strain rate. For example, toothpaste is shear thinning and the viscosity will decrease as a shear strain rate is increased. The opposite example is that of completely soaked sand, which shear thickens when a fast shear strain is applied and is the reason why wet sand will appear more solid when stepped on quickly but flows like a fluid when slowly perturbed [36, 37].

At the molecular level, viscosity comes from an energy cost to rearranging the structure of the network of molecules. For the purposes of this thesis, we can approximate viscosity as something similar to friction between molecules. This ‘friction’ dissipates energy through the fluid, just like friction between two surfaces dissipates kinetic energy, for instance when friction from rubbing your hands together dissipates energy in the form of heat. We can consider the case of a thin film again, where at the solid-liquid interface there is a no-slip boundary condition. A no-slip boundary condition means that the velocity of the fluid at the bottom of the film must be equal to zero and at the top of the film the velocity will be u. In order to transition between these two velocities, there must be a velocity gradient inside of the film, which can be discretized, so the flow happens in layers. Each layer will have a slightly different velocity (similar to the arrows shown in fig 1.2b)), and will impart a shear force on each subsequent layer. The energy lost to this is called viscous dissipation and is an important concept in highly viscous flow. Generally, viscous dissipation takes the scaling of $\eta\nabla^2\vec{u}$.

1.2.5 Drag

Drag is closely linked to viscous dissipation, which is the resistance felt by an object moving through a fluid. You might feel drag on a particularly windy day when you walk on the sidewalk and feel the air resisting you, or as you dangle your hand through water while on a moving boat. Drag depends on the speed of the object u, the cross sectional area A, a drag coefficient C_d and the density of the fluid ρ [25]. For an object moving through a fluid with a constant speed that is propelled by a constant force F, there must be an equal and opposite force resisting any acceleration, and this is the drag force. Generally, the drag force is $F_d = \frac{1}{2}\rho u^2 C_d A$ [25]. For highly viscous flows (*i.e.* low Reynolds number as discussed in section 1.4.1), like those handled in this thesis, C_d asymptotically approaches $1/\text{Re}$, where the Reynolds number, $\text{Re} = \rho u L/\mu$, and μ is the viscosity and L is a characteristic length scale of the system [38, 39, 40]. The Reynolds number compares viscous forces to inertial ones. For slow flows, the drag force is

$$F_d = \frac{1}{2}\frac{\mu u A}{L}. \tag{1.13}$$

For the case of a sphere, the length scale is the radius $L = R$, and area is the cross section of the sphere $A \propto R^2$. Inserting the length and area into the general expression for drag force (equation 1.13) gives the drag force $F_d = c\mu u R$, where all of the numerical coefficients are combined into a general coefficient c. From this expression, the faster the flow around the sphere, the larger the drag force will, and larger spheres will experience a larger drag force. For a sphere, the drag coefficient c can be solved analytically to be 6π [31]. Relevant to this thesis, the drag force on a bubble rising through a fluid bath sets the terminal velocity on the bubble due to the balance between buoyancy and drag. The buoyant force is dependent on the volume of the bubble and the density difference between the bubble and the bath

$$F_b = \frac{4}{3}\pi R^3 \Delta\rho g. \tag{1.14}$$

By balancing buoyancy and drag, then solving for the velocity, we can find the terminal velocity, v_t, for the bubble when it rises through the fluid,

$$v_t = \frac{2R^2\Delta\rho g}{9\mu}. \tag{1.15}$$

Drag on a spherical particle comes into particular relevance in measuring the viscosity of the fluid baths used in Chapter 6 along with the motion of the buckled bubble chain as it moves through the bath.

1.3 Capillarity

The research presented in this thesis is focused on interactions that happen at liquid interfaces. When a system has a large interface to bulk ratio, surface properties become important. Surface properties typically dominate in small volumes, when the small length scales of the system require that the volumetric scaling is much smaller than the surface area scaling. The study of fluid interfaces is often referred to as capillarity, which is the reason why bubbles are round and why the water at the edge of the glass is curved. Capillarity and capillary interactions have been an area of active study in the past number of years, and capillarity has been the driving force in thin film hydrodynamics studies [41, 42, 43], interactions with elastic media [44, 45, 46] and capillary induced instabilities [47, 48, 49]. In this section, I will provide the background information behind capillarity and how it pertains to drops and bubbles.

1.3.1 Surface tension

When you pour a glass of water, the bulk of the liquid travels toward the bottom of the glass due to gravity. Examining the surface closely, we see that at the surface it is perfectly flat at the center of the glass and curves slightly at the edges of the glass (the edges will be discussed in section 1.3.3). Swirl the glass or lift it to take a drink and the water flows, distorting that perfectly flat surface, but upon setting it back down the water quickly reforms the planar configuration. The reason for this beautifully flat liquid surface is of a property called surface tension. Consider surface tension as a restoring force that holds a liquid surface as taut as the geometry will allow. An excellent visualization of this is to take a soap film (like children may do in the summer months) and gently blow on the film as though to blow a bubble, not enough to detach the film as a bubble but just enough to distort the film. Stopping, you will notice the film springs back to a flat configuration as though it were stretched like an elastic sheet.

The origins of surface tension come from interactions at the molecular level. A liquid consists of molecules held together with inter-molecular bonds. These bonds are typically strong enough to keep the molecules in a condensed state, but not so strong that they are frozen strictly in place like a solid. Water is cohered with strong hydrogen bonds, whereas something like an oil is held together more loosely with weaker van der Waals forces. In the bulk of the liquid, each molecule feels an isotropic attraction and repulsion, and there is a minimal energetic cost of interaction because like-like interactions are generally the most favourable and has the lowest energy cost [1, 34].

At the surface of the liquid, a molecule will only have favourable interactions where it is in contact with the rest of the bulk. Figure 1.4a) shows a schematic of interactions of two sample liquid molecules, one in the bulk and one at the surface. The anisotropy of the configuration around the molecule at the surface means that part of it is forced to interact with a less favourable medium like a gas, other immiscible liquid, or solid, and this costs the system more energy than interacting in the bulk liquid. Nature is always seeking to minimize free energy and will work to reduce an excess surface and surface tension is the physical realization of this phenomenon. Surface tension can be treated as an *energy cost per unit area*

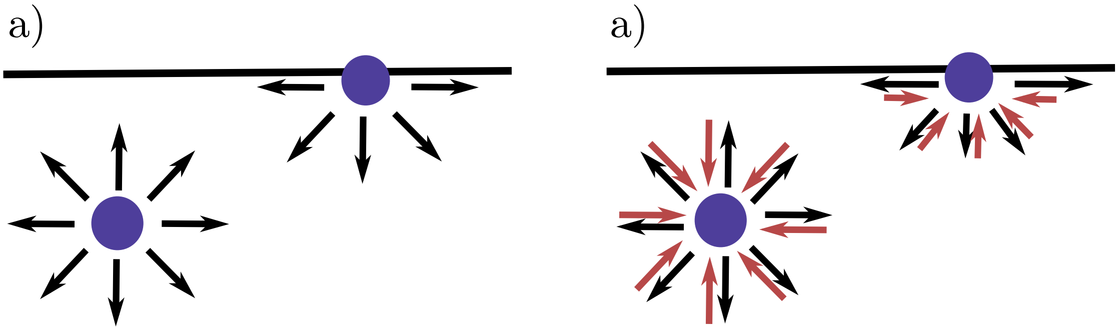

FIGURE 1.4: a) Two liquid molecules, one in the bulk showing isotropic interactions with the nearest neighbours and one at the surface with anisotropic interactions. b) The same sample schematic as in a) but now showing the relative strength of both attractive and repulsive interactions.

and is frequently denoted as γ. Considering surface tension as an energy cost per area makes sense from a mechanical point of view because to create more interface means to create more locations for unfavourable interactions and thus, costs more energy. The relationship between energy, area and surface tension can be written as

$$\delta W = \gamma \, dA, \tag{1.16}$$

where δW is the work done on the system, and dA is the change in area. In the earlier example of blowing on the soap film, you are providing the work through your breath, and the amount you must blow on the film to distort it by a given area change is dependent on the surface tension.

Surface tension also has equivalent units as a *force per unit length* that runs parallel to the surface of the interface. One of the confusing things for me during my thesis work was understanding why, based on the energy interaction diagram in fig 1.4a), the force is not normal to the surface. Considering figure 1.4 it appears as though the unbalanced interactions should be pulling down into the liquid. This figure, although common in many textbooks, is deceptive as it only shows the attractive interactions. Molecules in a liquid will experience a long range attraction, like van der Waals or hydrogen bonds, along with a repulsive interaction at short range to prevent molecules from overlapping with one another [1]. Combining the long range attraction and short range repulsion gives the interaction energy as a function of separation distance which can be approximated as the Lennard-Jones potential and is plotted in figure 1.5. The Lennard-Jones potential is a simplified model of atomic interactions that depends on the strength of the potential well ϵ and a particle size σ. A minimum in the potential indicates the distance between molecules for which the system is optimized, r_{min}. Moving two molecules closer than r_{min} repels the molecules and moving them farther apart will cause them to attract. One consequence of having short range repulsion and long-range attraction is that when there is anisotropy at a given location, there can be an anisotropy in the resulting interaction strengths. Early works in understanding molecular interactions and molecular dynamic interactions show that at a surface of a liquid the combination of the anisotropy at the interface and a decrease in molecule density results in a larger attractive force parallel to the interface [50, 51]. Figure 1.4b) shows the anisotropic attractive and the isotropic repulsive interactions at the surface compared to in the bulk. Thus, the force extends parallel to the interface. The anisotropy in molecular interactions is what gives rise to the macroscopic energy cost of creating more interface, known as surface tension.

1.3.2 Contact angles

Consider a droplet of water on a glass window, from observation one can see that the droplet does not lie flat on the window but beads up on the surface. Zooming in to the contact line where the solid, liquid, and gas meet, there is a constant angle all the way around the base of the droplet. This angle is known as the contact angle θ_E and comes from a balance of the three interfacial tensions, the solid-liquid γ_{SL}, solid-vapour γ_{SV} and liquid-vapour γ. All three of these forces per unit length are pulling away from the contact point and this is shown schematically in Figure 1.6 a). It is worth noting here that the angle depends on the material properties of the solid substrate, liquid drop and surrounding gas or liquid.

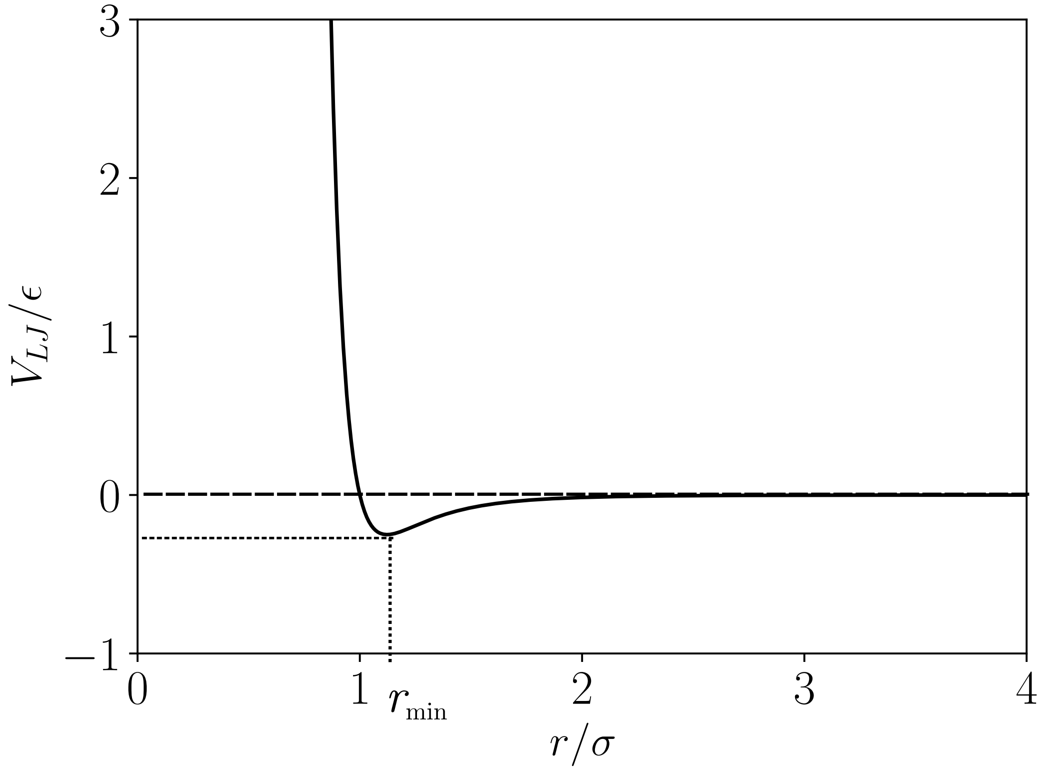

FIGURE 1.5: A plot of the Lennard-Jones potential showing the normalize interaction energy as a function of the normalized separation distance. The separation distance r_{min} marked by the minima indicates the equilibrium state for two atoms in a balance between short range repulsion and long range attraction.

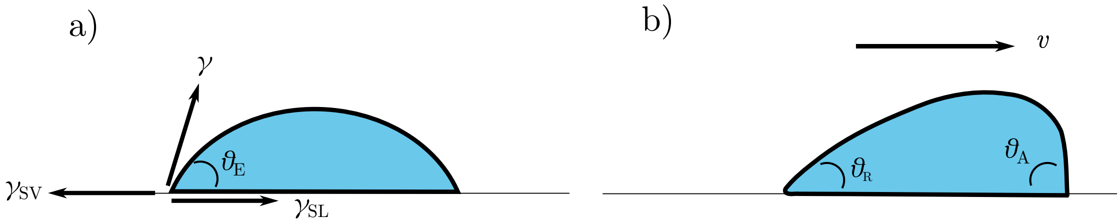

FIGURE 1.6: a) A static drop on a solid surface in equilibrium. The three surface energies acting on the contact line with magnitudes dependent on the respective interfacial tensions: γ_{SV} at the solid-vapour interface, γ_{SL} at the solid-liquid interface, and γ at the liquid-vapour interface. A horizontal force balance between these three forces gives the contact angle θ_E. b) A drop moving with a velocity v. The leading edge has an advancing contact angle θ_A and the trailing edge has a receding contact angle of θ_R.

Considering that a horizontal force balance at the contact line must be true for a static droplet, we find Young's relation where

$$\gamma \cos(\theta_E) = \gamma_{SV} - \gamma_{SL}. \tag{1.17}$$

Changing the contact angle will change the shape that the liquid sits on the solid surface. For a given volume of drop, as the contact angle decreases, the liquid spreads out, and conversely as the contact angle increases, the liquid beads up higher on the surface.

In order to spontaneously move drops on a surface, the contact angle will need to change from the static contact angle. Moving the drop towards a new, dry area of the surface will require that the contact angle exceed an advancing contact angle θ_A, *i.e.* $\theta > \theta_A$. If a contact angle is less than this critical angle, the shape of the drop will change, however the contact line will only move when the advancing contact angle is exceeded. Similarly, there is a receding contact angle, θ_R, which is a minimum angle that can be sustained before the trailing edge will retract and expose more solid substrate. The advancing and receding angle requirements can be seen when drop rolling down a window will have a bulbous front and a drawn-out tail, an example of this is shown in figure 1.6b). Motion on a pre-wet surface, such as the motion of the drop on a conical fiber like presented in Chapters 3-5, will require less force to move due to the decreased requirements to change the apparent contact angle of the drop due to the film. In particular, the importance of a lubricating film and the effects on the droplets motion are discussed in Chapter 3.

Another interesting effect of the contact line is that often a vertical force balance is disregarded because as the liquid-vapour surface tension pulls upwards on the solid, the stiffness of the solid balances the small upwards force without deforming. Soft solids, like gels, rubbers, and thin flexible films deform to balance this force by creating a small wetting ridge around the drop [52]. This ridge changes the dynamics of drop motion; in order to move the drop, it must not only distort to exceed the advancing and receding angle limits but also must overcome the increased dissipation caused by the wetting ridge [46]. Wetting ridge dynamics is an important topic in tribology and understanding how liquids and soft solids interact is important in the field of bio-engineering, the food industry and the rubber industry [53].

1.3.3 Wetting

Closely linked to contact angles is the concept of wetting. Wetting described how much a liquid will spread on a solid surface; for example, a drop of water placed on a table will stay beaded up, where a drop of silicone oil will spread out until it completely coats the table. Wetting also determines the meniscus that forms between a liquid and a container. The meniscus forms due to a balance between gravitational and capillary forces and the wetting causes a rise or depression of the liquid at the contact line.

To understand wetting one can ask if would it be more favourable to have a given surface be wet or dry? A spreading parameter S indicates the energetic difference between a wet and a dry surface [34]:

$$S = \gamma_{SV} - (\gamma + \gamma_{SL}), \tag{1.18}$$

where the energy of the dry surface (γ_{SV}) is compared to the wet surface (including the energy of both the solid-liquid interface and the liquid-air $\gamma + \gamma_{SL}$). The spreading parameter identifies two regimes, when $S > 0$ and when $S < 0$.

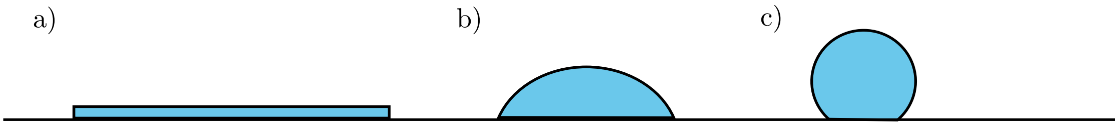

FIGURE 1.7: A schematic of a) totally wetting, b) mostly wetting, and c) mostly non-wetting liquids on a surface. The totally wetting liquid spreads until it creates a microscopically thin film, the two partially wetting droplets form spherical caps on the surface.

When $S > 0$, the liquid is totally wetting the surface, and it is energetically favourable for the liquid to be in contact with the solid. As a result, the liquid will spread out until it forms a coating over the entire surface. The liquid and solid combination used in this thesis, silicone oil and glass, is one example of a totally wetting liquid-solid combination. Figure 1.7a) shows how a totally wetting droplet placed on a surface will spread out to form a microscopically thin film [34].

When $S < 0$, it is more costly to have the liquid be in contact with the solid and therefore the liquid only partially wets the substrate. The liquid beads up on the surface and a small drop forms a spherical cap. The liquid forms a contact angle according to Young's relation (equation 1.17), and if the contact angle is acute, $0 < \theta_E < \pi/2$, then the liquid is said to mostly wet the surface (fig. 1.7), and the energetics are mildly favourable for the two to be in contact. For obtuse contact angles $\theta_E \geq \pi/2$, the liquid mostly non-wets the surface, and forms marble-like drops that are easy to roll off. Examples of totally wetting, mostly wetting and mostly non-wetting drops are shown in figure 1.7 a)-c), respectively. Tuning the wettability of a surface has many key applications in both industry and everyday life including coatings on non-stick frying pans, hydrophobic coatings on tents and rain jackets, and cell adhesion, among many others [44, 54]

1.3.4 Laplace pressure

When introducing surface tension in section 1.3.1, I described that surface tension acts parallel to the surface of the liquid. In this section, we will discuss how surface tension manifests itself over a liquid volume and how it creates a pressure at curved surfaces. Furthermore, I will postulate that flow due to topography is due to pressure gradients. Pressure at a curved interface is called Laplace pressure

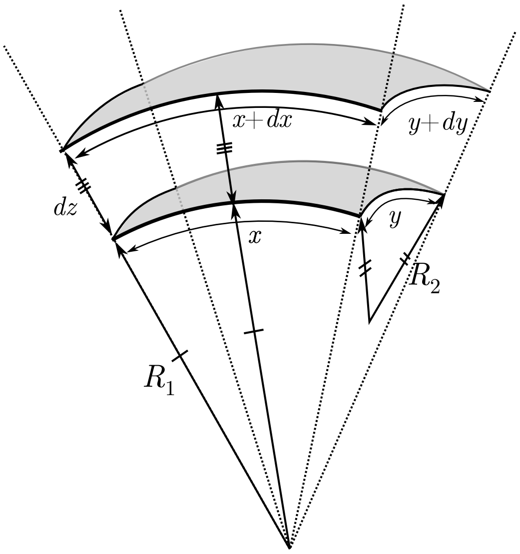

FIGURE 1.8: Diagram used for deriving Laplace pressure on a general curved surface with two orthogonal radii of curvature, R_1 and R_2. The surface is then inflated by a radial distance, dz and the surface increases in size (adapted from Adamson [55].

and is readily seen when it stabilizes bubbles and drops from deformation. Laplace pressure is caused by surface tension, and to understand where it originates we can look at a general curved surface, as shown schematically in figure 1.8 [55].

The general curved surface can be described by two orthogonal radii of curvature, R_1 and R_2. The surface is chosen so that the two radii are constant over the expanse of the surface, which has an area A_1. The area is defined so that $A_1 = xy$. If the surface is inflated by an infinitesimal radial distance of dz, we can define the new area $A_2 = (x + dx)(y + dy)$. The difference in surface area ΔA between the inflated and original surface is

$$\Delta A = A_2 - A_1 = xdy + ydx. \tag{1.19}$$

If we postulate that producing new surface area requires work W, which depends energy cost per unit area γ, the work required to inflate the surface is

$$W = \gamma \Delta A = \gamma(xdy + ydx). \tag{1.20}$$

We can use the relation between the arc length of a circular sector to the radius to compare the arc length and radii of the original and inflated surfaces. For the plane associated with R_1, we find

$$\frac{x}{R_1} = \frac{x + dx}{R_1 + dz}. \tag{1.21}$$

When the ratio is rearranged for dx, this relation becomes

$$dx = \frac{xdz}{R_1}. \tag{1.22}$$

Similarly, the other plane finds that $dy = ydz/R_2$. Inserting the$x$ and y differentials of these into equation 1.20 gives,

$$W = \gamma \left(\frac{xydz}{R_1} + \frac{xydz}{R_2} \right). \tag{1.23}$$

The above expression for work states that the energy to increase the surface area will depend on the radii of curvature, the area A_1 and distance expanded dz. Now we can consider that from thermodynamics, work is also related to a pressure difference acting on an area A_1 through the distance dz,

$$W = \Delta P A_1 dz = \Delta P xydz. \tag{1.24}$$

Setting the two values for work (equations 1.23 and 1.24) equal, we arrive at the expression for Laplace pressure

$$\Delta P = \gamma \left(\frac{1}{R_1} + \frac{1}{R_2} \right). \tag{1.25}$$

The Laplace pressure states that any surface that is concave will have a negative pressure, and a convex surface will have positive pressure. The canonical example often used to explain this phenomenon is a sphere which has a higher pressure inside compared to the medium outside, with $\Delta P = 2\gamma/R$. Small droplets have higher Laplace pressure than large drops and this explains why small bubbles are more stable to deformation than large bubbles.

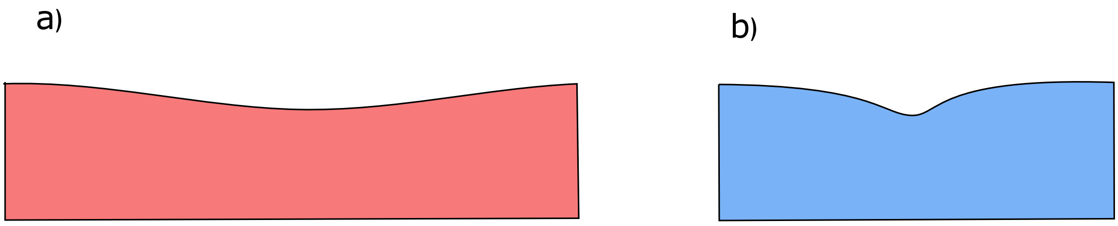

Figure 1.9: a) A shallow indentation in a volume of liquid with low Laplace pressure gradients. b) A sharp indentation into a volume of liquid with high Laplace pressure gradients

The Laplace pressure also has consequences for fluid flow. Imagine if a flat liquid surface was perturbed slightly so that there is a non-flat topography on the surface. The topography of the surface is no longer flat, surface tension will act to reduce any excess area. As discussed in section 1.2, the way that a liquid flows is determined by pressure gradients. Consider a curved surface perturbed in two different ways, but with the same excess area, one has a long shallow increase, where the other is narrow and deep (samples are shown in figure 1.9), we can ask ourselves which will fill in more quickly, and why? Intuition tells us the narrow and deep perturbation (figure 1.9b)) will resolve itself more quickly. We now know that the highly curved surface has a much higher local Laplace pressure. The surface with the deeper indentation therefore has larger Laplace pressure gradients between the indented surface and the flat interface further away than the shallowly deformed surface. The larger gradient in Laplace pressure results in a larger flow, as discussed in section 1.2.2.

1.3.5 Capillary length

Capillary forces generally are weak in comparison to other forces that we experience in our every day. However, on small scales capillary forces are incredibly important and can add up to macroscopic effect. For example, ground water is transported through capillary action in soil [56, 57], solvents in rapid tests for COVID-19 are drawn through the paper due to capillary forces [58, 59], and capillary action causes transpiration in plants [60, 61]. The length scale that compares the relative scales of gravity and capillarity is known as the capillary length. A scaling argument begins with the hydrostatic pressure P_{hyd} of a liquid with density ρ in Earth's gravity g at a depth of l_c

$$P_{\text{hyd}} = \rho g l_c. \tag{1.26}$$

The hydrostatic pressure would be balanced by the Laplace pressure in the liquid with surface tension γ and average radius of curvature l_c,

$$P_{\text{cap}} = \frac{\gamma}{l_c}. \tag{1.27}$$

Setting these two pressures equal and solving for l_c gives the following expression:

$$l_c = \sqrt{\frac{\gamma}{\rho g}}. \tag{1.28}$$

For many liquids on Earth, the capillary length l_c is around a few millimeters in length [34] and any system with a characteristic length scale $r < l_c$ will be dominated by capillary forces. Menisci on the sides of the drinking glass are on the order of a few millimeters in length because this is the length scale where capillary forces and gravity are balanced. The capillary length also explains why anything smaller than this scale appears to be unaffected by gravity.

If the length scale L of the system is larger than the capillary length, gravity dominates, and surface tension can be neglected in favour of bulk forces. The majority of this thesis operates in the regime where capillary forces dominate.

1.4 Comparing forces

For many hydrodynamic problems in soft matter, it is useful to note which forces are relevant over the scales of the system. A simple way to do this is to compare the magnitude of two forces in a system is by dividing them. Depending on the resulting ratio, a large or small number would indicate a dominant force, where a ratio ~ 1 would indicate both forces are important. Many physics problems can be simplified by considering the dominant forces and making the appropriate approximations. Reducing a problem based on the relevant dominant regimes has already been done in the section on fluid dynamics (section 1.2). For example, when simplifying the Navier-Stokes equations, the inertia was small compared to the viscous forces, and only the viscous term was considered. In this section, we will examine ratios of two forces that show up regularly in this thesis. The ratio of two forces will be dimensionless, and these ratios are often referred to as dimensionless numbers.

1.4.1 Reynolds number

The Reynolds number, Re, is the comparison of inertial forces to viscous forces. The Reynolds number commonly appears in fluid dynamics to quickly determine if the flow will be turbulent or laminar or somewhere in-between. From the Navier-Stokes equations, we can directly take the inertial and viscous terms and divide them to find the Reynolds number

$$\mathrm{Re} = \frac{\text{inertial term}}{\text{viscous term}} = \frac{(\vec{u}\cdot\nabla)\vec{u}}{\eta\nabla^2\vec{u}}. \tag{1.29}$$

The relationship between inertia and viscosity is the same in one dimension as it will be in three, and reducing to a one-dimensional problem simplifies the above equation and the Reynolds number becomes

$$\mathrm{Re} = \frac{\rho U L}{\eta}, \tag{1.30}$$

with the density ρ, characteristic flow speed U, typical length scale L and viscosity η. One can imagine for a highly viscous fluid, Re becomes small, and conversely large for an inviscid fluid. The length scale, fluid speed and density also vary Re proportionally. For a highly viscous liquid that is moving slowly at a small length scale, the flow will be laminar and the $\mathrm{Re} < 1$. When $\mathrm{Re} < 1$, viscosity dominates. For larger length scales with faster flow, inertia begins to dominate and the potential for turbulence increases and $\mathrm{Re} > 1$. This thesis focuses on systems with small Re, and we assume flow is laminar with viscous forces dominating the flow properties.

1.4.2 Bond number

Another important comparison of forces in this thesis is the comparison of capillary forces to gravitational forces. Comparing capillarity and gravity is applicable when examining the shape of drops and bubbles, where the ratio of the body force of gravity (volume dependent) to the capillary force (surface area dependent) determines the stability of the drop. To a scaling order, the hydrostatic force is $\rho g L^3$, where L is the length scale of the drop whereas the force due to surface tension is γL. The ratio of these two forces is called the Bond number Bo,

$$\mathrm{Bo} = \frac{\rho g L^3}{\gamma L} = \frac{\rho g L^2}{\gamma}. \tag{1.31}$$

When $\mathrm{Bo} > 1$, gravity exceeds surface tension and gravity must be considered when handling the problem. In the context of drops and bubbles, where the length scale L is commonly defined as the radius of the drop or bubble R. A large Bo means that there will be a difference in hydrostatic pressure across the drop, and the drop may deform due to gravity. For example, when a drop becomes large, like dew drops hanging from a strand of spider silk, the drops sag below the fiber and are no longer axisymmetric. When the bond number is small, $\mathrm{Bo} < 1$, surface tension dominates, and the droplet will be smaller than the capillary length; gravity is negligible. A droplet will surround the silk strand or fiber axisymmetrically. Droplets and bubbles with small Bo are considered in this thesis and therefore the shape of the droplets is determined entirely by surface tension. Typically, drops with small Bond numbers are referred to as droplets.

1.4.3 Capillary number

The final relevant comparison between forces is the competition between viscosity and capillarity. Known as the capillary number, the viscous forces are divided by the capillary forces. The general scaling for a viscous force is $\eta U L$, and capillary forces scale as γL, and dividing these gives the capillary number Ca,

$$\mathrm{Ca} = \frac{\eta U L}{\gamma L} = \frac{\eta U}{\gamma}. \tag{1.32}$$

The capillary number is often used to understand different regimes when depositing Landau-Levich-Derjaguin films (see section 1.6.1 for a detailed derivation) [62, 63, 64]. Landau-Levich-Derjaguin (LLD) films are liquid films that coat a solid as the solid is drawn out of a liquid bath. As a solid is pulled out of a bath, the viscosity of the liquid causes a film to be entrained along with the solid, whereas surface tension opposes creating new interface. Ca directly compares surface tension to viscosity. A large capillary number indicates a viscosity dominant regime with a thicker film, whereas a small capillary number indicates that surface tension dominates and will create a thinner film or no film at all.

1.5 Equilibrium shapes of drops

In this section, I will discuss the equilibrium shapes of drops in different geometries. Combining the material in section 1.2 and section 1.3, I will derive the shapes of drops in liquid baths, on solid surfaces and on cylindrical fibers. Of particular importance to this thesis are the shapes of drops on fibers and in liquid baths. Understanding drop shapes at equilibrium enables several measurement techniques including measuring surface tension using the pendant drop method [65, 66], contact angles of sessile drops [67, 68] and wetting properties [69]. Drops in a bath are used in a multitude of applications, including changing material properties during manufacturing, like creating a metal foam during casting [70, 71], and to improve nutrient transport in biological systems for mollusc farming [72]. Systems with drops on fibers have been used to develop lab on chip-like networks [73], drops have been used to bend and deform slender fibers [19, 21] and to look at transport properties of surfaces [9].

1.5.1 In liquids

As described in section 1.3, surface tension drives the minimization of surface area of an interface. For two immiscible liquids, with one dispersed phase inside of a continuous phase, the dispersed phase will form domains in the continuous phase and the geometry is set by the surface tension. Surface tension will minimize the interface to form a sphere [74]. A free volume of liquid with $\mathrm{Bo} < 1$ will form a spherical droplet. The radius of the droplet depends on the volume of liquid for incompressible fluids, but depends on the hydrostatic pressure for a compressible one [75]. One can see this effect when enjoying a carbonated beverage, like beer or sparkling wine. Carbon dioxide bubbles that form at the bottom of a glass inflate as they rise through the glass. At the bottom of the glass there is a higher hydrostatic pressure pushing inwards compared to further up the liquid column. Although the bubbles are still spherical because the pressure across the bubble is constant, there is a slight inflation due to the global change in pressure as the bubbles rise.

For example, a typical nucleated bubble is $\sim$ 100 μm in radius [76] and the typical pint glass is $\sim$ 20 cm in height. The difference in hydrostatic pressure at the top of the glass compared to the bottom is $\sim \rho g \Delta h \sim -200 Pa$. To keep the Laplace pressure $2\gamma/R$ inside the bubble the same, the radius must change. Using a surface tension of $\sim$ 72 mN/m, we find that the change in radius from the bottom to the top of the glass is $\sim$ 720 μm, which is a very large increase and in fact much larger than one would typically see in a glass of beer. This simple calculation does not account for gas dissolution into the liquid, which would decrease the volume of gas present, but does show that an increase in radius is expected for gas bubbles [75].

1.5.2 On surfaces

Consider a droplet on a solid surface, for instance if you spilled a small drop of coffee on the counter. The coffee will form a spherical cap because surface tension pulls the volume of liquid into a spherical section to minimize the free surface. For a partially wetting fluid, the shape is also constrained by the contact angle set by the three surface energies. Both large and small drops will be considered in this section, but first we must define the cut off between them. The distinction between a large drop and a small droplet is delimited by the capillary length l_c as defined in section 1.3.5. Looking down from above onto the surface of the drop, the radius R is based on the circle formed by the contact line. If $R < l_c$ like the example shown in figure 1.10a), capillary forces dominate and the shape of the droplet will depend on the two constraints: the contact angle and volume. In addition, the curvature of the free surface will be constant.

For drops with $R > l_c$, gravity begins to be important and if one has a disastrous coffee spill, you will note that the puddle begins to spread out with a constant

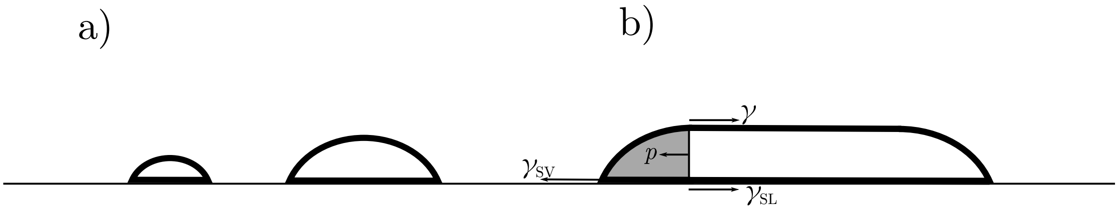

FIGURE 1.10: a) Small liquid drops that partially wet a surface and form a spherical cap. b) A large drop that spreads out like a puddle. The height of the puddle is determined by a balance of interfacial tensions and hydrostatic pressure.

thickness, e. To calculate the height of this puddle, we must consider both capillary forces and hydrostatic pressure.

Surface forces - Consider the diagram in figure 1.10b), ignoring the effect of the edge of the drop indicated by the shaded region and considering the shaded region as small body of fluid, at each of the surfaces there will be a force per unit length at the contact line. Summing these forces gives $\gamma_{SV} - (\gamma + \gamma_{SL})$, which is the spreading parameter, S.

Hydrostatic pressure - The hydrostatic pressure P will push the liquid from high regions to low regions. The pressure acting on a given location is calculated by integrating the pressure from the top of the puddle to the bottom

$$P = \int_0^e \rho g(e - z)dz = \frac{1}{2}\rho g e^2. \tag{1.33}$$

Summing up these forces per unit length, shows that $S = -1/2\rho g e^2$. To gain insight into how the thickness of the puddle changes with the contact angle, it is useful to substitute in Young's relation into the spreading parameter, where $S = \gamma(1 - \cos\theta_E)$. Rearranging finds that

$$e = \sqrt{2}l_c(1 - \cos\theta_E)^{1/2} = 2l_c\sin(\theta_E/2), \tag{1.34}$$

and we see that the thickness of the puddle increases for larger contact angles.

1.5.3 On fibers

Drops on fibers are something that we see quite frequently in nature, like rain drops on pine needles or dew on spider webs. Although it is trivial for one to imagine the shape of a droplet suspended on a thin wire, the mathematical form is more difficult to derive and can take on different shapes depending on the geometry and wetting conditions. A small, totally wetting droplet will surround the fiber forming a barrel shape. If the Bond number Bo is small, meaning that gravity can be ignored, and the droplet will be axisymmetric around the fiber. Increasing the drop size beyond a Bond number of 1 will result in a drop that is not axisymmetric around the fiber. If the fiber is held horizontal to gravity, the drop will sag underneath the fiber, and turning the fiber so it is held vertical with respect to gravity will result in the droplet sliding down the fiber [77]. If the drop is partially wetting, the contact line must also be considered, and for smaller drops on larger fibers we see a clam configuration, where the drop clings to one side of the fiber.

For the droplets considered in this thesis, we will assume the droplet totally wets the fiber and Bo is small, resulting in a barrel shaped, axisymmetric droplet. A drop of radius R is deposited on a fiber that has a constant radius of b as shown in figure 1.11. We also assume that $R >> b$ meaning that the Laplace pressure in the droplet is low. Here we will derive the shape of a totally wetting drop on a thin fiber, which is relevant to the work presented in Chapters 3-5. The liquid totally wets the fiber and has a contact angle of $\theta_E = 0$.

Some important notes before we begin the calculation are:

- The pressure everywhere in the droplet must be constant, otherwise there would be flow from high to low pressure and the droplet not be in equilibrium.
- If the pressure is constant everywhere throughout the droplet it is required that the curvature C of the surface of the droplet must also be constant according to Laplace pressure $\Delta P = \gamma C$

We first begin by examining the end of the droplet, where the droplet comes into contact with the fiber and the radius of curvature pointing toward the fiber becomes very small $= b$. In order to maintain the low pressure at this location,

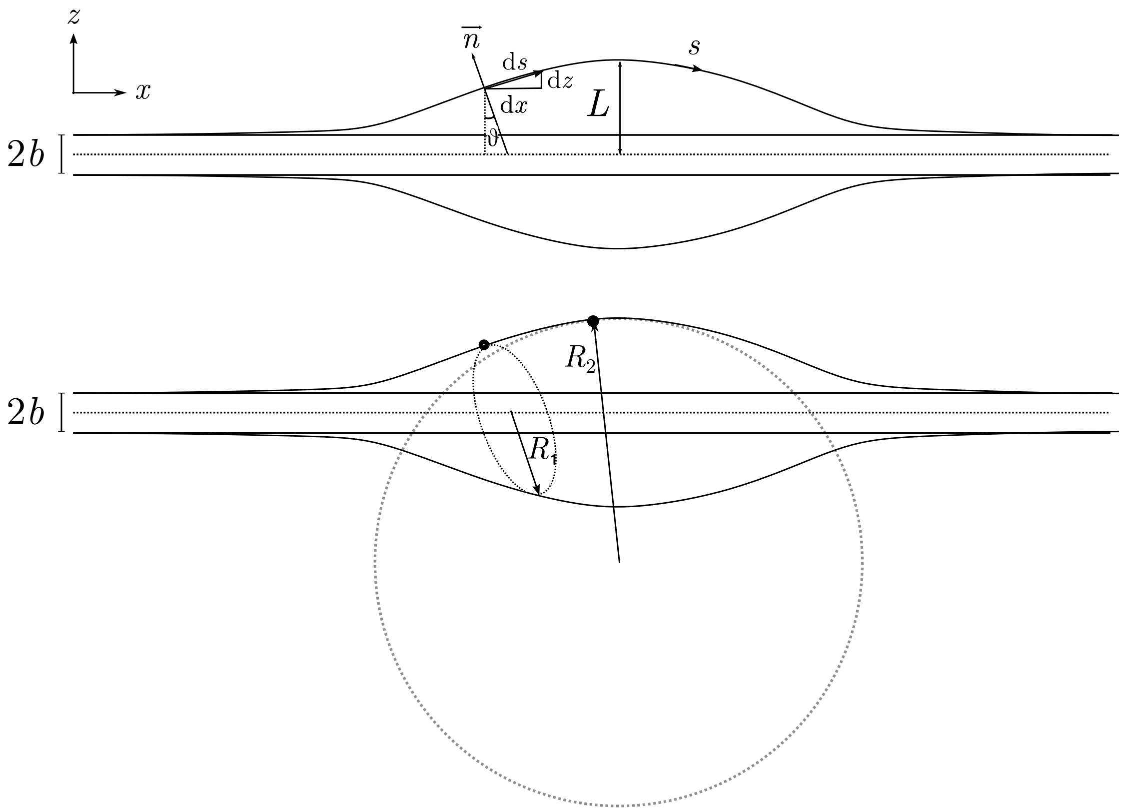

FIGURE 1.11: A diagram of a totally wetting droplet on a cylindrical, slender fiber of radius b. The surface of the droplet is traced out by the vector s and can be described by the horizontal coordinate x and vertical coordinate z. The surface normal $\vec{n}$ makes an angle with the vertical θ. The droplet has a maximum height of L. The lower panel shows example radii of curvature at the locations marked by the black dot for both the out of plane curvature R_1 and in-plane curvature R_2.

the radius of curvature in the other orthogonal plane must also become small but negative $\sim -b$ in order to keep the overall curvature low but still positive. Keeping in mind that the surface must have a constant curvature at any point on the surface of the droplet given by the Laplace pressure,

$$\frac{1}{R_1} + \frac{1}{R_2} = C = \frac{\Delta P}{\gamma}. \tag{1.35}$$

Moving along the surface of the droplet, the height z changes as a function of the position along the fiber x. Referring to figure 1.11, the outer surface of the drop follows a contour s. In addition, starting from the beginning point of the droplet, and moving from left to right, we can define two radii of curvature. Samples of the two radii are shown in figure 1.11 at two different locations. The first, R_1 is the radius of curvature that points from the normal of the tangent until it reaches the center of the axis line where $z = 0$. For instance, when $x = 0$, $R_1 = b$, at the center of the drop (the maximum point), $R_1 = L$. As z increases, so does R_1 and it is always pointing inside of the droplet, and thus always positive. R_1 can also be defined along the length of the droplet using s, and the angle between the normal of the drops surface to the vertical direction θ. Using trigonometry, we can see that $R_1 = z/\cos(\theta)$.

The other radius of curvature R_2 changes along the drop from the start to the middle. One can visualize this radius as though a circle is placed with the center lined up in the direction of the normal to the outer curve. At first, the radius of curvature is negative, meaning that it is concave out, which makes sense as the R_1 radius of curvature is small enough that it needs to be balanced out to maintain a low total curvature. Towards the center of the droplet along the x-direction, the radius reaches a point where it points inwards, creating positive radii of curvature. Using geometry, we find $R_2 = -ds/d\theta$.

There are now two radii of curvature defined with geometric parameters that we can insert into equation 1.35. Inputting the constraints gives

$$-\frac{d\theta}{ds} + \frac{\cos\theta}{z} = \frac{\Delta P}{\gamma}. \tag{1.36}$$

It is useful to change the coordinate system from s and θ to x and z. At the curve s, the two coordinates x and z can be related as $dz = ds \sin\theta$ and $dx = ds \cos\theta$. From trigonometry we also know that $ds = dx\sqrt{1+z'^2}$, where $z' = dz/dx$ and $z'' = d^2z/dx^2$, and that $\theta = \tan^{-1}(dz/dx) = 1/\left(1+z'^2\right)$. The differential equation becomes:

$$\frac{-z''}{(1+z'^2)^{3/2}} + \frac{1}{z(1+z'^2)^{1/2}} = \frac{\Delta P}{\gamma}. \tag{1.37}$$

This equation can be integrated once with respect to z to find

$$\frac{z}{\sqrt{1+z'^2}} - C = \frac{\Delta P z^2}{2\gamma} \tag{1.38}$$

.

Where C is an integration constant. Considering the edge of the drop, where $z = b$ and $z' = 0$, we can find that $C = b - \Delta P b^2/2\gamma$ and by evaluating at the maxima of the drop, where $z = L$ and $z' = 0$, we can also argue that the over pressure of the drop is going to be equal to [78]

$$\Delta P = \frac{2\gamma}{b+L}. \tag{1.39}$$

Therefore, the Laplace pressure in a drop on a fiber will depend on both the radius of the fiber and the radius of the drop.

I want to note that on a curved surface, like this fiber, a totally wetting droplet cannot spread out completely like it does on a flat surface. Spreading is not possible because of two conditions first that the surface area must not increase, and second that there must be constant pressure for everywhere on the drop. The section on the Plateau-Rayleigh instability (section 1.6.2) discusses the surface area condition in more detail.

1.5.4 Other equilibrium shapes for slowly moving drops

Along with surface tension affecting droplet shape by minimizing the surface area, the presence of other such forces can distort the shape of the drop.

Drops with large Bo will be able to be distorted by body forces that a small drop would not experience. For instance, the shape of a larger raindrop changes from a sphere to a rounded shape with one flattened side in the direction of motion [79]. As the drop falls, air resistance distorts drop, causing one side to flatten and the rest of the drop to bow away from a sphere. Distortion occurs because of the lower curvature; the Laplace pressure is not large enough to resist deformation for large drops.

Large air bubbles rising through a liquid bath will also distort. In this case, drag on the bubble is causing the distortion as it moves through the more viscous fluid. Unlike the stable raindrop shapes, the lower viscosity of the air in the bubble causes it to oscillate. Oscillations in the droplet shape can affect the path that the drop takes as it rises through the liquid bath, changing from a straight path to a zig-zag to a helix [80, 81, 82, 83]. Changing flow patterns happen when the bubble is in a turbulent flow and able to distort which requires that Re > 1 and Bo > 1. The changing shape also has an effect on a bubble or drop as it splashes when it impacts a surface [84].

The final equilibrium shape I will touch on is the shape of a drop on a conical fiber. Drops on conical fibers are discussed in the body of the thesis in Chapters 3-5 and the consequences of the shape are detailed thoroughly in Chapter 3. In this case, the drop is moving because of the shape of the fiber. We assume that motion is happening slowly, and the drop is only slightly perturbed from equilibrium. The radius of the fiber, b, is not constant across the drop, and instead there is a gradient in radius across the droplet. Based on equation 1.39, the pressure changes from the contact point of the fiber on the narrow end of the fiber to the other wider end. The gradient in Laplace pressure ∇P becomes [85]

$$\nabla P = -\frac{2\gamma}{(b+L)^2}\frac{\partial b}{\partial x}, \tag{1.40}$$

where γ is surface tension, x is the axial direction along the fiber and L is the droplet height. In the presented system in Chapter 3, we present an even more simplified case, where instead of Laplace pressure gradients across the entirety of the drop, we consider the difference in the capillary force from one end of the drop to the other.

1.6 Interactions between capillarity and hydrodynamics

At the length scales relevant in this thesis, fluid hydrodynamics and capillarity often interact in dynamical systems, and this gives rise to phenomena that make it easy to produce droplets. First, I will describe the method that I used to coat the fibers, either with the intent of creating droplets as discussed in Chapters 3-5. Depositing a film on a surface through dip-coating phenomenon is the same effect as when you dip a knife into a pot of honey, as you lift the knife out it will be coated by the viscous liquid, and the coating thickness depends on the speed at which it is pulled. The film left behind during the process of dip-coating is known as the Landau-Levich-Derjaguin film. Chapter 5 also explores the film that the droplet leaves behind due to the same phenomenon. Another interaction between capillarity and hydrodynamics that is exploited in this thesis is the Plateau-Rayleigh instability, which is a competition between hydrodynamic flow and capillarity. The Plateau-Rayleigh instability is responsible for breaking up a liquid coating on a fiber into droplets. The speed at which the film breaks up and the wavelength between droplets is well studied and can be used to distinguish material properties [86] and boundary conditions [87].

1.6.1 Landau-Levich-Derjaguin films

The Landau-Levich-Derjaguin film is a method of coating a solid surface with a partially wetting liquid, and it belongs to a family of wetting techniques called ‘forced wetting’ [88]. Creating a Landau-Levich-Derjaguin film involves submerging a solid substrate into a bath then pulling it back out of the bath. This technique is used frequently in industry (or when making a chocolate-dipped ice cream cone) to coat a substrate evenly by pulling the substrate out of the bath at a constant speed, a process known as dip-coating [89]. The key aspect of this coating method is that the meniscus is deformed as the substrate is drawn out of the bath, and the new shape of the meniscus is called the dynamical meniscus that has a length

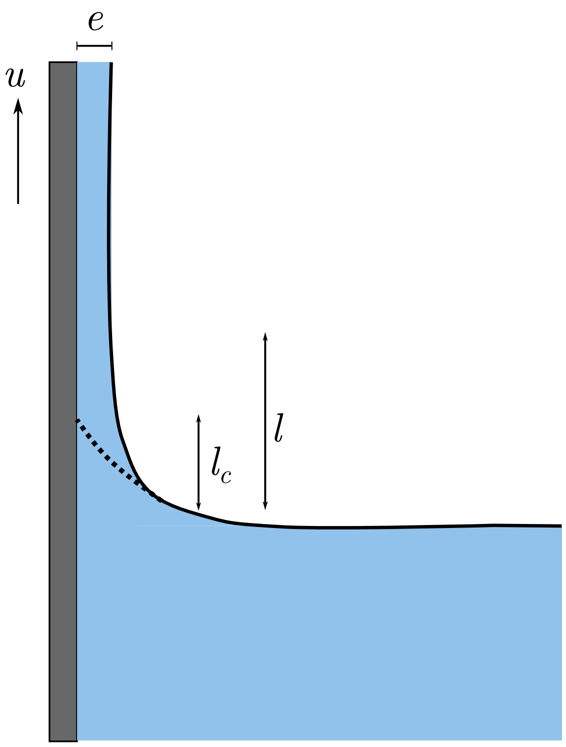

FIGURE 1.12: A diagram of a plate pulled out of a liquid bath at velocity u. A coating of thickness e covers the surface due to a difference in an entrained dynamical meniscus of length l compared to the static meniscus of length l_c. The film forms due to a balance between viscous entrainment and surface tension.

of l. The dynamical meniscus differs from a static meniscus that has a length l_c corresponding to the capillary length. A schematic of a plate being pulled out of a bath with velocity u creating a coating of thickness e is shown in figure 1.12. Note that the substrate is moving slowly so as not to cause inertial effects. Unlike a totally wetting material, which coats a substrate with a microscopic film, the Landau-Levich-Derjaguin (LLD) film would not exist without the motion of the substrate.

First I will describe the basis for coating a flat substrate before moving onto the more relevant cylindrical substrate. As one pulls a substrate out of a bath, the viscosity of the fluid will cause some of the liquid to be entrained by the moving substrate. Fluid entrainment is due to the no-slip boundary condition at the liquid-solid boundary because the liquid directly in contact with the substrate must move too. However, the surface tension will oppose the formation of extra interface.

Combining the idea that surface tension opposes the formation of the film, which is driven by the viscosity, we can make a scaling argument for the thickness of the coated film, e. Defining the rate that the substrate is pulled out of the bath as u, we now have all of the ingredients to make a scaling argument. The viscous force is $\sim \eta u/e^2$ in a method similar to that outlined in section 1.2.3. Using similar arguments, the capillary force will depend on Laplace pressure gradients from the of curvature of the dynamical meniscus. The curvature of the meniscus changes from a flat film to the $1/l_c$ to match the static meniscus, over the length of the dynamical meniscus l. The Laplace pressure gradient will therefore follow $\sim \gamma/(l\ l_c)$.

Setting the entraining viscous force to the same magnitude as the capillary force, we find

$$\frac{\eta u}{e^2} \approx \frac{\gamma}{l_c\ l}. \tag{1.41}$$

Currently, both e and l are unknown quantities but using the geometry of the film and the curvature we can compare the two length scales. The curvature at small slopes is approximately $\partial^2 z/\partial x^2$ and is proportional to e/l^2. The curvature is also constrained by the length of the dynamical meniscus $1/l_c$. Comparing the two values for curvature gives that $l \sim \sqrt{e/l_c}$. Combining these two constraints, we find that [34]

$$e \propto l_c \left(\frac{\eta u}{\gamma}\right)^{2/3} = l_c \mathrm{Ca}^{2/3}, \tag{1.42}$$

where Ca is the capillary number as derived in section 1.4.3

Here, the thickness of the film depends on the static capillary length and the ratio between viscosity and capillarity for a plate being pulled out of a bath. The faster the plate is pulled out of the bath or the more viscous the liquid, the thicker the film. Counter intuitively, the faster moving substrate entrains more liquid in the film rather than a slow-moving substrate.

A similar problem but with a slightly different geometry is the case of pulling a cylinder of radius b out of a bath. For slender fibers where $b << l_c$, the largest contribution to the curvature is now the radius of the fiber rather than the capillary length. As a result, our capillary force to viscous force balance is

$$\frac{\eta u}{e^2} \approx \frac{\gamma}{lb}. \tag{1.43}$$

Matching the dynamical to static meniscii condition now gives

$$\frac{e}{l^2} \approx \frac{1}{b}, \tag{1.44}$$

and combining these two conditions gives the thickness of the deposited film e, as is dependent on the fiber radius and capillary number,

$$e \approx b\mathrm{Ca}^{2/3}. \tag{1.45}$$

What is important to note here is that the scaling behaviour for a cylindrical fiber is the same as a planar structure in terms of the fluid properties and the speed of the substrate, but the curvature of the fiber dominates the prefactor rather than the capillary length. A deposited film on a slender fiber will always be thinner than a film on a flat substrate under the same conditions. So here the curvature in the radial direction plays an important role. One note is that for the coatings in Chapter 4, the thickness of the film is much thicker than the radius of the fiber, and we enter into a different regime where $e \approx (b + e)\mathrm{Ca}^{2/3}$ [34], and because $e >> b$ we see very little variation in the film thickness. We will see in Chapter 5 that when we consider the LLD film deposited by a droplet, the curvature of the droplet also is important to the deposition process.

1.6.2 Plateau-Rayleigh instability

If you turn on a water tap so that it forms a thin stream, you may notice that further down, it breaks up into droplets. The reason that the jet breaks up into droplets is because it undergoes a fluid instability called the Plateau-Rayleigh instability. Interestingly, it is present in both liquid jets, and in liquid coatings on a thin wire, where the presence of a solid core has little effect on the formation of the instability. Just like in the case of the droplet on a fiber discussed in

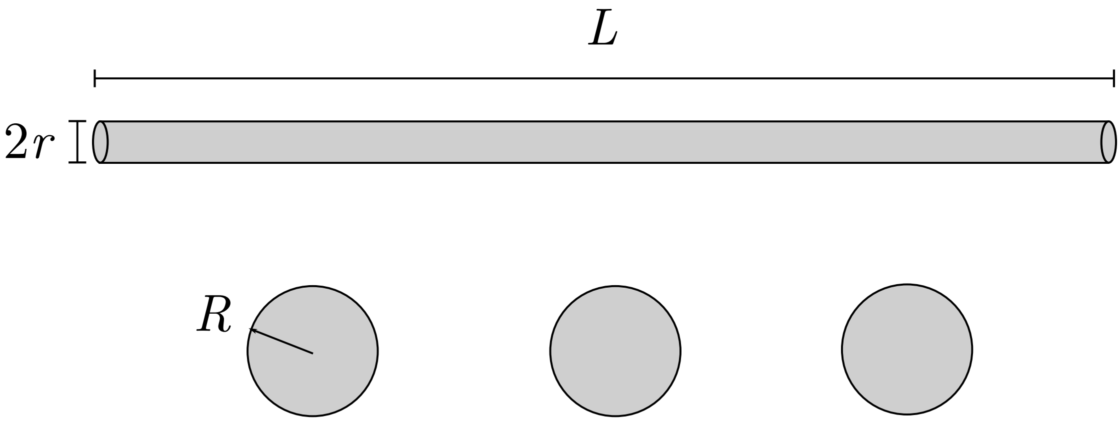

Figure 1.13: A cylinder with length L and radius r can be unstable and break up into spherical droplets of radius R if the conditions for minimizing surface energy are met through a rearrangement of fluid.

section 1.5, the curvature of the surface plays an important role in the dynamics of the process. We will first consider a jet breaking up into droplets to understand that when changing from a jet to a series of uniform droplets the surface area of the free surface is indeed reduced. Then we will consider the break up of a liquid sheath around a thin cylinder and work to understand the dynamics and the dominant wavelength that appears.

Consider a jet of fluid that has a radius r and a length L. Figure 1.13 shows the original configuration of the fluid and the geometry of the jet after it breaks up into droplets. The volume of this fluid will be $V = \pi r^2 L$, which is conserved as the jet breaks up into n droplets with radius R,

$$V = \pi r^2 L = \frac{4}{3}\pi R^3 n. \tag{1.46}$$

We can now compare the ratios of surface area for the drops S_n versus the surface area of the original jet S_j and this ratio gives

$$\frac{S_n}{S_j} = \frac{4\pi R^2 n}{2\pi r L} = \frac{2R^2 n}{rL}, \tag{1.47}$$

where we can substitute in the ratio of $n/L = 3r^2/4R^3$, from the volume conservation condition, to give:

$$\frac{S_n}{S_j} = \frac{3r}{2R}. \tag{1.48}$$

The ratio between surface area of the jet versus the droplets tells us that the surface area of the droplets will be less than the jet when the radius of the drop is more than 3/2 the radius of the cylinder. The condition proves that breaking a cylinder into droplets results in a decrease in surface area, and we can now consider the dynamics of such a breakup, *i.e.* what sets n.

Imagine a solid, thin cylindrical fiber with radius b that is coated with a liquid that has a thickness of e_0. The distance from the axis of symmetry to the surface of the the liquid is R (shown schematically in fig. 1.14). In many cases, this liquid coating is unstable (as anyone who has long hair that accidentally gets in their mouth and coated with saliva might know), small fluctuations in the surface of the liquid coating grow in amplitude and will break up into droplets. Break up is driven solely by surface tension and the Laplace pressure $\sim \gamma/R$. We will see that a wavy surface (shown in fig. 1.14), with average thickness e^* has a lower surface area than the original surface area of the cylinder, and a minimization of surface area drives the break of up this liquid coating.

We can start by defining a wavy surface as $e = e^* + \delta e \cos(qx)$, where δe is the amplitude of the perturbation that is a sinusoid with wave number q. Using conservation of volume, we can find $e*$. The volume of liquid in the cylindrical coating is $V = \int_0^\lambda \int_b^R \int_0^\pi z d\theta dz dx = \pi(R^2 - b^2)\lambda$, where λ is one wavelength.

The volume of liquid is conserved when the wavy perturbation forms, and it follows a similar integration

$$V = \int_0^\lambda \int_b^{b+e} \int_0^{2\pi} z \; d\theta \; dz \; dx = \left[(b+e^*)^2 + \frac{\delta e^2}{2} - b^2\right] \pi\lambda. \tag{1.49}$$

Setting the two volumes equal, linearizing, and rearranging, we find that average thickness of liquid layer is $e^* = e_0 - \delta e^2/4R$. Importantly, this relationship shows that the average thickness of the modulated film is less than the original thickness. From here we can now calculate the difference in energy between the wavy surface

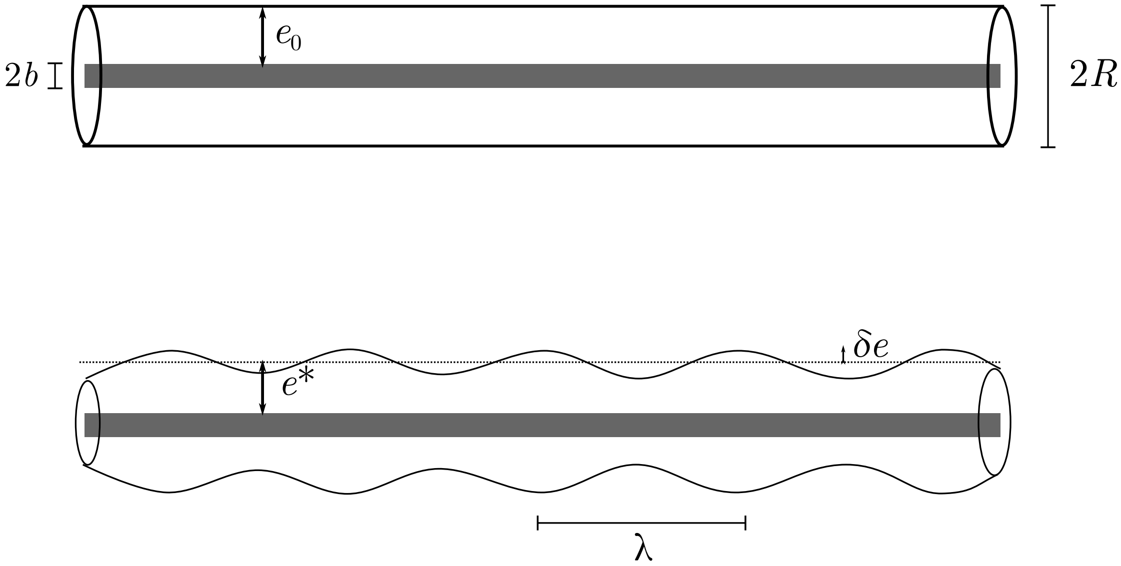

FIGURE 1.14: A liquid sheath of thickness e surrounding a fiber of radius b initially forms in a cylinder. Due to the Plateau-Rayleigh instability the cylinder will form a modulated surface with average thickness e^*, wavelength λ and modulation amplitude δe, as shown below.

and the straight cylinder because break up will be driven by a reduction in surface energy. For our system, the surface energy of a straight cylinder is

$$E_0 = 2\pi(b + e_0)\gamma\lambda. \tag{1.50}$$

The surface energy (or in this case the surface area) of the perturbed surface is a little bit less straightforward to calculate but begins with the general form

$$E_w = \int_0^{2\pi} \int_0^{\lambda} \gamma z \; ds. \tag{1.51}$$

Because we have the surface as a function of x not of the arc length s, we first convert ds to dx using the Pythagorean theorem, $ds = \; dx\sqrt{1 + (de/\, dx)^2}$ and if we assume de/dx is small, we can expand this to

$$ds \approx dx \left[1 + \frac{1}{2} \left(\frac{de}{dx} \right)^2 \right], \tag{1.52}$$

using a series expansion. Inserting the differential relationship into the integral for the surface energy

$$\begin{aligned} E_w &= \gamma \int_0^{2\pi} \int_0^{\lambda} (b+e) \left[1 + \frac{1}{2} \left(\frac{de}{dx} \right)^2 \right] dx \\ &\approx 2\pi\lambda(b+e^*) \left[1 + \frac{1}{4} q^2 \delta e^2 \right]. \end{aligned} \tag{1.53}$$

Now subtracting the two surface energies $\Delta E = E_w - E_o$ to find the change in energy from one geometry to the other, we can simplify by removing higher order terms of δe. What follows is the change in energy for this system to have a wavy surface

$$\Delta E = 2\pi\gamma\lambda \frac{\delta e^2}{4R} \left(R^2 q^2 - 1 \right). \tag{1.54}$$

A decrease in surface energy ($\Delta E < 0$) will happen when $R^2 q^2 < 1$, or in other words, when the wavelength is much longer than the radius. It is worth noting here that this stability condition for the wavelength is set by the total radius of the system regardless of the ratio of b and e. The dynamics, however, will depend on the ratio between the two. Now that we know the geometric constraints for the beginning of the instability, we can also look at the dynamics of the film break-up. We will assume that the fluid is in a viscosity dominant regime, the film is thin ($e_o << b$) and that the flow is driven by pressure gradients. This means that the system will be linearized and the approximation of $b \approx b + e$ will be made.

The curvature that gives rise to Laplace pressure is going to depend on the two radii of curvature, one being the radius of the fiber, and the other being the small variations due to the wavy surface. Assuming small slopes, the curvature can be written as

$$C = \frac{1}{b+e} + \frac{d^2 e}{dx^2}. \tag{1.55}$$

From here we can calculate the gradient in curvature dC/dx, which when multiplied by the surface tension gives the Laplace pressure gradients that will drive flow. The Laplace pressure gradient is

$$\nabla P = \frac{\gamma}{b+e_0} \left[(b+e_0)^2 q^2 - 1 \right] (\delta e \cos qx). \tag{1.56}$$

The flow through a segment of the film $Q \approx (e^3/\eta)(\partial P/\partial x)$ (see derivation at equation 1.11) can be related to the changing thickness of the film with time. As material flows from areas of negative to positive curvature, the thickness of the film must also change, $\partial Q/\partial x = -\partial e/\partial t$. Upon inserting the values for pressure and isolating for the changing amplitude of the film perturbation, we find

$$\frac{d\delta e}{dt} = \delta e \frac{\gamma e_0^3}{3\eta^2} q^2 (1 - q^2 b^2). \tag{1.57}$$

There are a couple of things worth noting from equation 1.57, first that the perturbation will grow when $qb < 1$, and second that the growth depends on the amplitude of the perturbation itself. We can presume that larger amplitudes will grow more quickly. The above equation however includes all values of q, which means that all wavelengths that meet the instability criteria are possible. However, we tend to see single wavelengths appear for given cylinder, and this is determined by the fastest growing wavelength.

Taking the derivative of equation 1.57 with respect to q and setting it equal to zero in order to find the maximum speed of growth, we find that $q^* = \sqrt{2}/b$ and relating back to the wavelength we find that the fastest growing wavelength λ^* depends only on the radius of the solid fiber in the thin film limit [34]:

$$\lambda^* = 2\pi\sqrt{2}b. \tag{1.58}$$

The dependence of the wavelength on b holds particular relevance to the work presented in Chapter 4 due to the changing radius of the fiber. The changing radius affects the spacing in between the droplets that form on a conical fiber. For systems with a thicker coating, a detailed derivation is conducted in work by Haefner *et al.* [87].

1.7 Suspensions

The final paper of this thesis in Chapter 6 considers the motion of small bubbles through a liquid rather than liquid droplets moving along a solid surface. Instead of considering how one continuous fluid flows in response to capillary forces, we are using capillary forces to stabilize the bubbles. In this section, I will discuss how the bubbles can be considered hard spheres and subsequently used as analogs for atomic structure, along with the physics behind keeping the bubbles stable, and how to make bubbles adhesive over short ranges.

1.7.1 Bubbles as hard spheres

As discussed in the Laplace pressure section (1.3.4), a curved interface has a pressure associated with the surface tension at the interface. When a spherical droplet is small enough, the pressure inside of the bubble or drop stabilizes the spherical shape. For example, consider an air bubble with a radius of ~ 30 μm in an aqueous bath of SDS and water, like the bubbles in this thesis. The aqueous bath and air has a surface tension of ∼35 mN/m [90]. The Laplace pressure of the bubble will have a pressure of ∼2500 Pa more than the liquid around it. For comparison, the difference in hydrostatic pressure across the drop $2\rho g R \sim 0.6$ Pa. Because of this large over-pressure to in the drop compared to the bath, the drops are stable and act as hard spheres. The hard sphere approximation has been proven to capture the first order behaviour of glassy materials, and bubble rafts have been used to mimic crystalline behaviour including packing of crystal structures, crystalline defects like dislocations [91, 92], and strength of adhesion [93].

1.7.2 Surfactants

To further stabilize the interface between the water and air, we can introduce a molecule known as a surface-active molecule, or a surfactant. A surfactant is an amphiphilic molecule that serves to decrease the cost of having an interface by lowering the interfacial tension. A surfactant is a molecule that straddles the interface, because one part will have a lower energy when interacting with one material, and the other part of the molecule will have a lower interaction energy with the other. By placing these molecules at an interface, the overall cost of having an interface is lowered and will allow for larger surface areas to exist for longer than it would otherwise be stable. Some everyday examples of surfactants include soaps, some polymers, phospholipids and some proteins, like the ones found in egg [94]. In this thesis, I use sodium dodecyl sulfate (SDS) as the surfactant to stabilize the air bubbles, Adding a surfactant to a water bath allows for the stabilization of air bubbles and subsequently allows for the production of small bubbles on the order of 30 μm in radius that are stable for time scales ranging from minutes to hours.

1.7.3 Micelles

If a critical concentration of surfactants is present in the solution, there is a tendency for the surfactants to self-assemble into structures to protect the solvent-phobic part of the molecule. A self-assembled structure that forms an enclosed aggregate with the solvent-phobic part of the molecule on the interior and solvent-philic part of the molecule on the exterior is a called a micelle. Micelles can form in a variety of shapes, but the most common are spherical micelles. The concentration that micelles begin forming at is known as the critical micelle concentration (CMC). The CMC can be calculated as a function of the difference in energy $\delta\epsilon$ between a lone monomer and a monomer in an optimally packed micelle $\delta\epsilon = \epsilon_M - \epsilon_1$, where ϵ_M is the energy of the monomer in the micelle and ϵ_1 is the energy of the lone monomer in solution. Derived nicely in Jones [1], the critical volume fraction ϕ_c of monomers in solution to spontaneously create micelles is $\phi_c = \exp(-\delta\epsilon/k_\mathrm{B}T)$ where k_B is Boltzmann's constant and T is the temperature. For SDS, the CMC is 8.3×10^{-3} M [95].

What is interesting is after the critical micelle concentration is surpassed, the concentration of micelles goes up, and the number of free surfactant molecules stays constant and low. The constant free surfactant concentration means that the surfactant molecules are successfully scavenged into micelles. Therefore, increasing the concentration of surfactant ends up increasing the concentration of micelles but not free surfactant molecules. Another effect worth noting is that increasing the amount of interface present in a system (*i.e.* by producing a foam) will reduce the amount of surfactant in solution and may depress the known amount of concentration of micelles from a low interface system [96].

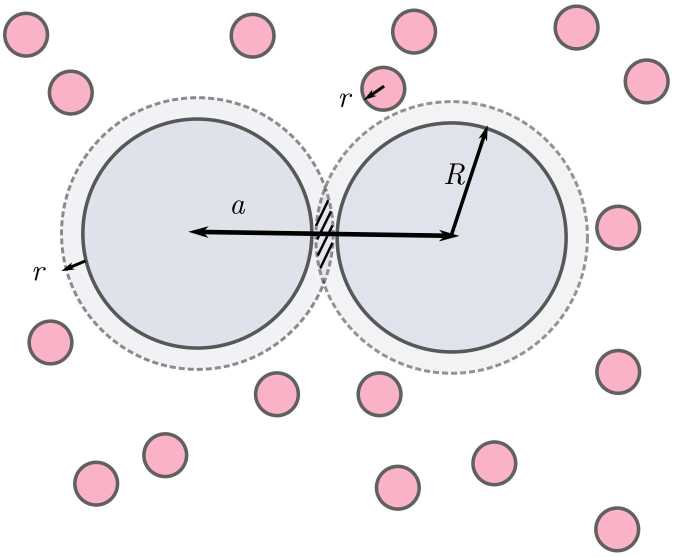

FIGURE 1.15: Two large colloidal spheres of radius R that are surrounded by small particles of radius r. A thin spherical shell surrounds the large particle to indicate the excluded volume. The two large particles are close enough for the excluded volumes to overlap as indicated by the hatched area.

1.7.4 Depletion forces

A depletion force refers to an entropy-driven force that comes from having large and small particles in a solution. Figure 1.15 shows a schematic of two large particles surrounded by small particles, that are separated by a distance a. Assuming the differently sized particles are spherical and are unable to overlap, there is a spherical shell around the large particles in which the center of the small particles may not reach, this volume is known as the excluded volume and for two large particles of radius R and small particles of radius r, the excluded volume V is [97]

$$V = \frac{8\pi(R+r)^3}{3}. \tag{1.59}$$

The excluded volume is valid when the large particles are far away from one another (*i.e* $a > 2(R+r)$). As two large particles diffuse in the solution, if they get into close enough proximity, the two excluded volumes begin to overlap. The overlapping volume decreases the total amount of volume, V_{dep} that is excluded from the small particles, which can be calculated based on the separation distance a between the two large particles [1].

$$V_{\text{dep}} = \frac{4\pi}{3}\left(R+r\right)^3\left(1 - \frac{3a}{4(R+r)} + \frac{a^3}{16(R+r)^3}\right). \tag{1.60}$$

The increase in available volume serves to increase the entropy of the system, because the small particles gain translational entropy due to the increased number of configurations available. Thus, the large particles attract. It is noted that the depletion forces cause a short-range attraction and become important when the large particles come within a distance on the order of the size of the small particles. In this work, the micelles discussed in the previous section are used as the small particles and the larger particles are the air bubbles. We can model it generally by considering the micelles as a dilute, ideal gas. The micelles will exert an osmotic pressure given by the ideal gas law

$$P_{\text{osm}} = \frac{N}{\Omega}k_bT, \tag{1.61}$$

with N micelles in a volume Ω with the temperature of the solution T. The resulting force due to the osmotic pressure is

$$F_{\text{dep}} = -P_{\text{osm}}V_{\text{dep}} = -\frac{N}{\Omega}k_bT\frac{4\pi}{3}\left(R+r\right)^3\left(1 - \frac{3a}{4(R+r)} + \frac{a^3}{16(R+r)^3}\right). \tag{1.62}$$

The depletion force is small, but always attractive. Because it also depends on the number of micelles in solution, the depletion force increases with micelle concentration [93].

1.8 Buckling and coiling

Coiling and buckling of slender structures happens when a slender object is subjected to a compression along the axial direction. Typically, the compressive force can be alleviated when the fiber buckles to reduce the length along the direction of the compression at the cost of bending the fiber. This is something we do everyday when we style hair, fiddle with headphone cables, or twirl pasta around a fork or chopsticks. Beyond the everyday, there are important applications that bound over several length scales, including bending of partially molten rock layers during mountain building events on geologic scales [98]. The stability of slender beams are important in bridge building and other civil engineering endeavours [27]. Laying down hose, like in installing underwater cables requires a specific handling of the cable to prevent costly buckling and twisting [99]. We also see buckling in regards to 3D printing techniques as a way to manufactures meta-materials at very low costs [100, 101, 102]. Understanding the fundamentals of coiling can provide a coarse-grained understanding of self-assembly of proteins and DNA structures [103, 104].

In the final paper, I present work examining the buckling of air bubbles attached in a chain. Much of the theory presented in Chapter 6 was inspired by the work from coiling theory, both for coiling of solid and viscous liquid threads [98, 105, 106, 107], however in working through the relevant parameters of the system, I found that there were some key differences, the first was that instead of the buckling being due to a barrier that applies a compressive force, it was due to the viscosity of the liquid bath in which the chain was moving. Buckling can arise due to viscous drag, which is when a slender object is pushed through a viscous liquid and the drag on the object causes an instability that results in a bending torque [108].

Common to these subtopics is the idea that a long, thin, flexible uniform structure is fed at a uniform speed. When faced with either a barrier or a frictional force, a compressive force results and the slender structure is forced to buckle and bend. In some cases, it can wind with a regular radius and frequency if the speed, stiffness, and feed height are constant. Here, I will first describe the conditions required for buckling a viscous thread and compare how this applies to solid threads. I will discuss how the balance between viscous forces and gravitational forces result in a set radius and frequency of coiling before describing drag-induced coiling.

1.8.1 Viscous coiling

When preparing a piece of toast with honey, you may be inclined to let the honey flow off the knife or spoon and onto the bread rather than fighting the viscosity to spread it onto the surface of the toast (and to prevent toast crumbs from infiltrating the honey). When you do this, you may notice that the radius of the streaming honey decreases the higher you hold it and the honey begins to whirl around itself in a coiling pattern, like shown in figure 1.16a). The reason that it does so is because the timescale that gravity causes the viscous thread to impact the surface is too fast for the viscosity of the liquid to flow in response. In this section, we will derive the two relevant timescales due to the viscous force resisting bending and the gravitational driving force before calculating the radius of coiling and the frequency.

For a liquid thread falling from height H with viscosity η and density ρ, it will fall with a flow rate Q based on the radius of the thread r (shown in figure 1.16b)). The thread will fall with a characteristic timescale τ_g due to gravity that can be derived from kinematics

$$\tau_g = \sqrt{\frac{H}{g}}, \tag{1.63}$$

where g is the acceleration due to gravity. The viscous timescale, on the other hand is derived by considering the time it would take for one fluid molecule to diffuse across the radial direction of the fiber. Based on a random walk, the viscous timescale τ_η is

$$\tau_\eta = \frac{r^2\rho}{\eta}. \tag{1.64}$$

We can see that $\tau_\eta >> \tau_g$ when $H >> r$, which means we can define a slenderness ratio $\epsilon = r/H$ and we will expect to see coiling when the ratio is small. When the gravitational timescale is less than the viscous timescale, the viscous fluid cannot flow fast enough when order to alleviate the stress of the thread impacting the barrier. The fastest way for the system to relieve the excess length is to have it behave like a solid and form a coil.

The radius of the coiling can be predicted using a simple force balance. The gravitational force on the rope per length is $F_g \sim \rho g r^2$. The viscous force is $F_\eta \sim \eta U r^4/R^4$ which arises due to a bending torque on the thread for bending with a radius R. Balancing these two forces, the radius of the coiling gives

$$R \sim (\eta U r^2/\rho g)^{1/4}. \tag{1.65}$$

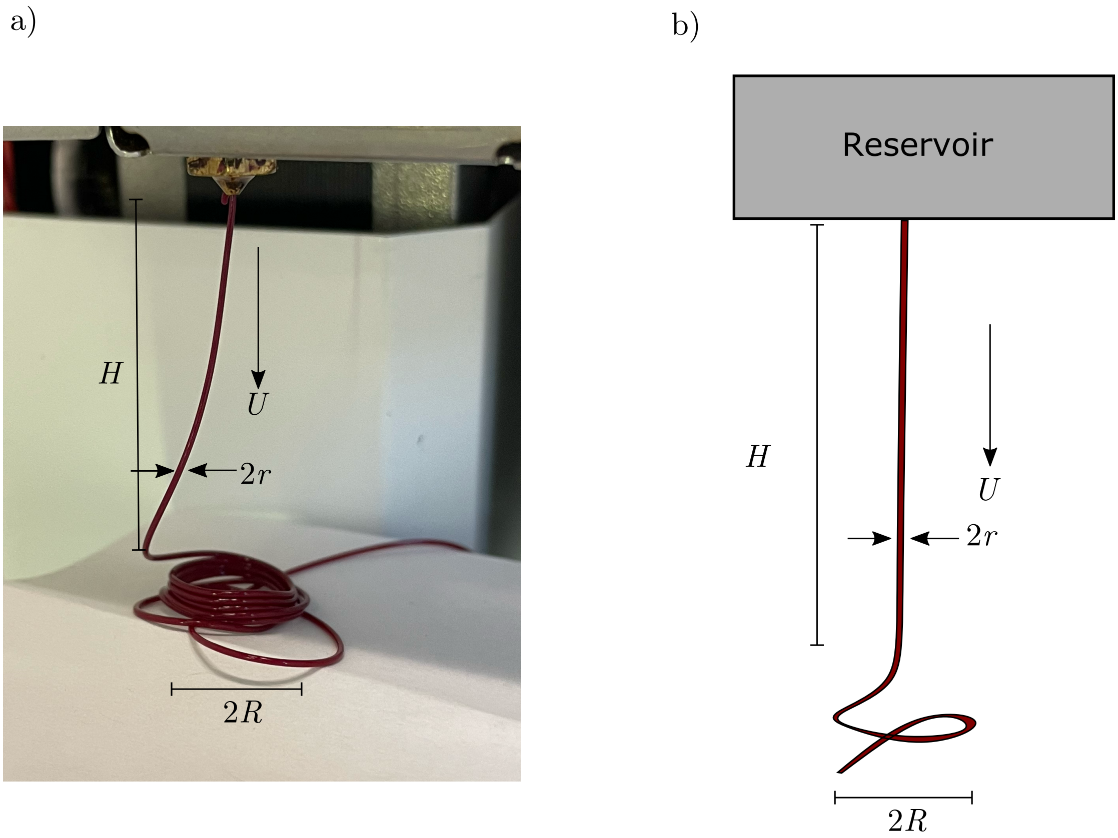

Figure 1.16: a) An image of an extruded plastic thread from a 3D printer undergoing a coiling as it impacts a piece of paper. b) A schematic of a thread of liquid with radius r falling from height H at speed U onto a surface. The thread begins to coil with a radius of R.

We can see that the coiling radius will depend on the radius of the thread and the speed that the thread is moving when it impacts the surface. To translate into an experimentally measurable parameters, we can consider the flow rate. The flow rate of the liquid out of the reservoir Q, which we know from continuity must be constant where the thread impacts the surface as well, which means that $Q \sim Ur^2$. The continuity constraint reduces equation 1.65 to $R \sim \nu^{1/4} Q^{1/4} g^{-1/4}$ where ν is the kinematic viscosity. Rearranging instead for the coiling frequency $\Omega = U/R$, one can find that the frequency is

$$\Omega \sim Q^{4/3} r^{-10/3} \nu^{-1/3}. \tag{1.66}$$

To compare to a solid rope with a bending stiffness of Er^4 where E is Young's modulus for the fiber, we can simply swap out the viscous force for a solid bending force altering it to $F_b = Er^4/R^3$. Otherwise the theory is the same, and it can be shown that a viscous liquid and solid rope will coil in the same manner. Where the radius R_b now scales as

$$R_b \sim \left(\frac{Er^2}{\rho g}\right)^{1/3}. \tag{1.67}$$

Note here that the bending radius does not depend on the speed that the rope impacts the surface.

In the system presented in Chapter 6 of a buckling chain of bubbles is quite different than the above system because there is no viscosity nor bending to stabilize the chain, and we see buckling far away from any barrier.

1.8.2 Drag induced coiling

In contrast to the previous example, where buckling is induced due to a difference in timescales, in this section we consider buckling due to viscous drag. Heavily inspired by the work presented by Chakrabarti *et al.* [109], we can compare the bending torque exerted by viscous drag that drives the buckling and bending energy of a solid fiber that resists the bending. If a thin fiber is extruded into a bath with a constant speed, U, where the viscosity of the bath is η. Based on the bending stiffness of the fiber Er^4, it will resist bending such that it has has a bending force of $F_b = Er^4/R^2$. Viscous force from the ambient fluid will be $F_\eta = \eta\, UR$ which results in a bending radius R_d of

$$R_d \sim \left(\frac{Er^4}{\eta U}\right)^{1/3}. \tag{1.68}$$

Compared to the gravitationally-induced coiling in equation 1.67, the speed of the extruded fiber is important to the radius of the coiling. The faster the speed, the larger the buckling amplitude. Drag-induced coiling is a good starting point for the system presented in this thesis, however, there is no bending stiffness to stabilize the chain of droplets. Instead, as outlined in Chapter 6, we find that viscous drag serves to both drive the buckling and also stabilize the buckling.

Chapter 2

Experimental Details

This section elaborates on the experimental techniques used in the papers presented in Chapters 3-6. Although each paper has a short methodology section, they are concise. The goal here is to write an experimental methods section that is clear enough so that a future undergraduate or graduate student working in the Dalnoki-Veress group can understand these techniques with enough clarity to replicate the results that I have produced. First, I will describe the fabrication of glass micropipettes which are used as the conical substrates in Chapters 3-5, and are used to produce the bubbles in Chapter 6. I will then describe two different methods for producing and placing droplets, followed by the method for producing air bubbles using the micropipettes. Finally, I will discuss the different image analysis techniques that I used to extract the relevant data from optical microscopy images.

2.1 Fabricating micropipettes

A technique used in all the papers in this thesis is the process of pulling glass micropipettes. A glass capillary with an inner diameter of 0.7 mm and an outer diameter of 1 mm (World Precision Instruments) is clamped on both ends (Figure 2.1a)) and an electromagnet exerts a force to pull on one end of the capillary while the other is held fixed. A middle location on the pipette is heated using a platinum filament and when the glass transition temperature is reached, the glass becomes a viscous liquid. Once a liquid, the fluid is no longer able to sustain

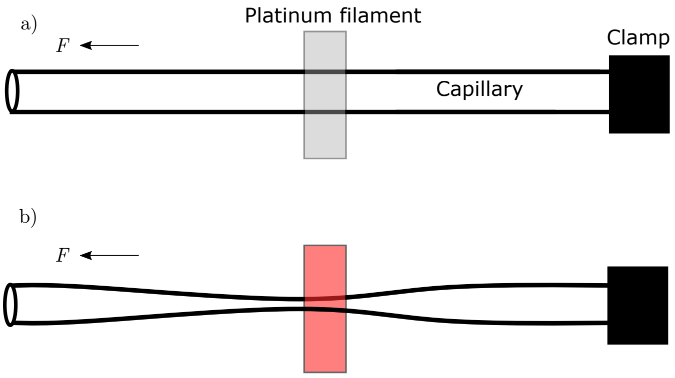

Figure 2.1: Schematic of pulling a glass capillary into a micropipette using a platinum filament. The capillary is clamped on the right side, the filament is positioned over the center of the capillary and a force F pulls on the left side of the capillary. a) An unpulled capillary before the platinum filament is heated. b) The pipette after being pulled. The filament heats and locally melts the glass, and the applied force pulls the two sides of the capillary apart, stretching the heated portion of the capillary to create a micropipette.

the pulling magnetic force and the two ends of the pipette pull apart as shown in figure 2.1b). The highly viscous fluid stretches and thins as the two ends are separated, resulting in a narrow diameter at the location of the filament that smoothly tapers to the original diameter of the capillary. The pipette cools as it moves further from the platinum filament and re-solidifies, halting any further flow. The shape of the resulting pipette can by tuned by changing the strength of the magnet and the temperature of the filament [110].

Typically, pulled micropipettes are used in patch clamping techniques, wherein extremely thin pipettes are used to probe the inner workings of living cells [111, 112]. In our lab, we try to pull a long, slender pipette that is ∼3 cm in length with the tip of the pipette being ∼30 μm in diameter. The pipettes are so thin that the glass bends easily if any force is applied to the sides, like a Hookean spring, and therefore can be used as force sensors. Previous work has found that these pipettes are sensitive to tens of pico-Newton precision [113, 114]. These pipettes are incredibly versatile, and have been used by the Dalnoki-Veress lab and others for a variety of techniques, including making monodisperse oil droplets using the snap-off technique [115], measuring adhesion forces of cells on surfaces [116], measuring exerted forces of living organisms [117, 118], and measuring the force required to translate droplets on a surface [114], along with many other applications. In this section, I will describe the ways in which I used the micropipettes.

In this thesis, I studied how oil droplets travel along conical glass fibers. To prepare the micropipettes, which are used as the glass fibers, I would first clean the outside of glass capillaries using acetone before putting them in the pipette puller (Narishige PN-30). Cleaning the surface of the capillaries is important because any dust or imperfections on the surface could cause pinning of the oil droplet as it translates across the substrate. When the micropipettes are used as conical glass fibers, the radius of the fiber would range between $\sim$ 20 - 150 μm. When used as a conical fiber, the micropipettes do not need to be manipulated any further.

In the final paper included in this thesis (Chapter 6), the shape of the micropipettes needed to be altered. Due to the chamber geometry, the narrow tip of the pipette needed to be bent. This can be done using a heated platinum wire. Figure 2.2 a) shows the pipette before it is bent. Figure 2.2b) shows the glass of the thin section of the micropipette bending when it is brought into contact with the hot wire. The heat from the wire locally melts the glass of the pipette enough for the glass to bend. Using a pair of tweezers in conjunction with the wire as bending template, the micropipette can be manipulated into a variety of shapes. Cooling the wire sets the shape of the pipette, and if done carefully, this can result in a micropipette bent into precise shapes. One important technical aspect to reduce the chances of the molten glass sticking to the platinum wire and breaking as a result, it was helpful to reduce the temperature of the platinum wire first before attempting to move the pipette away. Lowering the wire temperature meant that the as the molten glass solidifies, the thermal expansion coefficient of the platinum shrinks the wire, which separates the platinum and glass.

To make the small air bubbles required in Chapter 6, I required a smaller orifice than the standard range of radii that are easily obtained in the standard pulling process. As a result, I developed a 'double-pulling' technique that involved taking a pulled micropipette and thinning the end further. Double-pulling is done by

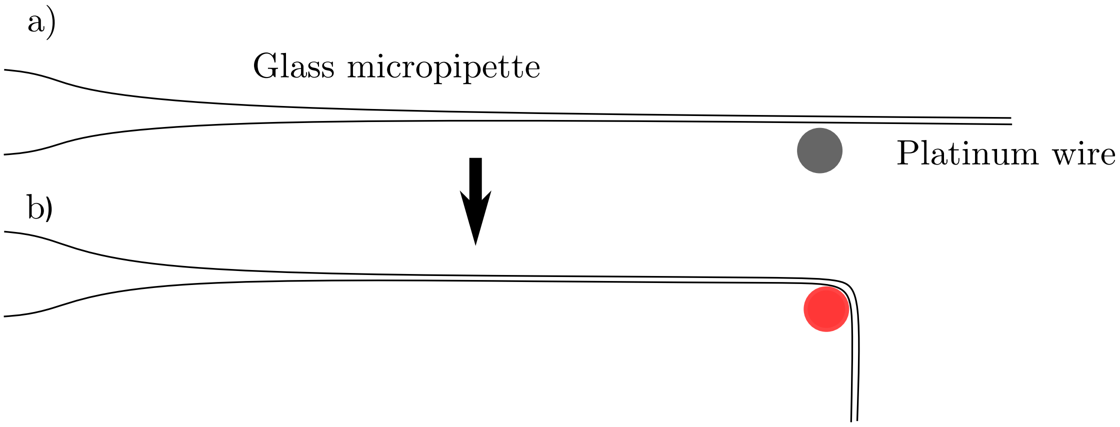

Figure 2.2: A glass micropipette bending due to a heated platinum wire. a) A straight glass micropipette after being pulled. b) The micropipette tip is bent on the heated platinum wire by locally heating one spot on the fiber.

locally heating the tip of the pipette using a platinum wire. The process for double pulling is shown in figures 2.3a) and b), where the best technique to reproducibly narrow the pipette orifice was to heat the tip of the pipette on one side. Once the pipette glass melts, it can be pulled away from the wire which further narrows and elongates the pipette tip, just as though the pipette were being pulled a second time on the micropipette puller. Asymmetric heating was key to the interior of the pipette elongating and narrowing as illustrated in figure 2.3b). Heating the pipette on one side allows an uneven melting across the narrow tip of the pipette, which allows for a less viscous melt at the point in contact with the platinum wire. The less viscous melt stretches out more quickly than the cooler, more viscous end of the pipette, allowing for the tip of the pipette to stretch out asymmetrically. This method produces air bubbles as small as 7 μm in radius. If the pipette tip were brought into contact with the wire such that the face of the orifice is heated (shown in figure 2.3c), the tip would rapidly melt closed and upon pulling the pipette the solid glass would narrow and extend. Once clipped to allow for air to be able to flow through the micropipette, the inner diameter would be the same as if the pipette were pulled once and would create bubbles larger than the targeted size.

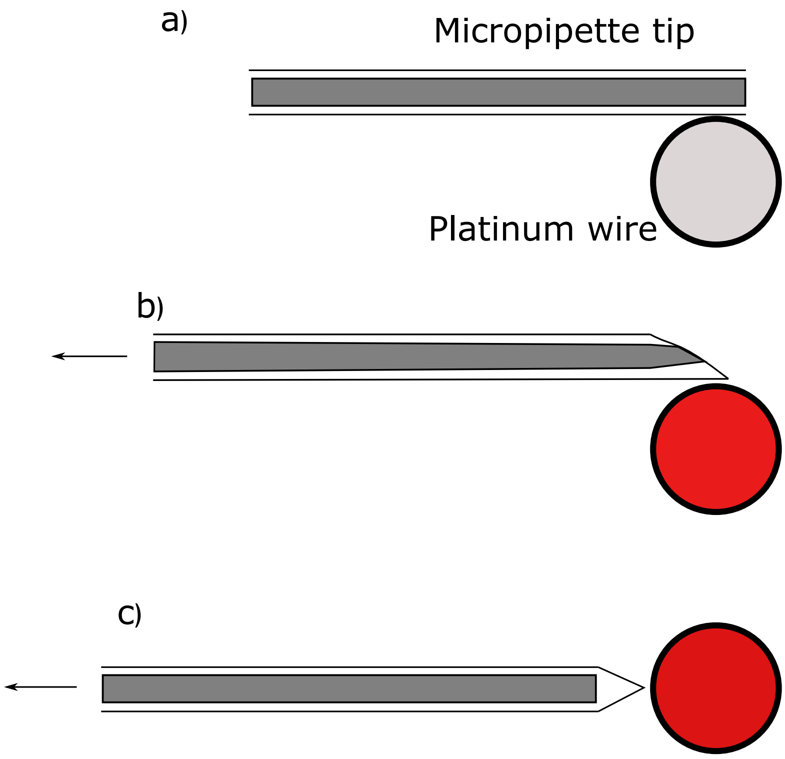

FIGURE 2.3: A schematic of the double-pulling pipette process. a) A magnified view of the narrow end of a micropipette near an unheated platinum wire. b) The most reproducible manner of double-pulling a micropipette, where the bottom edge of the pipette is brought into contact with the hot platinum wire before being pulled away. The tip stretches and draws the orifice to be narrower. c) A method of double-pulling that does not result in a narrower orifice. When a pipette tip is brought face on to the wire, the end of the glass rapidly melts and when pulled does not result in a narrower orifice.

2.2 Making droplets

Chapters 3-5 present research studying droplets on conical fibers. In this section, I will outline the two techniques for making droplets which include creating and transferring single droplets and creating multiple droplets using a combination of dip-coating and the Plateau-Rayleigh instability. All of the droplets were made with silicone oil because it is non-hygroscopic, non-reactive in air and totally wets glass. In addition, silicone oil was used because it is possible to change the viscosity of the liquid without changing the material chemistry; we have used viscosities ranging from 1000 cSt to 5000 cSt for the projects presented in this thesis.

2.2.1 Individual droplets

When it was necessary to place individual droplets onto a conical fiber in Chapters 3-6, we developed a technique of producing a droplet on an auxiliary pipette then transferring the droplet to the pipette used as a substrate. The auxiliary pipette is connected to a syringe and a small volume of fluid is extruded from the tip. The extruded volume will travel up the length of the auxiliary pipette and will form into a barrel-shaped droplet. This droplet can then be transferred to the primary pipette by bringing the two pipettes into contact at the location of the droplet. The auxiliary pipette is then moved to 'brush' the droplet onto the primary pipette. The droplet will transfer from one pipette to the other when the droplet is on a thinner pipette than the target pipette, because of the wetting conditions between the droplet and substrate. This technique allows for droplets to be placed at a desired location on the primary pipette. One downfall of this technique is that it is not possible to extrude droplets of extremely viscous liquids. To extrude viscous liquids from the end of a narrow micropipette requires too high of a pressure than can be supplied by hand from a syringe. To overcome this for more viscous liquids, we continue to use an auxiliary pipette to produce droplets using a technique outlined in the next section.

2.2.2 Multiple droplets

Multiple droplets can be produced at one time using a combination of the Landau-Levich-Derjaguin film deposition and the Plateau-Rayleigh instability. This technique works particularly well when trying to make droplets with an extremely viscous liquid. A submerged fiber is pulled out of a liquid bath and the viscous liquid will coat the fiber according to the Landau-Levich-Derjaguin relation. The thickness of the liquid coating will depend on the fiber radius, pull speed, viscosity, and surface tension. If the film is thick or if timescales are long, the film will break up into droplets due to the Plateau-Rayleigh instability. On a conical fiber the fiber radius is not constant, and this causes droplets with a range of sizes to form. The droplets are ordered so the small droplets form at the narrow tip of the fiber and large droplets form at the wide base.

Droplets can be made in a variety of sizes in an uncontrolled manner by simply holding the pipette and pulling if out of the bath by hand. The irregular coating breaks up into droplets that can be transferred to the primary pipette using the transferring technique described in the previous section. In Chapter 4, I studied the break up of a liquid film on a conical fiber, which required a uniform film thickness along the fiber. The film thickness can be controlled by pulling the pipette out of the bath at a constant speed using a translation stage. The tip of a Pasteur pipette was filled with silicone oil and used as a reservoir for these experiments. The Pasteur pipette was mounted on a translation stage. A schematic of the experimental set up is shown in figure 2.4. The conical fiber was inserted into the reservoir, and the Pasteur pipette was moved at a constant speed between 500 μm/s to 2000 μm/s to deposit a film on the fiber. At these speeds, film coatings ranged from 13-88 μm. The film then breaks up into droplets at a time scale and wavelength set by the fiber radius, the film thickness, viscosity, and surface tension.

Interestingly, we found that it was possible to nucleate film break up by holding the reservoir at a set location near the tip of the fiber (as shown in figure 2.5). The meniscus between the bath and fiber created a slight perturbation in the surface of the film, which created a cascade of droplets along the fiber. Nucleating the

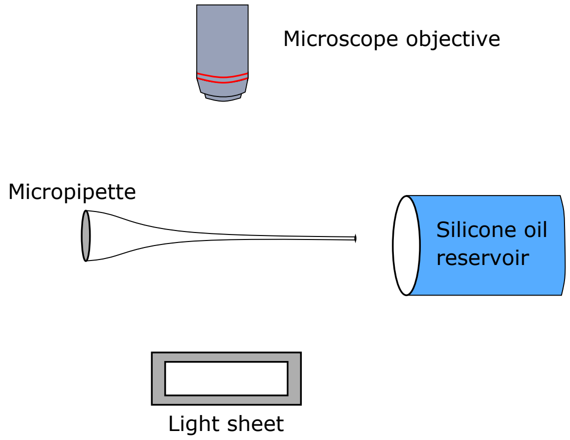

FIGURE 2.4: The experimental set up for droplet on conical fiber experiments. A glass micropipette is held horizontally and imaged from above with an optical microscope. A light sheet illuminates from below and a reservoir mounted on a translation stage is lined up with the narrow end of the pipette.

film break up reproducibly creates droplets with fixed sizes at fixed locations; a phenomenon that could be used for self-patterning applications.

2.3 Making bubbles

In Chapter 6, small uniform bubbles are produced in an aqueous bath. The aqueous bath includes a depletant which makes the bubbles adhesive over a short range and the bubbles can therefore be linked together in a chain. In this section, I will

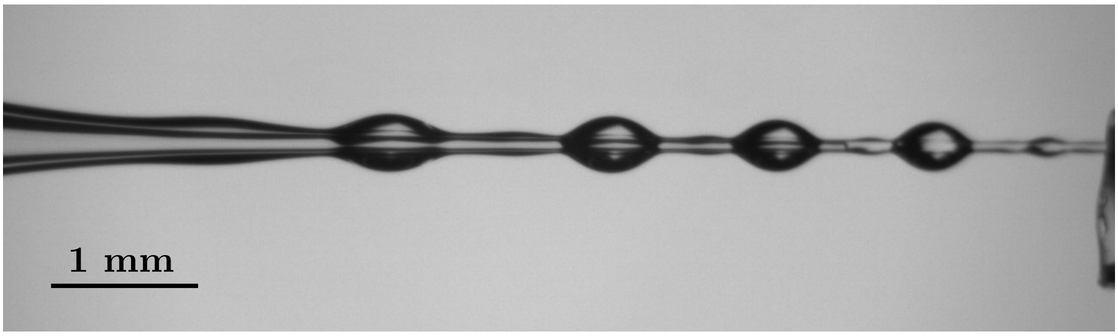

FIGURE 2.5: A sample image of the break up of a liquid film on a conical fiber. The reservoir is held at the right side of the image to nucleate the droplets at fixed locations.

discuss the method in which I create the bubbles as well as discussing the details of the aqueous bath.

Air bubbles are produced by extruding air through a double-pulled micropipette into an aqueous bath. The air pressure to create the bubbles was controlled using a 10 mL syringe as an air reservoir, which was then connected to the micropipette with tubing. The pressure was set by both the depth that the micropipette was submerged in the solution as well as the pressure applied to the syringe plunger. To ensure a constant pressure during the course of each data set, a motorized translation stage was used to apply a pressure to the end of the plunger on the syringe. Because the air reservoir was large in comparison to the flow of air through the micropipette, it is assumed that the pressure is constant over each data set. Constant pressure is confirmed by comparing the size of the bubbles at the beginning of the sequence to the size of the bubbles at the end. Air, being a compressible fluid, will create larger or smaller bubbles depending on the back pressure in the bubble blowing pipette [70, 119].

The solution that the bubbles are produced into is crucial to the small size, stability, and adhesion of the bubbles. The surfactant, sodium dodecyl sulfate (SDS, Bioshop) is added to water to stabilize the bubbles as they are extruded from the pipette. If the concentration of SDS is too low, large bubbles will form. As discussed in section 1.7.2, the surfactant migrates to the interface and lowers the interfacial tension. In addition, SDS is a depletant and SDS concentrations were varied to examine the effect of adhesion strength on chain behaviour [93]. The concentration of SDS ranged from 1% to 8% by weight in solution, and also contained 1.5% NaCl (Caledon) to screen electrostatic charges.

2.4 Imaging and data analysis

For each of the research projects presented in this thesis, data was collected using optical microscopy. This section details the experimental set up used to collect the images and the image analysis techniques used.

2.4.1 Imaging set ups

The first step to extracting quality data from optical microscopy images to ensure that the images and lighting are of high quality to produce crisp, well-contrasted images. There were two main optical microscopy set ups made for this thesis, one for experiments with oil droplets on conical fibers and one for the moving bubble chain experiments.

The experimental set up for studying droplet motion on conical fibers consists of a conical fiber held horizontally. The camera (ThorLabs, USB2.0 Digital Camera) imaged from above and a light sheet (Advanced Illumination, Side-fired Backlight) provided uniform lighting from below. A schematic of the set up is shown in figure 2.4. This geometry was found to provide the highest level of contrast between the fiber and the background. Depending on the required magnification, lenses ranging from a magnification of 2x to 10x were used. The 10x lens (Olympus) was used to measure the thickness of the deposited film in Chapter 5, where the 2x lens (Navitar) was used to look at longer length scale behaviour presented in Chapter 4.

In Chapter 6, the geometry of the system required imaging that allowed for 3-dimensional reconstruction. Due to the speed that the system was moving, a single camera and mirrors were used to ensure that orthogonal planes of the system were imaged synchronously. Shown in figure 2.6, I developed chambers that allowed for simultaneous imaging of two orthogonal planes. Using a resin 3D printer (Phrozen Sonic 4k), I created a chamber with two edges at a 22.5° angle from the flat imaging plane. Silicon wafer pieces were attached to the two angled edges using a two-part epoxy, which served as reflective mirrors. The chamber was then attached to a microscope slide to create a closed environment to hold the aqueous bath described in section 2.3. An object in the center of the chamber can be imaged in two planes orthogonal to each other by focusing on the reflections in the mirror rather than the object itself. An example of the chamber with bubbles can be seen in figure 2.6a), where the front view shows a bent micropipette produces bubbles in the center of the chamber. The reflections are shown to the left and right of the central bubble chain. Reflections of the micropipette are left out of the schematic for clarity. Figure 2.6b) shows the imaging set up from the top, where the chamber was lit

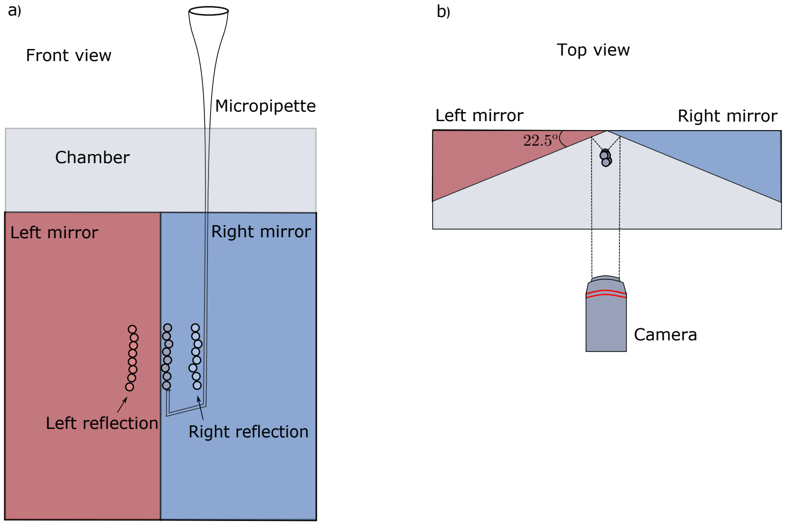

FIGURE 2.6: Experimental set up for a bubble chamber with two mirrors held at a 22.5° angle from a flat plane. a) Front view of the chamber shows a bent micropipette is inserted into an aqueous bath. Bubbles are produced in the center of the chamber (grey) and reflections from the left (red) and right (blue) as shown with the pipette reflections omitted for clarity. b) The top view of the chamber with the two mirrors held at 22.5° angle from a flat plane. The optical microscope focuses on the reflections to image two orthogonal planes. Sample ray traces are also shown.

and the camera imaged through the microscope slide. Two light sheets (Nanlite) were used to illuminate each mirror evenly. A 2x objective lens (Edmund Optics, 0.13 NA, Ultra Compact Objective) was used with a CMOS camera (Teledyne FLIR, Blackfly). Images were taken at a frame rate of 150 frames per second.

2.4.2 Image analysis

For each of the projects in this thesis, data collection was primarily conducted through optical microscopy. To extract the data from the optical microscopy images, image analysis needed to be done. All of the analysis was conducted using the python coding language, of which I wrote analysis scripts and implemented open-source image analysis packages.

In Chapters 3-5, I used edge detection to distinguish between fiber and droplet system from the background. I used a Sobel edge detection algorithm (`sobel` from `skimage.filters` [120]), which detects edges based on the intensity gradients in each direction of the image. Sharper gradients indicate a highly contrasted edge, and an edge is defined by thresholding the gradient values to only consider sharp gradients. Figure 2.7a) shows a representative image of silicone oil droplets on a fiber, and figure 2.7b) shows the edges detected using the edge detection algorithm. The first image taken for each of these experiments was an image of the bare glass fiber. Imaging the fiber before introducing the silicone oil to the fiber gives the measurement of the fiber radius r as a function of position z. A polynomial is fit to the fiber radius, and by taking the derivative as a function of position gives the gradient of radius of the fiber dr/dz.

The same edge detection can be done with the edge of the silicone oil, and by subtracting off the fiber thickness, we can extract the thickness of the film and droplet height, h, for each image as a function of position. An example of a profile is shown in figure 2.7c). Droplets appear as bulges in these profiles and the position of the droplet can be found using the local maxima. Fitting a small section of the bulge to a parabola, the values from the fit give the location of the drop to sub-pixel precision. Doing this for each of the frames gives the position of the droplets as a function of time. To smooth the data, a moving spline is fit over the position data, and which is used to take the numerical derivative, giving the velocity of the droplets. From the droplet position, heights, film thicknesses, velocities and fiber radius and gradient in radius we can extract all of the important information for these experiments.

In Chapter 6, additional image processing techniques needed to be implemented in addition to edge detection. The vertical speed of the chain was found using a cross-correlation technique. First, the images were binarized, so the bubbles were distinct from the background, and the center trace of the bubble chain was found. The vertical speed of the chain was calculated using the center traces by comparing one trace to the next frame. Using cross-correlation, the distance traveled in pixels could be extracted. Cross-correlation (`correlate` from `scipy.signal` [121]) is a spatially resolved measure of similarity between two profiles. One profile is translated across the other at a given step interval and the similarity between the two profiles is calculated. The position or ‘lag’ that shows the most similar profile

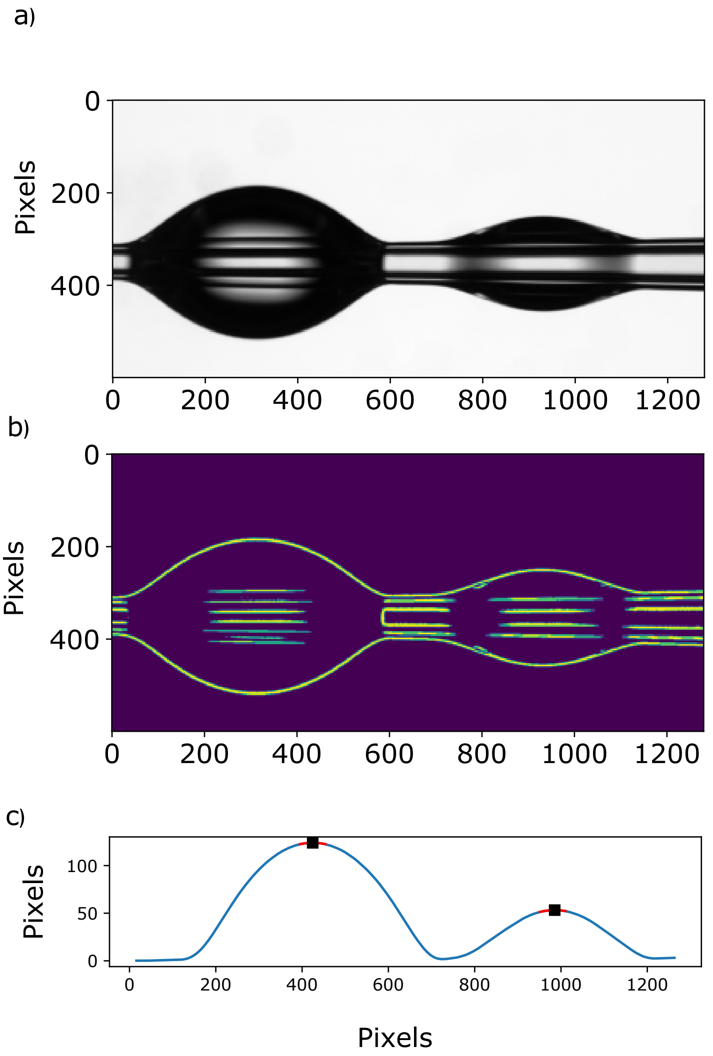

Figure 2.7: The image processing pipeline for a sample optical microscopy image of oil droplets on a conical fiber. a) The raw image of two oil droplets on a conical fiber. b) The image after edge detection has been performed. Light colours indicate edges, where the dark indicates non-edges. c) The profile of the oil surface after subtracting the radius of the fiber. The location of the center of each droplet is marked with a black square, which has been found by fitting a parabola (red) to the local maximum of the droplet.

is noted by a peak in the cross-correlation function [122]. The distance that the profiles need to shift to reach a maximum similarity corresponds to the distance that the chain has traveled in one frame. The distance moved per frame was averaged for the entirety of the data set to find the vertical velocity of the chain.

The bubble radius R was found using template matching. Template matching is an image analysis technique that searches an image for a smaller image patch. For example, figure 2.8a) shows a sample image of a chain of bubbles, and the inset i) shows the image patch that will be used as the template. Using a python package called `match_template` from `scikit-image` [123] which performs a 2-dimensional cross-correlation to match the location of the template across the image. This package exports an intensity map that corresponds to the location where the template image is present on the original image. Figure 2.8b) shows the cross-correlation map, where light colors indicate a higher similarity between the template and the image. Then peak finding functions can be used to locate instances of the template image. In this example, locations of the bubble template are indicated with a green dot in figure 2.8c). For this project, we can use the location of the bubbles to calculate the radius of the bubbles. Starting at the bottom of the frame where the bubbles are produced, bubbles are matched along the chain from the right and left side of the reflected images and using trigonometry for the two imaged planes, we calculate the distance between the center of subsequent bubbles. This distance corresponds to the diameter of the bubbles.

Finally, the amplitude of the buckling is determined by averaging all of the images for a given video. Averaging the images blur the compound image as a function of time, as shown in figure 2.9a), and by taking a horizontal cross section of the intensity allows us to find the outer edge of the bubble chain. Figure 2.9b) shows the profile of the blurred image along the horizontal line shown in figure 2.9a), with the beginning and end of the profile indicating the amplitude. Subtracting off the bubble radius and reconstructing the averaged data in 3-dimensions gives the average buckling amplitude.

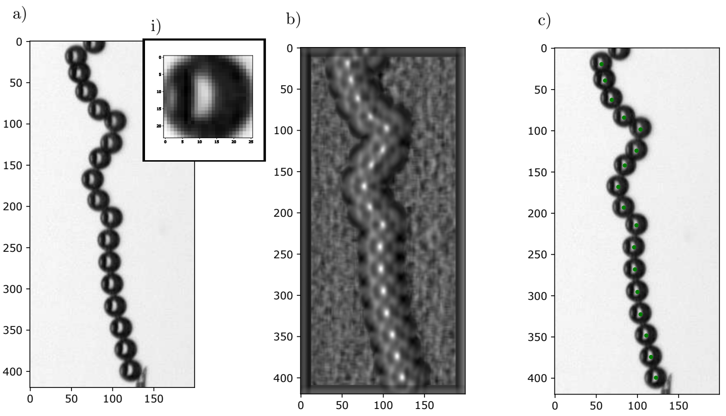

FIGURE 2.8: The image processing pipeline using template matching. a) A sample image of a number of air bubbles linked together in a chain and the inset i) shows the template bubble used in template matching. b) The intensity profile corresponding to instances of the template image in the original image. c) The sample image overlaid with green dots to indicate the located instances of the template bubble image.

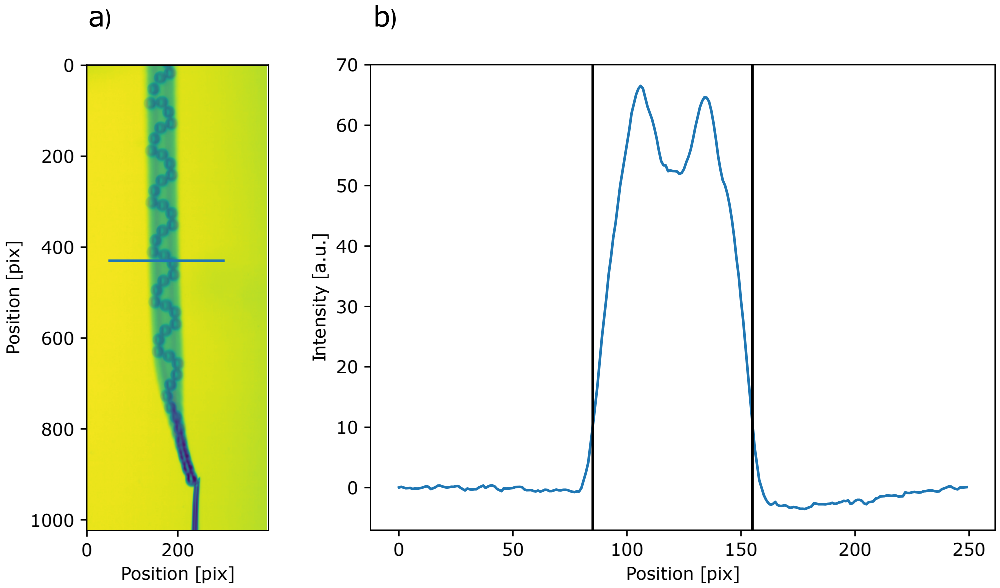

FIGURE 2.9: The image analysis pipeline to calculate the buckling amplitude of a bubble chain. a) A sample image from the data set is overlaid with an averaged image of all the images in the data set. It creates a blurred outline that is sliced horizontally. A sample slice is shown with a blue horizontal line. b) The intensity profile indicated by the horizontal location in panel a). The beginning and end of the amplitude are indicated by black lines.

Chapter 3

Droplet migration on conical fibers

Clementine Fournier, Carmen L. Lee, Rafael D. Schulman, Élie Raphaël and Kari Dalnoki-Veress

European Physical Journal E 44:12, 2021.

3.1 Paper introduction

This paper was motivated by the transport of liquids along slender structures in nature, specifically the motion of droplets on conical fibers. For example, droplets of water condense on cactus spines before spontaneously moving toward the base of the fiber. In this study, we have considered the interplay between surface tension which drives spontaneous motion of the droplet, and viscous dissipation which resists motion. An ideal cactus spine is modelled using glass pipettes that smoothly taper from a thin tip to a wider base with a gradually increasing radius gradient. The droplets are made of silicone oils of different viscosities. The oil totally wets the glass substrate, and the droplet moves toward the base of the fiber to maximize the contact of the liquid with the fiber.

Although droplet motion on conical fibers has been well studied, most previous works focus on systems with large droplets and large fibers, and with Bond numbers approaching 1 [85, 124, 125, 126]. In this paper, we chose to study small length scales so that the droplets will be axisymmetric around the fiber. We refined a simple model that considers the force due to surface tension at the two contact lines between the droplet and the fiber. We considered viscous dissipation in the droplet and use an approximation to model the shear force over the solid-liquid boundary. Balancing viscous and capillary forces, we found good agreement between the predicted speed of the droplet and the experimentally measured values. In addition, this is the first time to our knowledge that the relationship between drop height and fiber radius, as derived by Carroll in 1976 [78], has been verified experimentally.

Clementine Fournier, Rafael Schulman and Kari Dalnoki-Veress conceptualized the experiments. Clementine Fournier performed the data collection and wrote the MATLAB code for image analysis. I finalized the theoretical model that was initially developed by Rafael Schulman, Clementine Fournier, Élie Raphaël and Kari Dalnoki-Veress. I re-analyzed the data, and produced the figures containing the experimental data, along with editing subsequent versions of the manuscript.

The European Physical Journal volume 44 · number 2 · february · 2021

EPJ E

FOUNDED BY PIERRE-GILLES DE GENNES

Recognized by European Physical Society

Soft Matter and Biological Physics

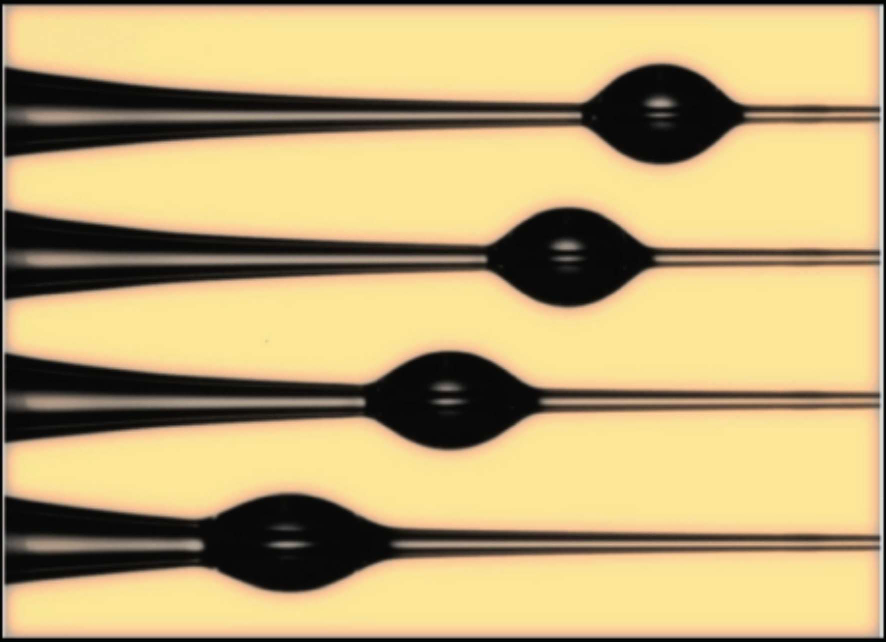

Droplet migration is driven by the changing curvature along a conical fiber.
Image courtesy of Clementine Fournier

Science Press | edp sciences
Società Italiana di Fisica
Springer

Eur. Phys. J. E (2021) 44:12
https://doi.org/10.1140/epje/s10189-021-00014-z

THE EUROPEAN
PHYSICAL JOURNAL E

Regular Article - Flowing Matter

Droplet migration on conical fibers

Clementine Fournier[1], Carmen L. Lee[1], Rafael D. Schulman[1], Élie Raphaël[2], and
Kari Dalnoki-Veress[1,2,a]

[1] Department of Physics and Astronomy, McMaster University, Hamilton, ON L8S 4M1, Canada
[2] UMR CNRS Gulliver 7083, ESPCI Paris, PSL Research University, 75005 Paris, France

Received 20 August 2020 / Accepted 5 January 2021 / Published online 8 March 2021
© The Author(s), under exclusive licence to EDP Sciences, SIF and Springer-Verlag GmbH Germany,
part of Springer Nature 2021

Abstract The spontaneous migration of droplets on conical fibers is studied experimentally by depositing silicone oil droplets onto conical glass fibers. Their motion is recorded using optical microscopy and analyzed to extract the relevant geometrical parameters of the system. The speed of the droplet can be predicted as a function of geometry and the fluid properties using a simple theoretical model, which balances viscous dissipation against the surface tension driving force. The experimental data are found to be in good agreement with the model.

1 Introduction

Spontaneous water transport systems at small length scales are a crucial feature for the survival of many living organisms and have been widely studied. In some cases, the aim is to remove excess water. For instance, water strider legs [1] and bird feathers [2] have water repelling properties. However, many of the organisms employing water transport do so to collect water. Spider webs [3], the backs of desert beetles [4], desert moss structures [5] and cacti spines [6–9] help these plants and animals collect the water necessary for their survival. In the case of cacti, water collection is based on a simple mechanism: when fog condenses at the tip of a conical cactus spine, a droplet forms that spontaneously migrates towards the widest end of the spine under the action of surface tension as a driving force. Many recent artificial water harvesting systems have been inspired by this mechanism [10–16], with the intent of fighting drought in arid environments. However, there are still unanswered questions about the droplet dynamics in this system.

A standard framework to describe droplets on cylindrical fibers has been developed by Caroll [17,18], who also highlighted the existence and the transition between two possible equilibrium configurations for a droplet on a fiber: the *asymmetric clam shell* configuration, in which the droplet is in contact with one side of the fiber, and the *axisymmetric barrel configuration*, in which the droplet envelopes the fiber. Drop transport along fibers may be induced by several means; previous works have used gradients in coating [19], temperature gradients [20,21] and gravity [22–25] to control the motion of droplets on cylindrical fibers. Lorenceau and Quéré [26] were the first to propose a theoretical model, based on Carroll's framework, to explain barrel shaped droplet dynamics on conical fibers. They showed that a gradient in Laplace pressure along the fiber will drive the motion of the droplet: the thicker the fiber is, the smaller the Laplace pressure will be, thus creating a spontaneous migration of the droplet toward thicker regions of the fiber. Their work is focused on large drop and fiber systems (characteristic length scale of approximately 1 mm), at which gravity must be taken into account and for a small range of relative drop sizes, *i.e.,* the drop size is compared to the fiber radius. The experimental results from Lorenceau and Quéré focus on the case where the drop size is comparable to the fiber radius, and therefore, the drop is quasi-cylindrical, along with considering the theoretical explanation for when the drop is quasi-spherical. Other recent theoretical, simulation and experimental works on this topic [16,27–32] have focused on large length scales and, in some of these studies, investigated where gravity fully balances the surface tension driving force. Smaller length scales have been explored in a more recent study, where the data were analyzed with the model presented by Lorenceau and Quéré [33]. In contrast to the model presented by Lorenceau and Quéré, others have modeled the driving force being due to surface tension acting on the point of contact between the fiber and droplet [16,31]. Moreover, the migration of clam shell drops has also been investigated [34,35]. In addition, the spontaneous migration of drops inside a conical tube or a wedge has been studied recently and theoretical models were proposed to describe this case [28,36–41]. Even if the geometry differs, the same forces are at play: gravity and gradients in the Laplace pressure. More generally, the asymmetry created by cone-like structures has been an inspiration in the field,

---

[a] e-mail: dalnoki@mcmaster.ca (corresponding author)

for instance, in elastocapillarity, where a liquid drop between two elastic fibers or thin sheets can make them coalesce or separate [42–46].

In the present work, we study the migration of highly viscous, totally wetting, and thus barrel-shaped, droplets on conical glass fibers on length scales at which gravity can be neglected. We explore a large range of drop sizes relative to the fiber radius. In this droplet/conical fiber system, the only forces acting on the droplet are a driving force originating from surface tension and the viscous shear force. The model we present is equivalent to that of Lorenceau and Quéré, with a modification to the assumptions used to describe the geometry of the drop. The simple theoretical model well predicts the droplet speed as a function of the radius, the gradient of the radius, droplet volume, as well as the surface tension and viscosity of the fluid.

2 Experimental methods

The glass fibers were prepared by pulling standard borosilicate glass capillary tubes with an outer diameter of 1 mm in a magnetic micropipette puller (Narishige PN-30). The resulting shape of the transformed pipette was a nearly conical fiber with a changing gradient and tip size of tens of micrometers. We note that though the fibers are "trumpet" shaped, with a gradient in diameter that increases weakly as the diameter increases, on the length scale of the droplets they are conical. The variations in diameter and gradient were unique to each pipette. Glass was chosen because it presents a well-controlled and smooth surface. Three different silicone oils, i.e., poly(dimethyl siloxane) (PDMS), were used: vinyl terminated PDMS, silanol terminated PDMS and vinyl terminated copolymer (0.3–0.4% vinylmethylsiloxane)-dimethylsiloxane (Gelest). The respective kinematic viscosities are 5000 cSt, 2000 cSt and 1000 cSt and a surface tension of $\gamma = 22$ mN/m. Silicone oils were the most appropriate liquids in this case, as they have well-controlled viscosities, are non-volatile and chemically stable. These oils also totally wet glass which means that droplets have a zero equilibrium contact angle with the fibers.

A glass fiber is cleaned using acetone and methanol to remove any dust particles. It is then fixed in a horizontal orientation, and a small droplet of PDMS is placed close to the tip of the fiber as shown in Fig. 1a at $t = 0$ s. The droplet is first produced using another micropipette, which then deposits it on to the fiber by brushing the droplet perpendicularly on the top of the fiber. Once the droplet is deposited, its motion is recorded from above using an optical microscope. Snapshots of the resulting time series of the motion are shown in Fig. 1a. An average frame rate of 1 image per second is used. The recording continues until either the droplet exits the field of view or it loses its barrel shape and axial symmetry, which happens when the fiber radius becomes large compared to the droplet size. The first two droplets migrating on an as-cleaned fiber coat the fiber with a thin film of PDMS. Here we focus mainly on subsequent droplets, as we wish to study droplet motion on fibers which are pre-wet by a homogenous thin liquid film. Subsequently, the migration of several droplets of different volumes is recorded and analyzed.

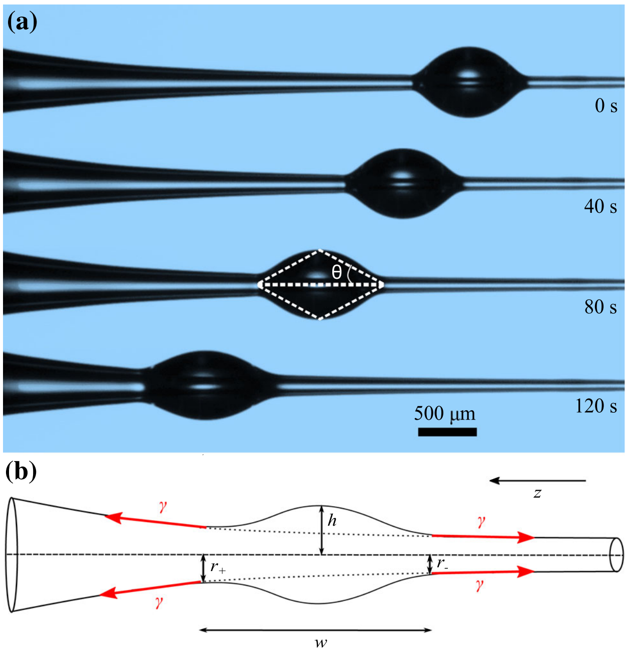

Fig. 1 **a** Microscope images of droplet migrating along a conical fiber at different times. The third panel is annotated with the wedges defined in the model (see Sect. 3). **b** Schematic of a barrel-shaped droplet on a pre-wetted conical fiber with the relevant lengths identified. The surface tension γ acting as a driving force on the droplet is also shown

To ensure that gravity had no impact on the measurements, the experimental setup (including the conical fiber and the microscope) was tilted at an angle and the experiment was reproduced in this configuration. The resulting data presented no difference with the rest of the recorded data; thus, gravitational effects are overwhelmed by surface tension-driven forces. The dominance of surface tension over gravity in the experiments presented is to be expected since the capillary length of the silicone oils used is $l_c = \sqrt{\gamma/(\rho g)} \sim 1.5$ mm, with density $\rho \approx 965$ kg/m^3 and g the acceleration due to gravity.

Several parameters of interest are extracted from the videos: the fiber radius r, the radius gradient $\mathrm{d}r/\mathrm{d}z$ as a function of the axial coordinate z, as well as the droplet properties, height h, volume Ω, width w and position at all times. Some of these parameters are denoted in Fig. 1b. All parameters are obtained by direct image analysis. The droplet position is retrieved by averaging the z-position of the maximum and minimum of parabolas fitted, respectively, to the top and bottom of the detected edge of the droplet. The speed v is calculated as the numerical time derivative of the droplet position.

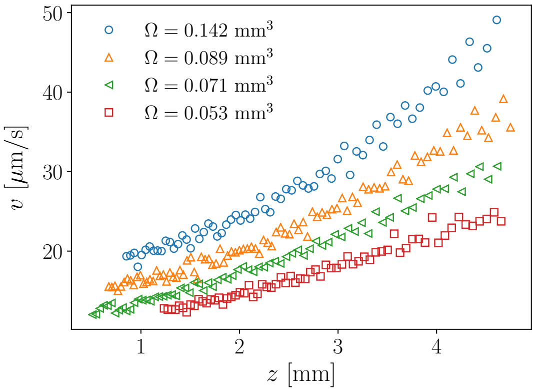

Fig. 2 Speed v of several droplets migrating one after another along the same conical fiber plotted as a function of their position on the fiber z. Different markers represent droplets of different volumes Ω

As the goal of this study is to find a comprehensive expression for v as a function of all the other variables, a first step is to look at how the speed varies with the other parameters of the system. A plot of v as a function of the droplet position (Fig. 2) shows the speed of four droplets of different volumes that migrated on the same pipette. From this plot, it is evident that the speed increases with position. However, we also know that both the radius and the gradient of the fiber increase with position. Therefore, the raw data do not allow us to dissociate the effect of each parameter. A second observation is that the speed increases with the droplet volume. Since there are several variables which influence the droplet speed, it is necessary to develop a model in order to attain a comprehensive expression for v as a function of all the relevant parameters of the system.

3 Theoretical model

In order to develop a model, we consider all the forces applied on the droplet. Gravity is negligible, verified both by the experiment (see Sect. 2) and the fact that the length scale of the experiments is well below the capillary length. We assume that inertial forces are negligible, as the Reynolds number is on the order of 10^{-6}. Two main contributions remain: the driving force caused by the surface tension γ of the silicone oil, as depicted in Fig. 1b, and the viscous dissipation in the liquid. The first contribution, which we denote F_γ, is the net surface tension force exerted by liquid–air interface of the pre-wetted fiber onto the droplet volume. It is composed of a difference between two surface tension forces: one acting at the extremity of the advancing side where $r = r_+$ and another acting at the receding side where $r = r_-$. We note that here we consider the external forces acting on the droplet (surface tension at the contact lines), rather than the method of internal Laplace pressure gradients as implemented by Lorenceau and Quéré [26]. A simple approximation gives the following final expression for F_γ:

$$F_\gamma \sim 2\pi\gamma r_+ - 2\pi\gamma r_- \sim \gamma w \frac{\mathrm{d}r}{\mathrm{d}z}. \quad (1)$$

We note that this simple approximation ignores the difference in the advancing and receding contact angles [16]. The second contribution, denoted F_η, results from the viscous force at the solid–liquid interface. In order to attain a simple expression for this quantity, we approximate the droplet shape as two joined wedges drawn in the third panel of Fig. 1a which depend on h and w. Although a crude approximation, it should suffice for quantifying the dissipation at the level of scaling; furthermore, this approximation is consistent with the use of h to describe the dynamics of the Plateau–Rayleigh instability [47]. In this case, the viscous force can be evaluated by integrating the shear force over the entire liquid–solid area (A_{ls}) beneath the wedge [48]:

$$F_\eta \sim \iint_{A_{\mathrm{ls}}} \eta \left.\frac{\mathrm{d}v}{\mathrm{d}y}\right|_{y=0} \sim \frac{\eta r v}{\tan(\theta)}\,, \quad (2)$$

where y represents the radial coordinate, which is equal to 0 when the point of interest is at the center of the fiber, η is the dynamic viscosity and θ is angle of the wedges which approximate the droplet. Here, we have neglected any prefactors and the logarithmic term which truncates the integral in viscous wedge dissipation (see Ref. [48]). The only parameter from this expression that has not directly been measured in the experiment is $\tan(\theta)$. Using simple trigonometry, we have:

$$\tan(\theta) = \frac{h}{w/2}\,. \quad (3)$$

Substituting Eq. 3 back into Eq. 2, a final expression for F_η is obtained:

$$F_\eta \sim \frac{\eta r v w}{h}\,. \quad (4)$$

In the absence of gravity and inertia, we must have $F_\eta \sim F_\gamma$. Thus, equating Eqs. 1 and 4 yields an expression for the speed as a function of all the other relevant parameters:

$$v \sim \frac{\gamma}{\eta}\frac{h}{r}\frac{\mathrm{d}r}{\mathrm{d}z}. \quad (5)$$

The droplet height can in principle be obtained from an exact equation of the shape of a droplet on a fiber, assuming the quasi-static approximation. For a barrel droplet on a cylindrical fiber, it has been shown that there is a non-trivial dependence on the fiber radius [17,18,49,50]. The relationship between h and r as derived by Carroll [17,18] is shown as a solid black line in Fig. 3 with reduced coordinates $h/\Omega^{1/3}$ and $r/\Omega^{1/3}$ and is non-monotonic. The dashed black line shown in the inset of Fig. 3 represents the asymptotic regime in which $h = r$. For large r, h tends

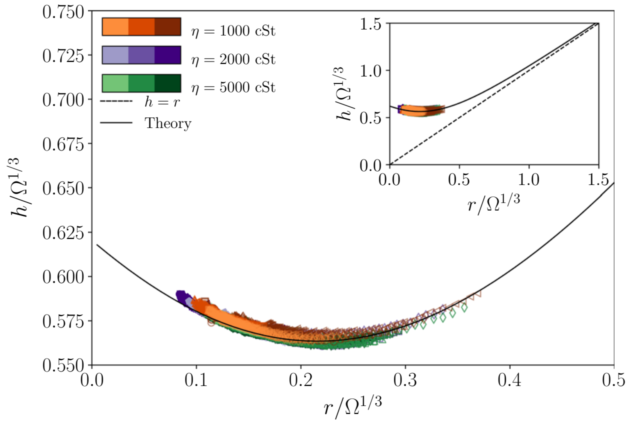

Fig. 3 Reduced height $h/\Omega^{1/3}$ of all studied droplets plotted as a function of the reduced radii of the fibers $r/\Omega^{1/3}$, on which the droplets are migrating. The markers show the experimental data for all droplets. Different colors for the markers represent viscosities: 1000 cSt (orange), 2000 cSt (purple) and 5000 cSt (green); different shades of a color correspond to different fibers. The solid black line represents the theoretical relationship between $h/\Omega^{1/3}$ and $r/\Omega^{1/3}$, as derived by Carroll [17,18] with no fitting parameters. The inset in the image shows the experimental data, the theoretical relationship and the dashed black line of equation $h = r$ show that the predicted h tends towards r for large fiber radii on a larger scale compared to the main figure

towards r as the droplet flattens and takes the shape of a cylinder enveloping the fiber. For small r, h is close to that of a droplet in a quasi-spherical regime, where $h/\Omega^{1/3} \approx 0.62$ as $r \to 0$ (a droplet can be approximated as a sphere of radius h). Experimentally the parameters in Eq. 5 can all be determined easily. η and γ are known fluid properties, and r and $\frac{\mathrm{d}r}{\mathrm{d}z}$ are geometrical properties of the fiber which can be determined from image analysis as discussed above (see Sect. 2). Lastly, since the droplet height varies non-trivially with fiber radius, we determine h experimentally at every image frame in the sequence.

4 Results and discussions

We first turn to the height of the droplet on a fiber. Since the droplet migrates, if we make the quasi-static assumption (i.e., neglect fiber gradient and assume $v = 0$), the experiment is equivalent to extracting the height of a droplet as a function of fiber radius. The experimental data are shown in Fig. 3, with markers corresponding to the three different viscosities: 1000 cSt (orange), 2000 cSt (purple) and 5000 cSt (green); different shades correspond to different conical fibers. To the best of our knowledge, this relationship has not been experimentally verified and the agreement with the classic theory is excellent with no fitting parameters. Although for small fiber radii h is close to that of a droplet in a quasi-spherical regime, we do not make the common approximation of $h \sim \Omega^{1/3}$ in this study.

The droplet speed as a function of experimentally relevant parameters is given by the model prediction presented in Eq. 5. In Fig. 4a, we plot the speed, v, as a function of $\frac{h}{r}\frac{\mathrm{d}r}{\mathrm{d}z}$. The model predicts a straight line through the origin with a slope proportional to $\frac{\gamma}{\eta}$. Indeed, for all the experiments (52 in total), the experimental data are in excellent agreement with the simple model despite the approximations made (see [16] for a more rigorous theory and simulation). The droplets follow three different trends corresponding to the three different viscosities: 1000 cSt (orange markers), 2000 cSt (purple markers) and 5000 cSt (green markers). For each viscosity, three different fibers of varying radii and gradients were used to diversify the experimental conditions. They correspond to different colors shades of the markers. On each single fiber, several droplets migrations (6 on average) were recorded once the fiber was pre-wet. In Fig. 4a, each different type of marker (circle, square, etc.) corresponds to a different droplet. According to Eq. 5, these straight lines have slopes that are inversely proportional to the respective viscosities of the fluids but otherwise have the same prefactor. The prefactor itself is the result of the multiplication of the surface tension γ (the same for the three oils that were used) and a numerical coefficient of order of 10^{-1}.

The comparison between model and data can be tested further by dividing the speed by the capillary velocity of the oil γ/η, which normalizes the data by the corresponding viscosities. The expectation is then to obtain a single trend for all droplets, in this case a straight line going through the origin with a slope equal to the prefactor discussed earlier: a numerical prefactor which we find to be equal to 0.074 ± 0.002 by fitting the data. We see in Fig. 4b that all data collapse in agreement with Eq. 5. The agreement between the data and the model further demonstrates the robustness of the model.

Limitations of the model approximations could be observed in the experiments. For instance, when the droplet continues to migrate towards the larger end of the fiber, there is a point where the droplet becomes asymmetric which results in a deviation of the data from the expected straight line when plotted as shown in Fig. 4b. Failure of the model can also be observed for droplets with extreme volumes when the volume is sufficiently large and gravity cannot be neglected. This deviation happens when the characteristic dimension of the droplet is comparable to the capillary length of the liquid.

A further interesting observation can be made about the first droplets to migrate on each fiber. In that case, the droplets are moving on fiber that has not been prewet. The resulting data for these droplets are still found to collapse onto a straight line going through the origin when plotted as shown in the inset in Fig. 4b. The only difference is that the slope of this line is smaller than the slope of the wet fiber data by a factor of approximately 4. The altered dynamics is reasonable

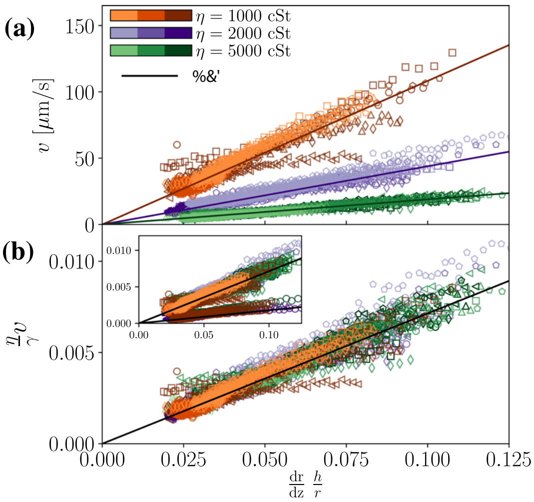

Fig. 4 **a** Speed for all studied droplets as a function of the gradient of their respective fibers multiplied by their height and divided by their radii, $\frac{\mathrm{d}r}{\mathrm{d}z}\frac{h}{r}$. Different color families represent the viscosity of the PDMS: 1000 cSt (orange markers), 2000 cSt (purple markers) and 5000 cSt (green markers). Different color shades denote different fibers (3 different fibers for each viscosity). Different types of markers (circle, square, etc.) denote different droplets. The lines represent the best fit of the model (Eq. 5) for each viscosity. The best fit lines have slopes of $a\gamma/\eta$, where a was found to be $\sim 0.074 \pm 0.002$. **b** Speed normalized by the capillary velocity for all studied droplets as a function of $\frac{\mathrm{d}r}{\mathrm{d}z}\frac{h}{r}$. The color scheme is the same as in **a**. The straight line represents the best fit of the model to all data with the best fit slope of $\sim 0.074 \pm 0.002$. The inset includes the data from the main panel and the speed normalized by the capillary velocity for droplets on a dry fiber as a function of $\frac{\mathrm{d}r}{\mathrm{d}z}\frac{h}{r}$. The best fit slope for the data on a dry cone is $\sim 0.018 \pm 0.003$

because in the absence of a pre-wetting film there is greater viscous dissipation at the advancing contact line, and furthermore, one can expect a modification to the driving force depicted in Fig. 1b. Images of such droplets in motion reveal a cusp at the contact line and an advancing angle that deviates significantly from the receding angle, unlike the case of droplets moving on a pre-wet fiber. Regardless, the deviation results in a constant pre-factor so that the overall scaling remains unchanged.

The work presented here differs from the experiments presented by Lorenceau and Quéré [26] and the work by Li and Thoroddsen [33] in several ways. First, in our experiments, gravity is negligible because we consider droplets with characteristic sizes smaller than the capillary length, while Lorenceau and Quéré studied larger droplets. Second, here we focus on a broad range of relative droplet sizes in the quasi-spherical regime. In contrast, Lorenceau and Quéré focus on experimental results in the quasi-cylindrical regime. Third, our theoretical model differs from the model built by Lorenceau and Quéré and used by Li and Thoroddsen. While we also predict the droplet speed using a balance of both the viscous dissipation and the driving force, we use a different approximation for the dissipation and define our driving force through the tensions at the contact line. Lastly, in previous works by Lorenceau and Quéré as well as Li and Thoroddsen, experimental data are provided as evidence for the models. Just as for the model presented here, the authors predict a direct proportionality between the speed as a function of fiber gradient with a speed that vanishes as the gradient tends to zero. In both studies [26,33] when comparing data to the theory, the data are consistent with a linear dependence of speed on the fiber gradient, but inconsistent with the prediction that the speed must vanish when the gradient vanishes (i.e., the best fit lines do not go through the origin and predict a nonzero velocity when there is no gradient). We have resolved this inconsistency with our model and data.

5 Conclusions

In this work, the spontaneous migration of a droplet on a fiber with a radius gradient has been characterized. If gravity and inertia are negligible, the speed of the droplet can be predicted as a function of the other parameters of the system. These parameters are geometrical (radius and gradient of the fiber, droplet height) and fluid characteristics (viscosity, surface tension). The predicted speed of droplet migration is based on a simple theoretical model in which the viscous shear force on the droplet balances the surface tension driving force. We find a good agreement between this model and the experiments that were performed using various fiber shapes and droplet volumes. We further validate the non-monotonic dependence of droplet height on fiber radius. One could imagine using the model as a way to improve future fog harvesting devices inspired by this spontaneous droplet migration mechanism often seen in biological systems.

Acknowledgements The authors are grateful to Michael Brook and Dan Chen for providing the silicone oils, and to Tak Shing Chan and Andreas Carlson for extensive discussions. The financial support by the Natural Science and Engineering Research Council of Canada is gratefully acknowledged.

Author contribution statement

CF, RDS and KDV designed the research project, CF performed all experiments, all authors contributed to analyzing the data and developing the models, and CF wrote the first draft of the manuscript. All authors edited the manuscript to generate a final version and contributed to discussions.

Data Availability Statement This manuscript has associated data in a data repository. [Authors' comment: Please contact the corresponding author for data.]

References

1. Q. Wang, X. Yao, H. Liu, D. Quéré, L. Jiang, Proc. Natl. Acad. Sci. USA **112**, 9247 (2015)
2. C. Duprat, S. Protiere, A. Beebe, H. Stone, Nature **482**, 510 (2012)
3. Y. Zheng, H. Bai, Z. Huang, X. Tian, F.Q. Nie, Y. Zhao, J. Zhai, L. Jiang, Nature **463**, 640 (2010)
4. A.R. Parker, C.R. Lawrence, Nature **414**, 33 (2001)
5. Z. Pan, W.G. Pitt, Y. Zhang, N. Wu, Y. Tao, T.T. Truscott, Nat. Plants **2**, 16076 (2016)
6. J. Ju, H. Bai, Y. Zheng, T. Zhao, R. Fang, L. Jiang, Nat. Commun. **3**, 1247 (2012)
7. L. Guo, G. Tang, Int. J. Heat Mass Transf. **84**, 198 (2015)
8. C. Luo, Langmuir **31**, 11809 (2015)
9. F.T. Malik, R.M. Clement, D.T. Gethin, D. Beysens, R.E. Cohen, W. Krawszik, A.R. Parker, Bioinspir. Biomim. **10**, 036005 (2015)
10. K. Li, J. Ju, Z. Xue, J. Ma, L. Feng, S. Gao, L. Jiang, Nat. Commun. **4**, 2276 (2013)
11. J. Ju, K. Xiao, X. Yao, H. Bai, L. Jiang, Adv. Mater. **25**, 5937 (2013)
12. X. Heng, M. Xiang, Z. Lu, C. Luo, A.C.S. Appl, Mater. Interfaces **6**, 8032 (2014)
13. Y. Peng, Y. He, S. Yang, S. Ben, M. Cao, K. Li, K. Liu, L. Jiang, Adv. Funct. Mater. **25**, 5967 (2015)
14. M. Cao, J. Ju, K. Li, S. Dou, K. Liu, L. Jiang, Adv. Funct. Mater. **24**, 3235 (2014)
15. T. Xu, Y. Lin, M. Zhang, W. Shi, Y. Zheng, ACS Nano **10**, 10681 (2016)
16. T.S. Chan, F. Yang, A. Carlson, J. Fluid Mech. **894**, A26 (2020)
17. B. Carroll, J. Colloid Interface Sci. **57**, 488 (1976)
18. B. Carroll, Langmuir **2**, 248 (1986)
19. H. Bai, X. Tian, Y. Zheng, J. Ju, Y. Zhao, L. Jiang, Adv. Mater. **22**, 5521 (2010)
20. Y. Hou, L. Gao, S. Feng, Y. Chen, Y. Xue, L. Jiang, Y. Zheng, Chem. Commun. **49**, 5253 (2013)
21. A.L. Yarin, W. Liu, D.H. Reneker, J. Appl. Phys. **91**, 4751 (2002)
22. Y. Chen, L. Wang, Y. Xue, L. Jiang, Y. Zheng, Sci. Rep. **3**, 2927 (2013)
23. T. Gilet, D. Terwagne, N. Vandewalle, Appl. Phys. Lett. **95**, 014106 (2009)
24. T. Gilet, D. Terwagne, N. Vandewalle, Eur. Phys. J. E. **31**, 253 (2010)
25. I.L. Kliakhandler, S.H. Davis, S.G. Bankoff, J. Fluid Mech. **429**, 381 (2001)
26. É. Lorenceau, D. Quéré, J. Fluid Mech. **510**, 29 (2004)
27. S. Michielsen, J. Zhang, J. Du, H.J. Lee, Langmuir **27**, 11867 (2011)
28. J.L. Liu, R. Xia, B.W. Li, X.Q. Feng, Chin. Phys. Lett. **24**, 3210 (2007)
29. Y.E. Liang, H.K. Tsao, Y.J. Sheng, Langmuir **31**, 1704 (2015)
30. X. Tan, T. Shi, Z. Tang, B. Sun, L. Du, Z. Peng, G. Liao, J. Bionic Eng. **13**, 364 (2016)
31. M.E.R. Shanahan, Langmuir **27**, 14919 (2011)
32. T.S. Chan, C. Pedersen, J. Koplik, A. Carlson, preprint (https://arxiv.org/abs/2008.03058)
33. E.Q. Li, S.T. Thoroddsen, Phys. Fluids **25**, 052105 (2013)
34. C. Lv, C. Chen, Y.C. Chuang, F.G. Tseng, Y. Yin, F. Grey, Q. Zheng, Phys. Rev. Lett. **113**, 026101 (2014)
35. J. McCarthy, D. Vella, A.A. Castrejón-Pita, Soft Matter **15**, 9997 (2019)
36. M. Reyssat, L. Courbin, E. Reyssat, H.A. Stone, J. Fluid Mech. **615**, 335 (2008)
37. P. Renvoisé, J. Bush, M. Prakash, D. Quéré, Europhys. Lett. **86**, 64003 (2009)
38. J.W. Bush, F. Peaudecerf, M. Prakash, D. Quéré, Adv. Colloid Interface Sci. **161**, 10 (2010)
39. Z. Wang, C.C. Chang, S.J. Hong, Y.J. Sheng, H.K. Tsao, Phys. Rev. E **87**, 062401 (2013)
40. E. Reyssat, J. Fluid Mech. **748**, 641 (2014)
41. É. Ruiz-Gutiérrez, C. Semprebon, G. McHale, R. Ledesma-Aguilar, J. Fluid Mech. **842**, 26 (2018)
42. J. Bico, B. Roman, L. Moulin, A. Boudaoud, Nature **432**, 690 (2004)
43. C. Duprat, J.M. Aristoff, H.A. Stone, J. Fluid Mech. **679**, 641 (2011)
44. J.M. Aristoff, C. Duprat, H.A. Stone, Int. J. Non Linear Mech. **46**, 648 (2011)
45. M. Taroni, D. Vella, J. Fluid Mech. **712**, 273 (2012)
46. J. Bico, É. Reyssat, B. Roman, Annu. Rev. Fluid Mech. **50**, 629 (2018)
47. S. Haefner, M. Benzaquen, O. Bäumchen, T. Salez, R. Peters, J.D. McGraw, K. Jacobs, E. Raphaël, K. Dalnoki-Veress, Nat. Commun. **6**, 1 (2015)
48. P. de Gennes, F. Brochard-Wyart, D. Quéré, *Capillarity and Wetting Phenomena: Drops, Bubbles, Pearls, Waves* (Springer, New York, 2003).
49. R.J. Roe, J. Colloid Interface Sci. **50**, 70 (1975)
50. G. McHale, M. Newton, B. Carroll, Oil Gas Sci. Technol. **56**, 47 (2001)

Chapter 4

Multiple droplets on a conical fiber: formation, motion, and droplet mergers

Carmen L. Lee*, Tak Shing Chan*, Andreas Carlson, and Kari Dalnoki-Veress
*co-first authorship
Soft Matter 18, 1364-1370. (2022).

4.1 Paper introduction

Although there is a robust theoretical and experimental background to describe how single drops spontaneously travel on conical fibers, there has been very little work on multiple droplets interacting on a conical fiber [127]. This work was inspired by nature, where heavy rainfalls coat slender structures with a film of water that then breaks up into drops, like the formation of dew drops on a spider web. In this paper, we studied how a liquid coating on a conical fiber will break up into droplets and how those droplets move and interact. First, we focused on how a liquid coating breaks up on a fiber and found that the conical substrate creates non-linear patterning between droplets. Break up dynamics were studied using a uniform coating of silicone oil on a conical glass fiber. When the film was thick relative to the fiber radius, we found that small satellite droplets formed between larger droplets. As discussed in Chapter 3, droplet speed depends on the droplet size. As a result, larger drops will catch up to smaller drops and the two will merge. We were able to identify the steps that a droplet undergoes when merging, and we studied the dynamics of the merging process. Taking inspiration from droplets merging on flat substrate [128, 129], we tracked merging dynamics by extracting the height and location of the neck between the two droplets. Numerical simulations of the geometry using the lubrication approximation were performed to study the merging dynamics which match well with experiment. We also found that we could explain the motion of the droplets during merging using surface tension arguments similar to the model presented in Chapter 3.

I designed and conducted the experiments, did the data analysis and image processing using in-house python code with support from Kari Dalnoki-Veress. Tak Shing Chan led the simulation effort with help from Andreas Carlson. I wrote the first draft of the manuscript, all authors contributed to the analysis and writing.

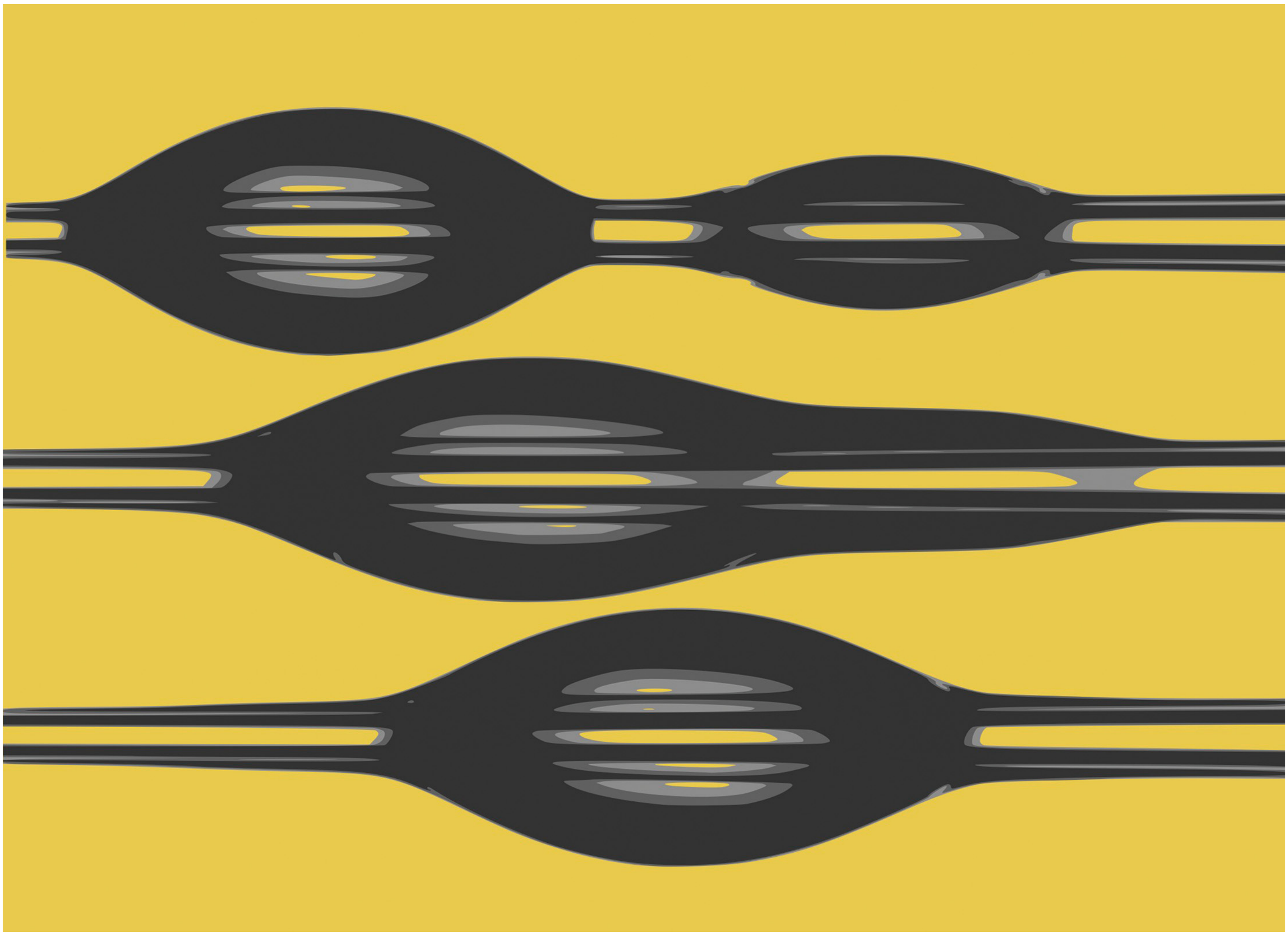

Showcasing research from Professor Kari Dalnoki-Veress's research group at McMaster University.

Multiple droplets on a conical fiber: formation, motion, and droplet mergers

Droplets placed on a conical fiber spontaneously move along a fiber. We study how multiple droplets form, move and merge using experiments and numerical simulations.

Image credit: Carmen L. Lee

As featured in:

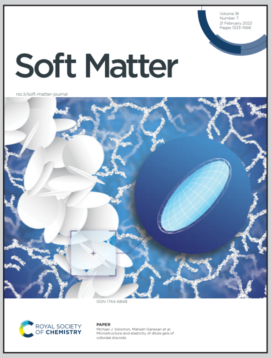

See Carmen L. Lee *et al.*,
Soft Matter, 2022, **18**, 1364.

ROYAL SOCIETY
OF **CHEMISTRY**

rsc.li/soft-matter-journal

Registered charity number: 207890

Published on 03 January 2022. Downloaded by McMaster University on 5/11/2022 3:10:19 PM.

Soft Matter

ROYAL SOCIETY OF CHEMISTRY

PAPER

View Article Online
View Journal | View Issue

Check for updates

Cite this: *Soft Matter*, 2022, **18**, 1364

Received 10th October 2021, Accepted 3rd January 2022

DOI: 10.1039/d1sm01462e

rsc.li/soft-matter-journal

Multiple droplets on a conical fiber: formation, motion, and droplet mergers†

Carmen L. Lee,‡[a] Tak Shing Chan,‡[b] Andreas Carlson [b] and Kari Dalnoki-Veress *[ac]

Small droplets on slender conical fibers spontaneously move along the fiber due to capillary action. The droplet motion depends on the geometry of the cone, the surface wettability, the surface tension, the viscosity, and the droplet size. Here we study with experiments and numerical simulations, the formation, spontaneous motion, and the eventual merger, of multiple droplets on slender conical fibers as they interact with each other. The droplet size and their spacing on the fibre is controlled by the Plateau–Rayleigh instability after dip-coating the conical fiber. Once these droplets are formed on the fiber, they spontaneously start to move. Since droplets of different size move with different speeds, they effectively coarsen the droplet patterning by merging on the fiber. The droplet merging process affects locally the droplet speed and alters the spatiotemporal film deposition on the fiber.

1 Introduction

In Nature, several species of plants[1–3] and animals[4–6] have evolved to form slender conical structures. One purpose of these conical structures is to transport liquid drops along the cone, either toward or away from the organism. For instance, the spines on a cactus can create a surface preferential to fog condensation, with droplets spontaneously travelling from the tip of the cone to the base.[7–10] The hydrophobic hairs on the legs of a water strider work to expel errant water droplets off the insect, allowing the strider to stay on the surface of the lake or pond.[11,12] Beyond these two examples, there are many more organisms and structures that exhibit this behaviour. Several studies have been conducted to examine the efficacy of droplet transport along these conical structures, and have served to motivate the development of bio-inspired fog harvesting devices.[13–16]

Droplet motion can be driven by several factors. For droplets below the capillary length, motion is driven by the surface tension of the droplet to maximize contact with the fiber when the droplet wets the fiber.[11,17–20] As the characteristic size of the droplet becomes larger than the capillary length, the droplet may either be propelled[21–24] or stalled[25] by gravity depending on the fiber orientation. Droplet motion can also be induced in these systems by temperature gradients or coatings.[26,27] The motion of a single droplet on a slender conical structure has been studied and characterized extensively, with an excellent understanding of the driving forces and viscous dissipation in the droplet.[17,19,20,23,28–31] Furthermore, previous works have examined the formation of multiple droplets *via* the Plateau–Rayleigh instability (PRI) of a film of liquid on a cylindrical fiber.[32,33] In addition, studies have examined wetting and coalescence of droplets on a fiber network with particular interest in droplet capture in textiles[34–38] However, there has been little work on the formation and interaction between multiple droplets as they traverse along a conical fiber beyond qualitative observations,[17,32,39] despite being prevalent in nature as illustrated in Fig. 1; a photograph of the *Geranium robertianum* fruit covered with dew drops.

Here we examine the formation of multiple viscous liquid droplets along a conical fiber created by the PRI. We then follow the motion of the droplets as they move along the fiber, propelled by capillary forces and the interaction between droplets when they meet and coalesce. We rationalize the experimental observations with numerical simulations of the droplet flow based on a thin film model. The experiments and simulations are found to be in excellent agreement. In this paper, we study the effect of the conical nature of these fibers and how this drives motion and merging of droplets.

2 Experimental methods

We fabricate ideal conical fibers with a smoothly changing radial gradient from borosilicate glass capillary tubes (1 mm

---

[a] *Department of Physics & Astronomy, McMaster University, Hamilton, Ontario, L8S 4M1, Canada. E-mail: dalnoki@mcmaster.ca*

[b] *Mechanics Division, Department of Mathematics, University of Oslo, 0316 Oslo, Norway*

[c] *UMR CNRS Gulliver 7083, ESPCI Paris, PSL Research University, 75005 Paris, France*

† Electronic supplementary information (ESI) available. See DOI: 10.1039/d1sm01462e

‡ These authors contributed equally to this work.

This journal is © The Royal Society of Chemistry 2022

View Article Online

Published on 03 January 2022. Downloaded by McMaster University on 5/11/2022 3:10:19 PM.

Fig. 1 Multiple dew drops covering *Geranium robertianum* fruit. Image credit: Calum Davidson, Aberdeenshire, Scotland.

outer diameter, World Precision Instruments).[19,28] The capillaries are locally heated and pulled with a constant force using a micropipette puller (Narishige PN-30). The resulting shape is a smoothly tapering conical glass fiber with the base of the fiber being the diameter of the original capillary tube (1 mm), and the tip being tens of microns in diameter.

A silicone oil (vinyl terminated polydimethylsiloxane) with kinematic viscosity η = 5000 cSt was used to create droplets in these experiments. The silicone oil is used because it is non-volatile, non-hygroscopic, and is totally-wetting on glass, with a surface tension γ = 22 mN m^{-1}. Droplets are placed on the conical fiber in two ways. The first uses the Landau–Levich–Derjaguin (LLD) film deposition,[40] where the fiber is inserted into a reservoir of fluid and then pulled away at a constant speed (ranging between 5 μm s^{-1} and 50 μm s^{-1}), leaving behind a uniform fluid film on the fiber. The thickness of the film depends on the speed that the reservoir moves, with a film thickness that increases with increasing speed. The resulting film is unstable *via* the PRI, and will break up into droplets. Fig. 2a shows a schematic diagram of this process, with relevant geometric parameters labelled. The patterning of droplet formation along the fiber is controlled by the thickness of the LLD film.

The second method begins with creating droplet in the method described in Fig. 2a on a different fiber. The resulting droplets are transferred by bringing one of the droplets into contact with the fiber.[19] This method allows for the precise placement of individual droplets along the fiber. A droplet can be placed at the tip of the fiber and allowed to completely move to the base of the fiber to deposit a thin film to act as a lubrication layer for subsequent droplets. A lubrication layer is present for all experiments to ensure the dynamics are the same between the two methods. To examine droplet coalescence, we take advantage of the dependence of droplet speed on the size of the droplet. A large droplet moves more quickly toward the base of the fiber compared to a smaller droplet.[19] We place a smaller droplet closer to the base of the fiber, and a larger droplet is placed closer to the tip allowing for the larger droplet to catch up to the smaller droplet, coalesce, and merge.

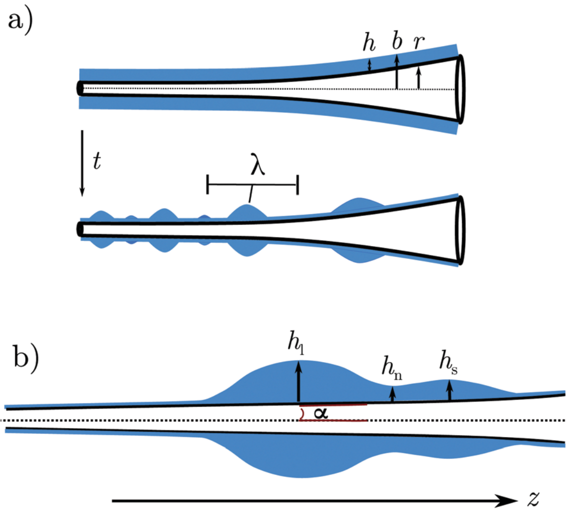

Fig. 2 (a) A schematic diagram of a coated glass fiber with radius $r(z)$ and film thickness h. After some time, t, the film breaks up into droplets *via* the Plateau–Rayleigh instability, where the thickness from the axi-symmetric centre to the liquid/air interface, b varies along the fiber. (b) A schematic of two droplets merging on a conical fiber characterised by angle α, with height h_l for the large droplet, h_s for the small droplet, and h_n for the minimum of the liquid–air interface between the droplets, as a function of horizontal position z.

With the fiber held horizontal, the droplet motion is recorded from above using an optical microscope. Additionally, a reference image of the bare glass pipette is taken before the experiment begins. From these images, the fiber radius, cone angle, and droplet heights, can be extracted as a function of position along the fiber, and as a function of time t. Image analysis was done with an in-house Python script. We use edge detection to locate the outer contour of the liquid surface $b(z)$. For each pixel position, we calculate the volume of a circular disk with radius b and height of one pixel. Summing these disks along z, we can calculate the total volume taken up by both the liquid and the cone. The same technique enables us to calculate the volume of the cone with no liquid present, which can then be used to find the volume of liquid.

3 Numerical simulations

To model the motion of the droplets, we describe the flow inside the liquid by the Stokes equations and impose a no-slip boundary condition at the solid substrate, and no-shear stress at the liquid–air interface. Assuming that both the slope of the liquid–air interface and the cone angle α are small, we apply the lubrication approximation[41,42] to the Stokes equations and obtain the thin film equation for a conical geometry. A detailed derivation of the thin film equation can be found in ref. 20. The axisymmetric liquid–air interface profile is given by $\hat{h} = \hat{h}(\zeta,t)$, defined as the distance between the interface and the substrate, as a function of the distance from the vertex of the cone ζ and time t. We note that ζ measures along the surface of the cone and is related to the experimentally measured z as $z = \zeta\cos(\alpha)$ and for small angles $\zeta \approx z$. The evolution of the liquid–air

Published on 03 January 2022. Downloaded by McMaster University on 5/11/2022 3:10:19 PM.

interface is described by the thin film equation and driven by the capillary pressure gradients $\partial p/\partial\zeta$ which reads,[20,43]

$$\frac{\partial\hat{h}}{\partial t}+\frac{1}{\zeta\alpha+\hat{h}}\frac{\partial}{\partial\zeta}\left(M\frac{\partial p}{\partial\zeta}\right)=0, \tag{1}$$

where the mobility $M = M(\hat{h},\zeta,\alpha)$ is expressed as

$$\begin{aligned}M(\hat{h},\zeta,\alpha) &= \frac{\zeta^4\alpha^4}{2\mu}\left\{\frac{1}{8}\left[3\left(1+\frac{\hat{h}}{\zeta\alpha}\right)^4\right.\right.\\ &\left.-4\left(1+\frac{\hat{h}}{\zeta\alpha}\right)^2+1\right] \\ &\left.-\frac{1}{2}\left(1+\frac{\hat{h}}{\zeta\alpha}\right)^4\ln\left(1+\frac{\hat{h}}{\zeta\alpha}\right)\right\}.\end{aligned} \tag{2}$$

The capillary pressure gradient in the liquid generates the flow and the pressure $p = p(\zeta,t)$ reads

$$p=-\gamma\left\{\frac{\dfrac{\partial^2\hat{h}}{\partial\zeta^2}}{\left[1+\left(\dfrac{\partial\hat{h}}{\partial\zeta}\right)^2\right]^{3/2}}-\frac{1-\alpha\dfrac{\partial\hat{h}}{\partial\zeta}}{(\zeta\alpha+\hat{h})\left[1+\left(\dfrac{\partial\hat{h}}{\partial\zeta}\right)^2\right]^{1/2}}\right\}, \tag{3}$$

where the expression is simplified for $\alpha \ll 1$.[20,43] Eqn (1) and (3) are discretized by linear elements and numerically solved with a Newton solver by using the open source finite element code FEniCS,[44] additional details about the numerical approach are found in.[43] The initial condition is a droplet smoothly connected to a pre-wet film of thickness ε. At the two boundaries ($\delta\Omega$) of the numerical domain we impose $\hat{h}(\delta\Omega,t) = \varepsilon$ and $p(\delta\Omega,t) = \gamma/[R(\delta\Omega) + \varepsilon]$, where $R(\delta\Omega)$ is the radius of the cone at the boundaries. We note that only the droplet volume V is important and the initial droplet shape does not affect the results.

4 Results and discussion

Before discussing the case of multiple droplet migration we first present an intuitive description of the motion of an isolated droplet which has been studied extensively.[17,19,20,23,28–31] Here we follow the essential ingredients of a model presented by Fournier *et al.*[19] aplicable to length-scales where the droplet is much smaller than the capillary length, and the effect of gravity is negligible. In short, the motion is driven by the rate of change in capillary energy, which is dissipated by the liquid viscosity. There is a difference in the capillary forces acting on the advancing and receding ends of the isolated droplet due to the difference in the circumference of the ends of the droplet: $F_\gamma = 2\pi\gamma(r_+ - r_-)$. We see that the tug-of-war between the advancing and receding ends of the droplet results in the capillary force driving the droplet towards a larger diameter on the cone. Clearly an increase in the droplet speed results from an increase in the surface tension or an increase in the cone angle α. The surface energy released is dissipated through Poiseuille flow in the viscous droplet, thus the velocity decreases with increasing viscosity. As the droplet migrates there is more contact with the no-slip boundary condition at the liquid–solid interface, thereby increasing viscous dissipation: droplets slow down as they migrate away from the apex of the cone. And lastly, a larger droplet has a greater difference in the advancing and receding contact lines resulting in a higher velocity. These relationships, though well established in the literature,[17,19,20,23,28–31] are important for providing an intuitive understanding of the results presented.

4.1 Plateau–Rayleigh instability on a conical fiber

A cylinder of liquid will break up into droplets to minimize the surface area according to the PRI. The size and spacing of the droplets increases with the initial radius of the cylinder: in the case of a liquid film with thickness h, coating a solid cylinder with radius r, the sum of the radius of the cylinder and liquid film, $b = h + r$, dictates the wavelength. However, a conical fiber does not have a constant radius along the length of the fiber, and hence the wavelength between droplets is not constant. As such, the patterning of droplets along a conical fiber will depend on the thickness of the film, and the location along the fiber. To test the effect of the film thickness, the reservoir was pulled at different constant velocities to deposit films of different thicknesses. Fig. 3 shows examples of the break up of the coating film for two different values of h: the thinner film, h = 53 μm, shown in Fig. 3a was pulled out of the reservoir more slowly than the thicker film with h = 88 μm shown in Fig. 3b. Reservoir speeds ranged from 5 μm s^{-1} to 50 μm s^{-1} to deposit appropriate Landau–Levich films for the PRI to occur in this system. For the thinner film [Fig. 3a], droplets form in panel (i) with monotonically increasing sizes along the fiber, and they

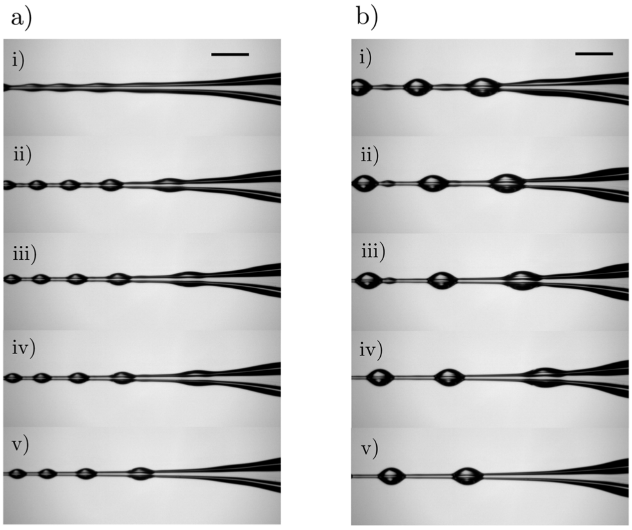

Fig. 3 Optical microscope images of a fiber with cone angle α = 0.96 ± 0.01° coated with silicone oil with film thicknesses (a) h = 53 ± 1 μm (b) h = 88 ± 1 μm. Panels (i)–(v) show snapshots of the break up of the coating film and the motion of the droplet from left to right along the fiber at 19.2, 44.8, 58.0, 73.6 and 117.8 s from the time when the fiber was coated. The film thickness in (a) shows the formation of monotonically increasing droplets, where the film thickness in (b) breaks up into principle and satellite droplets. Scale bar indicates 1000 μm.

This journal is © The Royal Society of Chemistry 2022

Published on 03 January 2022. Downloaded by McMaster University on 5/11/2022 3:10:19 PM.

move progressively toward the base of the fiber in the subsequent frames (ii)–(v). In Fig. 3b, a different patterning appears, where larger droplets form [panel (i)] with small satellite droplets in between. At later times, [panels (ii) and (iii)] the larger droplets catch up with the satellite droplets and coalesce, resulting in the large droplets moving toward the end of the fiber [panels (iv) and (v)]. Videos of this process are shown in the ESI† SI 1.

We can visualize the motion of the droplets by taking a row of pixels along the axis of the fiber for each time-step of the optical microscopy images. This row is stacked for each image in the time-series to show the migration of droplets as a function of time in Fig. 4. In Fig. 4 the same fiber is coated with four different film thicknesses ranging from $h = 29 \pm 1$ μm to $h = 88 \pm 1$ μm with the top row corresponding to the initial film at $t = 0$. The dark bands in the center panel correspond to the beginning and end of each droplet. Using these images we track the droplet locations along the fiber, denoted by the white dotted lines in the figure. At early times in the experiment as the droplets first form (indicated by the black arrow), we take these positions to calculate the wavelengths shown in Fig. 5. Above this arrow is the initial regime that is dominated by droplet formation through the Plateau–Rayleigh instability. Below this arrow, the droplets have formed and the dominant physics is associated with droplet motion and mergers. In Fig. 4c and d one can observe the principle droplets moving with a faster velocity (steeper slope) compared to the smaller satellite droplets. Once the small and large droplets come into contact, we see the trace of the smaller droplet disappear when it merges with the large droplet, this is marked with a horizontal white line overlaid on the image to guide the eye. The droplet pattern at the end of the observation time is shown in the bottom row and we note that the droplets will continue to move and migrate toward the base of the fiber, until they all collect at the base of the fiber.

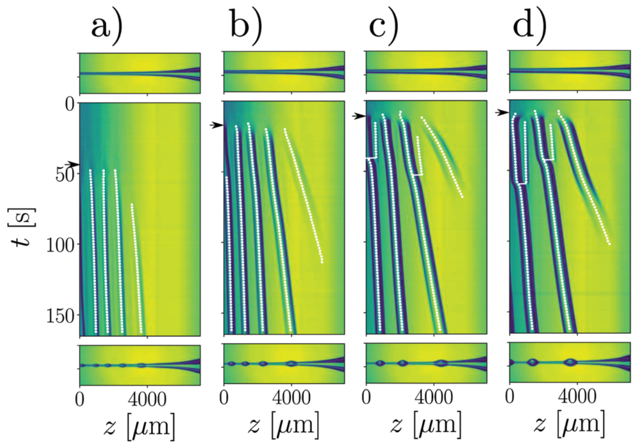

Fig. 4 Images of a fiber with cone angle $\alpha = 0.96 \pm 0.01°$ coated with silicone oil. The top row corresponds to the fiber coated with film thickness, (a) $h = 29 \pm 1$ μm, (b) 53 ± 1 μm, (c) 77 ± 1 μm, and (d) 88 ± 1 μm at the initial state $t = 0$. The middle panel shows the central slice of each image, stacked to reveal the the break up of the film into droplets and their resulting motion, giving the position z of the droplets as a function of time t. Overlaid on the images are the central position of the droplets marked with white dotted lines, and merging events are shown as horizontal white lines connecting the two merging droplets (present in (c) and (d)). Black arrows indicate the time when each experiment transitions from the PRI dominant regime to the migration/merging dominant regime. The final row shows the patterning of the droplets at the end of the observation time.

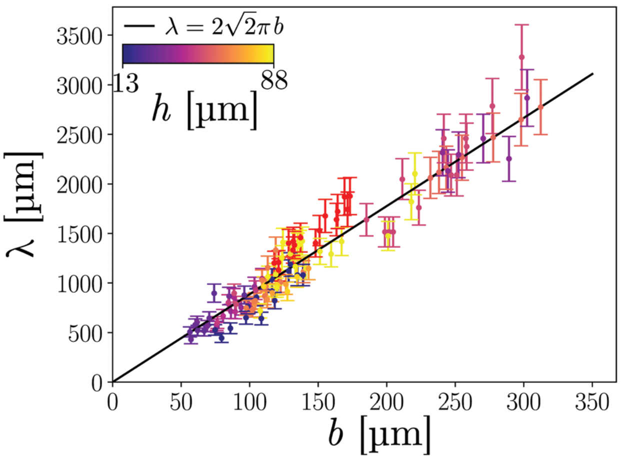

Fig. 5 Spacing between droplets (λ) produced from the Plateau–Rayleigh instability on a conical fiber. Different colours refer to different liquid film thicknesses, 8 different thicknesses are shown here for multiple fibers, while the horizontal axis, the distance from the axi-symmetric centre to the liquid/air interface, b, depends on the position along the conical fiber, z.

The relationship between wavelength of droplet formation and the radius of the fiber and coating is shown in Fig. 5. The wavelength for a given droplet is found by locating the positions of the neighbouring droplets when they form, *i.e.* where the white lines initially appear in Fig. 4. For various pipettes and film thicknesses, the initial wavelength between droplets is shown with different experiments indicated by different colours. The conical shape of the fiber results in different time constants along the length of the fiber, meaning that the droplets appear at different times and immediately move after forming, therefore the wavelength was defined when the droplet first appears with a pronounced minima on either side. To find the wavelength, we locate the position of the nearest local maxima (*i.e.* the neighbouring principle droplets) on either side of a droplet, which corresponds to twice the wavelength. The data are shown in Fig. 5. The solid line shows the relationship $\lambda = 2\pi\sqrt{2}b$, where λ is the wavelength, b is the distance from the axis of symmetry about the length of the fiber and the liquid/air interface, *i.e.* a combination of the fiber radius r with the thickness of the coating film h.[45] The wavelengths found using this method show excellent agreement with the theory and provides insight into using conical fibers to passively control the patterning of droplets.

For sufficiently large film thicknesses, the PRI occurs such that satellite droplets form between the principal droplets, which can be seen in Fig. 3b panel (i). Previous experiments and models on the motion of a single droplet on a conical fiber show droplet speed along a fiber increases with droplet volume,[17,19] due to the increased volume reducing the resistance to flow. In addition, the larger the fiber radius the slower

Published on 03 January 2022. Downloaded by McMaster University on 5/11/2022 3:10:19 PM.

the droplets move due to the increased contact with the fiber. Fournier *et al.*[19] showed the importance of the lubricating layer on the speed of the droplet: the absence of a lubricating film drastically slowed down the motion of the droplets in comparison to those droplets with a lubricating film, indicating that equivalent droplets on the same fiber move faster with a thicker precursor film compared to a thinner film. Based on these previous experiments, as the droplets move along the fiber, the larger main droplets catch up to the smaller satellite droplets that are closer to the base of the fiber. The two droplets merge to form a large droplet and change the initial distribution of drops created by the PRI.

4.2 Coalescing droplets

To examine the coalescence process in more detail, individual droplets were carefully placed on the fiber using the second droplet deposition method described in the experimental section. These droplets were imaged at higher magnification compared to the PRI droplets. Images of the merging process are shown in Fig. 6. In Fig. 6, we observe five distinct stages: (a) the two droplets begin as individual droplets. (b) As the larger droplet catches up with the smaller droplet, a thick fluid bridge forms between the two, connecting the two fluid bodies. The smaller Laplace pressure in the bridge causes the liquid in the droplets to flow toward the bridge. (c) The bridge thickens as liquid flows into the bridge and the local maximum height of the smaller droplet decreases. (d) Remnants of the small droplet leave behind a thick film preceding the larger droplet. (e) The droplet reforms into the semi-symmetric shape, and continues moving to the end of the fiber. A thicker film is deposited behind the merged droplet due to the acceleration during merging along with the higher velocity associated with the larger volume of droplet (see Fig. 6f).

In addition to optical microscopy, Fig. 6 also shows profiles of the merging process matched to the conditions of the experiment as generated by the numerical simulations. Outlined in red, the profiles shown here match exactly the profiles obtained from experiment. An interesting feature that appears in both simulation and experiment is the presence of a thicker film deposited behind the droplet after merging (shown in Fig. 6e, outlined in green). Focusing on the location outlined in green in Fig. 6e, we can extract the profile of LLD film left behind by the moving droplet, to show that the increase in speed of the droplet due to merging, deposits a thicker film than a slower moving droplet.[28] Fig. 6f shows the profile of the LLD, renormalized by the droplet volume, for each of the preceding panels of the figure.

To further understand the dynamics during droplet merging, we track the position of the droplets. We do this by locating three features on the droplets, the positions and height of two maxima associated with the large ($z_l(t)$, $h_l(t)$) and small droplet ($z_s(t)$, $h_s(t)$), and the position of an intermediate radius ($z_n(t)$, $h_n(t)$), which denotes the location of the local minima in the fluid neck (see Fig. 2b). The position along the fiber z is measured relative to the tip of the cone with a constant cone angle. Fig. 7a shows the position of these three points, normalized by the length scale determined by the volume of the large droplet V, as a function of dimensionless time $t\gamma/\eta V^{1/3}$, and Fig. 7b shows the rescaled heights $h/V^{1/3}$ of each of these points as a function of dimensionless time $t\gamma/\eta V^{1/3}$. In addition to the experimental data, we have matched the droplets with simulations. A slight difference in the experimental data compared to the simulations can be attributed to the fiber having a gently varying cone angle along the length of the fiber, unlike the simulated fiber which has a constant cone angle. Regardless, the agreement between experiment and theory is excellent.

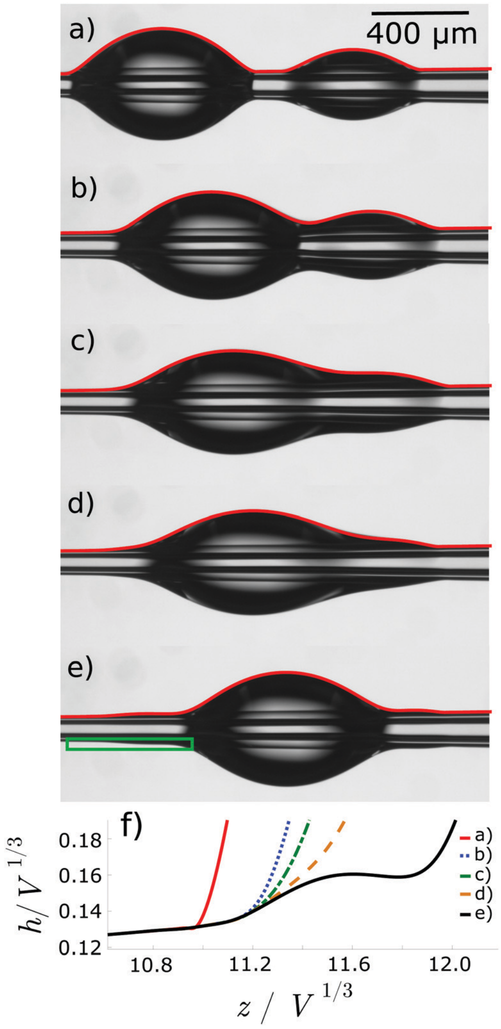

Fig. 6 Images showing the main steps in the coalescence process of two droplets (V = 0.0191 ± 0.0002 mm^3 and 0.0050 ± 0.0003 mm^3) on a conical fiber (α = 0.673 ± 0.002°). (a) Separate droplets. (b) Two droplets when first in contact with one another. (c) Flow of the smaller, higher pressure droplet backwards into the larger droplet. (d) Acceleration of the large droplet toward the film left behind by the small droplet. (e) A final droplet, the volume of the two initial droplets. Panels (a)–(e) correspond to 18.6, 47.1,47.8, 48.5, and 51.7 s after the experiment recording started. (f) The dimensionless profiles of the deposited film $h/V^{1/3}$ as a function of $z/V^{1/3}$ at different times (from (a)–(e)) in the receding region of the big droplet (indicated by the green box in (e)). A thicker film is deposited behind the droplet after the two droplets merge.

5 Conclusions

In this work, we have studied the formation of multiple droplets on a conical fiber through the breakup of a coating

This journal is © The Royal Society of Chemistry 2022

Published on 03 January 2022. Downloaded by McMaster University on 5/11/2022 3:10:19 PM.

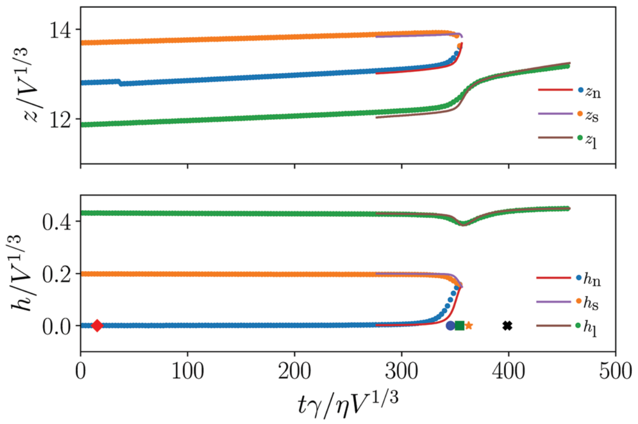

Fig. 7 (a) The position along the fiber z rescaled with the volume of the large droplet V for the maximum point of the large and small droplets along with the fluid neck as a function of dimensionless time. (b) The renormalized height of the liquid/air interface at the local maxima of the large and small droplets h_l and h_s, respectively, and the local minima between the two droplets marking the location of the liquid neck h_n are plotted as a function of time t. The heights are normalized by the length scale determined by the volume of the large droplet V. Experimental values for both subplots are denoted by dots and the matched numerical simulations are denoted by lines with cone angle α = 0.673 ± 0.002°. These data correspond to the experiment shown in Fig. 6a–e and are denoted by markers ◊, ○, □, ★, ×.

film *via* the Plateau–Rayleigh instability. The patterning of droplet production depends on the gradient of radius of the cone, where the averaged wavelength or droplet spacing depends on the radius of the fiber at the location of the drop. The initial spacing of the droplets can be explained through the relationship predicted by the classic Plateau–Rayleigh instability theory. The droplets are driven by the surface tension to spontaneously move along the fiber, where the motion of the drops depends on the size of the droplet, properties of the liquid and geometry of the fiber. In this system, the gradients in radius of the conical fiber create an imbalance in capillary forces and serve to drive motion toward the base of the fiber for a wetting liquid. The larger the droplet, the larger the imbalance as the droplet spans a larger range of fiber radii, and larger droplets move more quickly compared to smaller droplets. The motion of the droplets is limited by the viscosity of the liquid, a droplet of a more viscous fluid will move more slowly compared to a droplet of lower viscosity. Depending on the local thickness of the cylinder where the droplet is created, smaller satellite droplets may form between larger drops, and with time, the larger droplets catch up with the smaller droplets and merge, changing the droplet pattern. We have captured the main steps of droplet merging, including bridge formation, and reformation into a large droplet. We have modelled the droplet merging by assuming lubrication flow on a conical geometry which closely matches the dynamics captured in the experiments. Understanding the motion and the interaction of droplets merging on a conical fiber can give insight into efficient methods of fog harvesting through modelling a realistic system of multiple droplets on conical fibers. Droplet pattern formation through the Plateau Rayleigh instability also gives insight into the process of self-patterning droplet on fibers.

Author contributions

CLL led the experimental effort with help from KDV, TSC led the theoretical effort with help from AC. CLL wrote the first draft of the manuscript, all authors contributed to the analysis and writing.

Conflicts of interest

There are no conflicts to declare.

Acknowledgements

CLL and KDV gratefully acknowledge the financial support by the Natural Science and Engineering Research Council of Canada. TSC and AC gratefully acknowledge financial support from the Research Council of Norway NANO2021 program (Project No. 301138) and the UiO:LifeScience initiative at the University of Oslo.

References

1 L. Guo and G. Tang, *Int. J. Heat Mass Transf.*, 2015, **84**, 198–202.
2 J. Ju, H. Bai, Y. Zheng, T. Zhao, R. Fang and L. Jiang, *Nat. Commun.*, 2012, **3**, 1247.
3 Z. Pan, W. G. Pitt, Y. Zhang, N. Wu, Y. Tao and T. T. Truscott, *Nat. Plants*, 2016, **2**, 16076.
4 Y. Zheng, H. Bai, Z. Huang, X. Tian, F.-Q. Nie, Y. Zhao, J. Zhai and L. Jiang, *Nature*, 2010, **463**, 640.
5 H. Bai, X. Tian, Y. Zheng, J. Ju, Y. Zhao and L. Jiang, *Adv. Mater.*, 2010, **22**, 5521.
6 A. R. Parker and C. R. Lawrence, *Nature*, 2001, **414**, 33.
7 Q. Wang, B. Su, H. Liu and L. Jiang, *Adv. Mater.*, 2014, **26**, 4880–4894.
8 F. T. Malik, R. M. Clement, D. T. Gethin, D. Beysens, R. E. Cohen, W. Krawszik and A. R. Parker, *Bioinspir. Biomim.*, 2015, **10**(3), 036005.
9 H. Chen, T. Ran, Y. Gan, J. Zhou, Y. Zhang, L. Zhang, D. Zhang and L. Jiang, *Nat. Mater.*, 2018, **17**, 935–942.
10 M. E. R. Shanahan, *Langmuir*, 2011, **27**, 14919.
11 K. Zhang, F. Liu, A. J. Williams, X. Qu, J. J. Feng and C.-H. Chen, *Phys. Rev. Lett.*, 2015, **115**, 074502.
12 Q. Wang, X. Yao, H. Liu, D. Quéré and L. Jiang, *Proc. Natl. Acad. Sci. U. S. A.*, 2015, **112**, 9247–9252.
13 P. Wang, R. Bian, Q. Meng, H. Liu and L. Jiang, *Adv. Mater.*, 2017, **29**(45), 1703042.
14 T. Xu, Y. Lin, M. Zhang, W. Shi and Y. Zheng, *ACS Nano*, 2016, **10**, 10681.
15 M. Cao, J. Ju, K. Li, S. Dou, K. Liu and L. Jiang, *Adv. Funct. Mater.*, 2014, **24**, 3235–3240.

Published on 03 January 2022. Downloaded by McMaster University on 5/11/2022 3:10:19 PM.

16 X. Heng, M. Xiang, Z. Lu and C. Luo, *ACS Appl. Mater. Interfaces*, 2014, **6**, 8032–8041.

17 E. Lorenceau and D. Quéré, *J. Fluid Mech.*, 2004, **510**, 29–45.

18 J. McCarthy, D. Vella and A. A. Castrejón-Pita, *Soft Matter*, 2019, **15**, 9997.

19 C. Fournier, C. Lee, R. Schulman, E. Raphaél and K. Dalnoki-Veress, *Eur. Phys. J. E: Soft Matter Biol. Phys.*, 2021, **44**, 1–6.

20 T. S. Chan, F. Yang and A. Carlson, *J. Fluid Mech.*, 2020, **894**, A26.

21 T. Gilet, D. Terwagne and N. Vandewalle, *Eur. Phys. J. E: Soft Matter Biol. Phys.*, 2010, **31**, 253–262.

22 H. Ji, C. Falcon, A. Sadeghpour, Z. Zeng, Y. S. Ju and A. L. Bertozzi, *J. Fluid Mech.*, 2019, **865**, 303–327.

23 E. Q. Li and S. T. Thoroddsen, *Phys. Fluids*, 2013, **25**, 052105.

24 F. Weyer, A. Duchesne and N. Vandewalle, *Sci. Rep.*, 2017, **7**, 13309.

25 T.-H. Chou, S.-J. Hong, Y.-E. Liang, H.-K. Tsao and Y.-J. Sheng, *Langmuir*, 2011, **27**, 3685–3692.

26 Y. Hou, L. Gao, S. Feng, Y. Chen, Y. Xue, L. Jiang and Y. Zheng, *Chem. Commun.*, 2013, **49**, 5253.

27 A. L. Yarin, W. Liu and D. H. Reneker, *J. Appl. Phys.*, 2002, **91**, 4751–4760.

28 T. S. Chan, C. L. Lee, C. Pedersen, K. Dalnoki-Veress and A. Carlson, *Phys. Rev. Fluids*, 2021, **6**, 014004.

29 C. Lv, C. Chen, Y.-C. Chuang, F.-G. Tseng, Y. Yin, F. Grey and Q. Zheng, *Phys. Rev. Lett.*, 2014, **113**, 026101.

30 J. Van Hulle, F. Weyer, S. Dorbolo and N. Vandewalle, *Phys. Rev. Fluids*, 2021, **6**, 024501.

31 A. Gupta, A. R. Konicek, M. A. King, A. Iqtidar, M. S. Yeganeh and H. A. Stone, *Phys. Rev. Fluids*, 2021, **6**, 063602.

32 S. Haefner, O. Baumchen and K. Jacobs, *Soft Matter*, 2015, **11**, 6921–6926.

33 R.-J. Roe, *J. Colloid Interface Sci.*, 1975, **50**, 70–79.

34 M. Safavi and S. S. Nourazar, *Theor. Comput. Fluid Dyn.*, 2021, **35**, 331–343.

35 F. Wang and U. D. Schiller, *Soft Matter*, 2021, **17**, 5486–5498.

36 K. Zhang, K. Fang, M. N. Bukhari, R. Xie, Y. Song, Z. Tang and X. Zhang, *Cellulose*, 2020, **27**, 9725–9736.

37 R. Labbé and C. Duprat, *Soft Matter*, 2019, **15**, 6946.

38 F. Weyer, M. Lismont, L. Dreesen and N. Vandewalle, *Soft Matter*, 2015, **11**, 7086–7091.

39 H. Lu, Z. Pan, H. Wang, Y. Liu, P. Dai and Q. Yang, *J. Hazard. Mater.*, 2021, **412**, 125188.

40 A. Koulago, V. Shkadov, D. Quéré and A. de Ryck, *Phys. Fluids*, 1995, **7**, 1221–1224.

41 G. K. Batchelor, *An Introduction to Fluid Dynamics*, Cambridge University Press, Cambridge, 1967.

42 A. Oron, S. H. Davis and S. G. Bankoff, *Rev. Mod. Phys.*, 1997, **69**, 931–980.

43 T. S. Chan, C. Pedersen, J. Koplik and A. Carlson, *J. Fluid Mech.*, 2020, **907**, A29.

44 A. Logg, K.-A. Mardal and G. Wells, *Automated solution of differential equations by the finite element method: The FEniCS book*, Springer Science & Business Media, 2012, vol. 84.

45 L. Rayleigh, *Proc. London Math. Soc.*, 1878, **s1–10**, 4–13.

This journal is © The Royal Society of Chemistry 2022

Chapter 5

Film coating by directional droplet spreading on fibers

Tak Shing Chan*, Carmen L. Lee*, Christian Pedersen, Kari Dalnoki-Veress, and Andreas Carlson
*co-first authorship
Physical Review Fluids 6, 014004. (2021).

5.1 Paper introduction

As a droplet moves along a conical fiber, as discussed in detail in Chapters 3 and 4, it can leave behind a thin film as it travels. In this paper, we characterized the deposited film that a droplet leaves behind as it travels along a conical fiber using asymptotic analysis, experiments, and numerical simulations using the lubrication equation. To understand the deposition process, one can imagine the droplet as a reservoir being pulled along the conical fiber. We find that the film thickness, h_f, follows the same scaling behaviour as predicted by Landau-Levich-Derjaguin (LLD) theory which is $h_f \approx l\mathrm{Ca}^{2/3}$, where Ca is the capillary number and l is the characteristic length scale based on the curvature of the system. However, we found that the relevant length scale l changed depending on the ratio between the fiber radius and droplet radius. For a large drop on a thin fiber, the curvature is dominated by the fiber radius because the large droplets approach the shape of an infinite bath. As a result, the length scale approaches the radius of the fiber, like in the classical LLD case of a cylindrical fiber as described in section 1.6.1. For small droplets relative to the fiber radius, the curvature of the droplet begins to affect the deposition due to the finite-size effect of the reservoir. The findings from this paper suggest that large droplets moving at the same speed as smaller droplets will deposit films of different thicknesses. We matched the experimentally measured film thicknesses and profiles to the numerical simulations with good agreement.

Numerical simulations were performed by Tak Shing Chan with support from Christian Pedersen and Andreas Carlson. I performed the experiments and analyzed the experimental data with help from Kari Dalnoki-Veress. Tak Shing Chan wrote the first draft of the manuscript and all of the authors contributed to editing subsequent drafts.

PHYSICAL REVIEW FLUIDS **6**, 014004 (2021)

Film coating by directional droplet spreading on fibers

Tak Shing Chan,[1,*] Carmen L. Lee,[2,*] Christian Pedersen,[1] Kari Dalnoki-Veress,[2,3]
and Andreas Carlson[1,†]
[1]*Department of Mathematics, Mechanics Division, University of Oslo, N-0851 Oslo, Norway*
[2]*Department of Physics and Astronomy, McMaster University, 1280 Main Street West,*
Hamilton, Ontario, Canada L8S 4M1
[3]*UMR CNRS Gulliver 7083, ESPCI Paris, PSL Research University, 75005 Paris, France*

(Received 10 August 2020; accepted 15 December 2020;
published 20 January 2021)

Plants and insects use slender conical structures to transport and collect small droplets, which are propelled along the conical structures due to capillary action. These droplets can deposit a fluid film during their motion, but despite its importance to many biological systems and industrial applications, the properties of the deposited film are unknown. We characterize the film deposition by developing an asymptotic analysis together with experimental measurements and numerical simulations based on the lubrication equation. We show that the deposited film thickness depends significantly on both the fiber radius and the droplet size, highlighting that the coating is affected by finite-size effects relevant to film deposition on fibers of any slender geometry. We demonstrate that by changing the droplet size, while the mean fiber radius and the capillary number are fixed, the thickness of the deposited film can change by an order of magnitude or more. We show that self-propelled droplets have significant potential to create passively coated structures.

DOI: 10.1103/PhysRevFluids.6.014004

I. INTRODUCTION

Droplets on slender conical substrates will self-propel due to capillary action [1–10] provided the droplets are smaller than the capillary length. This principle is used by insects [11,12] and plants [13–20] for droplet collection. Several studies have focused on mimicking structures found in nature to control liquid movement [21–27]. Recent work [13] has shown that the conically shaped trichomes on the underside of the lid of the *Sarracenia*, a pitcher plant, can transport droplets with a velocity several orders of magnitude larger than that found in other plants. Enhanced water transport is the result of surface lubrication of the trichome. The first droplet that slowly spreads across the trichome deposits a microscopic liquid film, and the following droplets slide along the lubricating film on the trichome. From a technological point of view, understanding the principles of film deposition by capillary-driven motion of droplets can provide pathways for relubrication of slippery liquid infused porous surfaces with conical shapes [6,28] as well as the development of other multifunctional materials. This lubricating film-coating principle has a fundamental role in biological phenomena and has untapped potential as a droplet-driven coating technique, yet the properties of the liquid film are unknown. We study here how droplets deposit lubricating films as they move along slender structures.

---

[*] These authors contributed equally to this work.

[†] acarlson@math.uio.no

©2021 American Physical Society

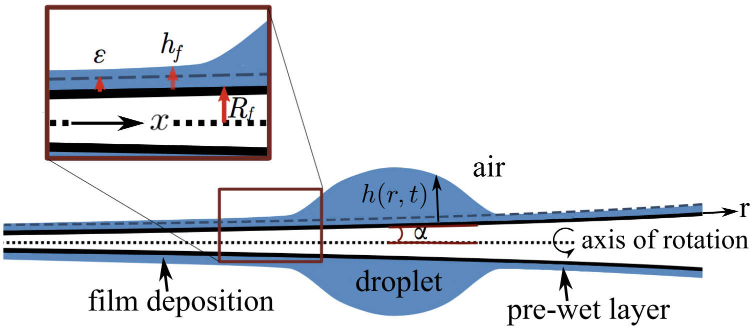

FIG. 1. (a) A sketch of a droplet on a conical fiber with a local cone angle α. Inset: zoom into the region connecting the deposited film of thickness h_f and the receding edge of the droplet at the fiber radius R_f. The fiber is prewet with a layer of the same fluid of thickness ϵ.

Coating a solid substrate with a lubricating liquid film as a way to reduce friction between substrates has been known since ancient Egypt [29]. The broad relevance of coating processes have made them widely studied, with great advances in understanding their underlying physical principles [30–34]. Dip-coating is today one of the most widespread coating techniques [35], where the solid moves with a velocity U relative to the liquid bath. The foundational work of Landau-Levich-Derjaguin (LLD) [36,37] has paved the way for a fundamental understanding of film deposition on solid substrates during wetting. By considering the viscous capillary flow of a liquid with a viscosity μ and a surface tension γ, LLD predicted that the deposited film thickness h_f, normalized by the characteristic length of the system L, is given by $h_f/L \sim \mathrm{Ca}^{2/3}$ [36,37], where the Capillary number $\mathrm{Ca} \equiv \mu U/\gamma$ is the ratio of the viscous and surface tension forces. The LLD theory was developed for $\mathrm{Ca} \ll 1$ and when inertia can be neglected. It is a generic scaling and has proven to be an accurate description of a wide range of coating phenomena, i.e., dip coating of plates [38], cylinders [31,39,40], and Bretherton bubbles [41]. However, a droplet depositing a film on a cylinder has a fundamental difference from film deposition from a liquid reservoir; the droplet size introduces another length scale to the system. The fiber geometry and droplet size are tuneable parameters to control the coating process [1,2].

II. THEORY AND EXPERIMENT

In the system studied here, a droplet deposits a film as it migrates toward the thicker part of a prewet conical fiber, driven by the curvature gradient, as shown schematically in Fig. 1. We investigate the system by combining asymptotic analysis, experiments, and numerical simulations. The assumptions made are that there is viscous flow driven by capillarity ($\mathrm{Ca} \ll 1$). Furthermore, we neglect gravitational effects because the drop size is much smaller than the capillary length, as is clear from the Bond number, which represents the balance between gravity and surface tension, $\mathrm{Bo} = \Delta\rho g V^{2/3}/\gamma \ll 1$, where $\Delta\rho$ is the density difference between the liquid and surrounding air, V is the droplet volume, and g is the gravitational acceleration. As will be seen below, these assumptions are verified by our experiments.

A. Asymptotic analysis

We start off by revising the classical LLD theory for the case of a droplet moving on a cylindrical fiber with radius R by matching asymptotically the quasistatic droplet profile on the fiber $h_s(x)$ and the self-similar deposited film profile (for details, see [4]). By matching the profiles, we show that the film thickness h_f scales with Ca as [4]

$$h_f = 1.338\ell \mathrm{Ca}^{2/3}, \tag{1}$$

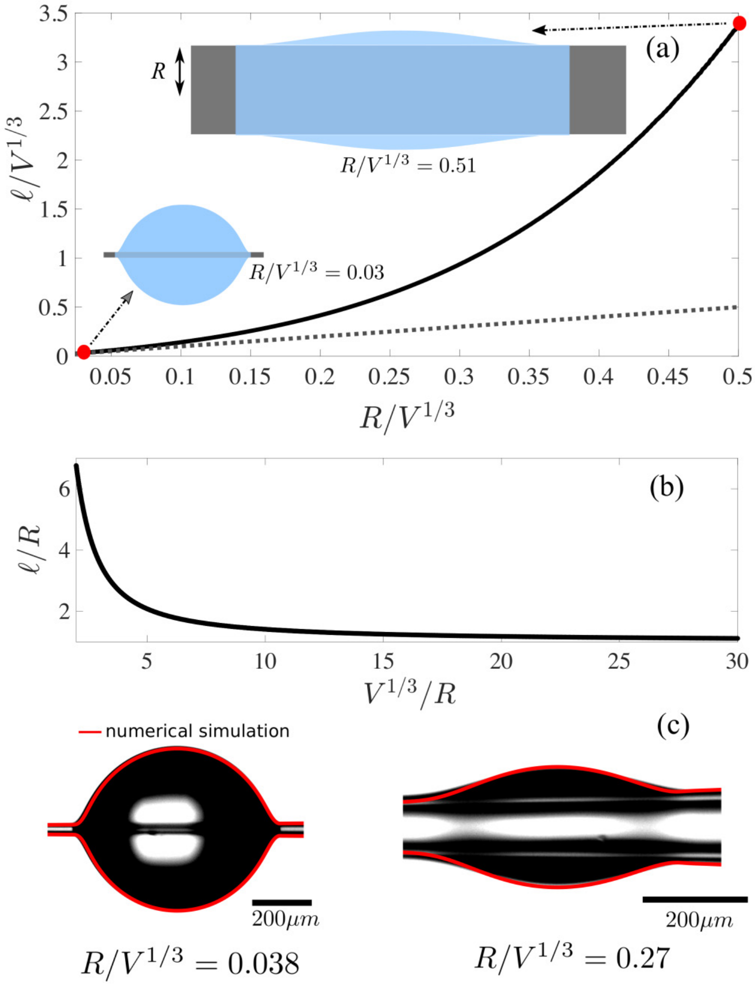

FIG. 2. (a) The dimensionless characteristic length $\ell/V^{1/3}$ as a function of the rescaled radius $R/V^{1/3}$ of a cylindrical fiber (solid line). The dotted line represents the linear relation, i.e., $\ell = R$. Inset: two static droplets of the same volume in contact with a fiber with $R/V^{1/3} = 0.03$ and 0.51 (indicated by the two red dots), which demonstrate different droplet shapes when R varies. The deposited film thickness h_f predicted by our asymptotic analysis scales linearly with ℓ for a given Capillary number Ca (dimensionless droplet velocity); see Eq. (1). From (a) we see that a droplet of a fixed volume coats a thicker film on a thicker fiber. In (b), ℓ rescaled by the fiber radius R is plotted as a function of $V^{1/3}/R$. It shows that for the same fiber radius, a smaller droplet coats a thicker film on the fiber. (c) Sample images of two droplets taken with optical microscopy (top views). Left: $\alpha = 0.43^\circ$ and $R/V^{1/3} = 0.038$, and right: $\alpha = 2.5^\circ$ and $R/V^{1/3} = 0.27$. The numerically calculated profiles from the lubrication theory on a cone [Eq. (2)] are shown in red for matching V, R, and α.

where $\ell \equiv 1/[\partial^2 h_s(x = x_{\mathrm{cl}})/\partial x^2]$ is the inverse of the second derivative of the static profile $h_s(x)$ evaluated at the contact line position $x = x_{\mathrm{cl}}$, i.e., where the profile $h_s(x)$ meets the solid substrate. A crucial difference from the classical LLD theory is that choosing $\ell = R$ only recovers the correct film thickness in the limit of $R \ll V^{1/3}$. In general, ℓ depends on both the droplet volume V and the fiber radius R, which indicates a finite-size effect. To illustrate this point, we plot $\ell/V^{1/3}$ as a function of $R/V^{1/3}$ in Fig. 2(a). In the limit where $R \ll V^{1/3}$, $\ell = R$, then the film thickness $h_f = 1.338 R\,\mathrm{Ca}^{2/3}$ is independent of the droplet volume. However, when $R/V^{1/3} \gtrsim 0.15$, the droplet size starts to play a significant role in predicting the deposited film thickness that is much larger than if we would naively assume $\ell = R$. Since $\ell/V^{1/3}$ increases with $R/V^{1/3}$ faster than a linear relation, Eq. (1) also implies that a smaller droplet deposits a thicker film for fixed R and Ca. This property is shown in Fig. 2(b), in which ℓ/R decreases with increasing $V^{1/3}/R$. For the directional spreading of droplets on a conical fiber with a small cone angle α, the influence of α on ℓ only appears as high-order corrections, which are neglected here (see [4] for details). The conical geometry acts as a factor that generates the spontaneous motion of the droplet and plays a role in determining the magnitude of Ca. The theoretical prediction for the film thickness dependence on the droplet size and the fiber radius [see Eq. (1)] can now be compared to experiments and numerical simulations based on the lubrication theory.

B. Experiments

The conical substrates used in the experiments are prepared by pulling standard borosilicate glass capillary tubes in a magnetic micropipette puller (Narishige PN-30). The resulting shape of the capillary tube is a nearly conical fiber with a smoothly varying diameter and gradient, with a smaller cone angle nearing the tip of the fiber. The gradient in the cone angle varies slowly along the fiber, thus on the length scale of the droplet the fibers can be treated as ideal. Droplets of silicone oil with viscosity of $\mu \approx 4.9$ Pa s, and with air-liquid surface tension $\gamma = 22$ mN/m, were deposited at the fiber tip. Silicone oil is ideal because it is totally wetting, chemically stable, nonvolatile, and nonhygroscopic. The fiber is prewet by placing a droplet on the tip of the fiber and allowing it to migrate from one end of the fiber to the other, thereby depositing a film. Prewet film thicknesses were found to range from 0.27 to 13.87 μm, as determined by optical microscopy (OM) using an upright microscope (Olympus BX51) with bottom illumination. OM images of the fiber were taken from above both before and after coating, and they were used to obtain the film thickness. Droplets of volumes V in the range of 0.009–1.99 mm^3, i.e., Bo $\in$ [0.02-0.7], were deposited onto the fiber. Images of the droplet are taken as it migrates along the fiber at a given radius R, and the deposited film is observed as the droplet passes a given location. To ensure the effects of gravity are not affecting the dynamics, a similar experiment was performed in which the entire experimental setup was tilted at different angles to measure if there were any changes in droplet motion in the plane of gravity. There were no discernible differences in droplet motion, and thus the effects of gravity are negligible. The radii of the cone at the measured film thicknesses ranged between 22.26 and 103.92 μm and the deposited film thicknesses were measured in the range of 0.17–19.75 μm.

C. Numerical simulations

To give a mathematical description of the droplet flow on the prewet fiber, we turn to the lubrication approximation for the viscous incompressible flow, when the cone angle $\alpha \ll 1$. The thin-film equation is obtained by reducing the Navier-Stokes equations for flow in films with large lateral dimensions in relation to the thickness [42,43], in combination with mass conservation. A detailed derivation of the lubrication approximation on a conical geometry for $\alpha \ll 1$ is found in [3]. Note that we impose a no-slip condition at the solid substrate and no-shear stress at the free surface. The axisymmetric liquid-air interface profile is given by $h = h(r,t)$, defined as the distance between the interface and the substrate, as a function of the radial distance from the vertex of the cone r and time t. The evolution of the free surface is described by [3,4],

$$\frac{\partial h}{\partial t} + \frac{1}{r\alpha + h}\frac{\partial}{\partial r}\left(M\frac{\partial p}{\partial r}\right) = 0, \tag{2}$$

where the mobility $M = M(h,r,\alpha)$ reads

$$M(h,r,\alpha) = \frac{r^4\alpha^4}{2\mu}\left\{\frac{1}{8}\left[3\left(1+\frac{h}{r\alpha}\right)^4 - 4\left(1+\frac{h}{r\alpha}\right)^2 + 1\right] - \frac{1}{2}\left(1+\frac{h}{r\alpha}\right)^4 \ln\left(1+\frac{h}{r\alpha}\right)\right\}. \tag{3}$$

The capillary pressure gradient in the liquid generates the flow, and the pressure $p = p(r,t)$ reads

$$p = -\gamma\left\{\frac{\frac{\partial^2 h}{\partial r^2}}{\left[1+\left(\frac{\partial h}{\partial r}\right)^2\right]^{3/2}} - \frac{1-\alpha\frac{\partial h}{\partial r}}{(r\alpha+h)\left[1+\left(\frac{\partial h}{\partial r}\right)^2\right]^{1/2}}\right\}, \tag{4}$$

where the expression is simplified for $\alpha \ll 1$ [3,4]. Equations (2) and (4) are discretized by linear elements and numerically solved with a Newton solver by using the open source finite-element code FEniCS [44]; additional details about the numerical approach are found in [4]. The initial condition is a droplet smoothly connected to a prewet film of thickness ϵ. At the two boundaries ($\delta\Omega$) of the numerical domain, we impose $h(\delta\Omega, t) = \epsilon$ and $p(\delta\Omega, t) = \gamma/R(\delta\Omega)$, where $R(\delta\Omega)$ is the radius of the cone at the boundaries. We note that only the droplet volume V is important, and the initial droplet shape does not affect the results.

III. RESULTS AND DISCUSSION

We start by comparing the droplet spreading dynamics on two cones with $\alpha = 0.43^\circ$ and 2.5°, where the droplet quickly relaxes from its initial condition to its quasistatic shape and then starts to translate to the thicker part of the fiber. When we overlay the experimental measurement with the numerical simulations, as shown in Fig. 2(c), we see that the two results are in close agreement. By zooming into the trailing edge of the droplet, both the experiment and the numerical simulation show the deposition of a film of different thickness from that of the prewet film ϵ.

Next we turn to characterize the thickness of the film during the droplet spreading dynamics on the fiber. To determine the Ca, we extract the droplet velocity U measured at its center of mass. The film is measured on the cone after the droplet has deposited the film, which is stable throughout the observation time in the experiments and the numerical simulations. The Rayleigh-Plateau instability is expected to take place at much longer times as the time scale of the fastest growing mode for a film coated on a cylinder with similar radius is predicted to be more than an order of magnitude longer than both the experimental observation time and the simulation time. Since there is a slight gradient in the cone angle along r in the fiber used in the experiments, we extract the cone angle locally at a given position on the cone with radius $R = R_f$. Here R_f is the cone radius in the receding region, defined based on the droplet profile; see [4]. The deposited film thickness h_f is then a function of α, R_f, V, and ϵ. We combine all the experimental measurements and the numerical predictions of $h_f \in [0.17 - 19.75]$ μm, i.e., for $\alpha \in [0.35 - 2.3]^\circ$, in Fig. 3(a), and they are in good agreement. The film thickness is not uniform along the fiber for a fixed cone angle, but increases with the cone radius R_f. The film thickness h_f increases by roughly one order of magnitude when the cone angle α is varied from 0.35° to 2.3°.

To further compare the theory to the experiments and numerical simulations, we rescale our measurements according to Eq. (1) and also plot the analytical prediction; see Fig. 3(b). Since the motion of the droplet is driven by capillarity, i.e., it is self-propelled, the droplet velocity is a function of the position on the cone. The deposited film thickness h_f rescaled by ℓ obtained from the experiments and the lubrication theory on a cone is shown as a function of Ca in Fig. 3(b). When comparing the results (1) predicted by the asymptotic matching, the experiments, and the numerical simulations, we observe that they are in close agreement, especially for the smallest cone angles. When α increases, there is a slight deviation from $2/3$ scaling observed in the numerical simulations with a slightly larger film thickness than predicted from Eq. (1), likely a consequence of the reduced separation of length scales between the film thickness h_f and the droplet size $V^{1/3}$.

We show that self-propelled droplets have a significant potential to create passively coated structures. By combining an asymptotic analysis, experiments, and numerical simulations of the lubrication equation, we have demonstrated that a droplet that moves on a fiber can deposit a film with a thickness h_f, controlled by the droplet's capillary number and the characteristic length ℓ. The quantity ℓ is a geometric factor that is linear with respect to the fiber radius R when $R/V^{1/3} \ll 1$, i.e., the droplet is much greater in size than the fiber radius. Otherwise, $\ell/V^{1/3}$ increases significantly with $R/V^{1/3}$ when $R/V^{1/3} \gtrsim 0.15$. Our finding has direct implications for control of film deposition during spreading, e.g., if we fix the fiber radius, decreasing the droplet size can increase the thickness of the deposited film by an order of magnitude or more at the same Ca. Coating by droplets introduces novel design features that do not exist in classical coating techniques where the substrate is connected to a liquid reservoir. For a droplet moving on a cylindrical fiber driven

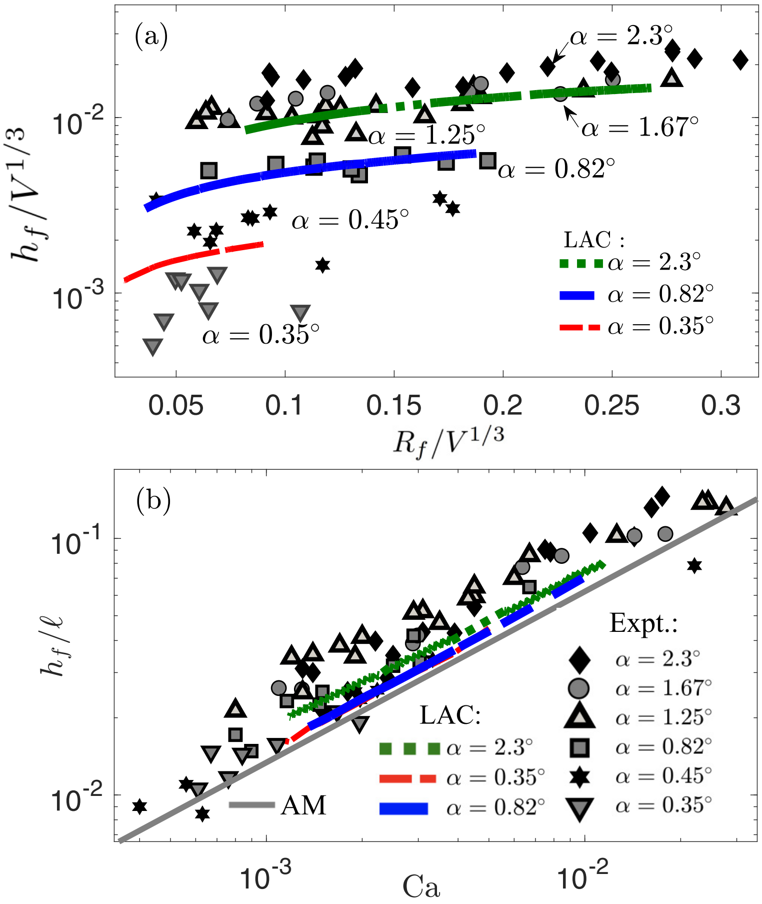

FIG. 3. (a) The deposited film thickness h_f as a function of the cone radius R_f and the cone angle α. Both axes are normalized by $V^{1/3}$. Symbols are experimental data and curves are numerical results from the lubrication theory on a cone (LAC). The prewet layer thickness ϵ in both the experiment and the theory is controlled within a range of 0.27-13.87 μm. (b) The film thickness h_f rescaled by ℓ as a function of the capillary number Ca. The solid line (AM) is the result of asymptotic matching given by Eq. (1).

by external forces, e.g., electric, magnetic, and gravitational, the deposited film thickness follows Eq. (1), whereas Ca depends on the magnitude of the driving force. Our findings are expected to be relevant for any droplet coating application involving a slender geometry, and they may help shed light on why slender conical structures have evolved in a diverse set of biological systems to facilitate efficient droplet transport.

ACKNOWLEDGMENTS

T.S.C. and A.C. gratefully acknowledge financial support from the Research Council of Norway (Project No. 301138) and the UiO:LifeScience initiative at the University of Oslo. C.L.L. and K.D.-V. acknowledge financial support from the Natural Science and Engineering Research Council of Canada.

[1] É. Lorenceau and D. Quéré, Drops on a conical wire, J. Fluid Mech. **510**, 29 (2004).
[2] E. Q. Li and S. T. Thoroddsen, The fastest drop climbing on a wet conical fibre, Phys. Fluids **25**, 052105 (2013).
[3] T. S. Chan, F. Yang, and A. Carlson, Directional spreading of a viscous droplet on a conical fibre, J. Fluid Mech. **894**, A26 (2020).

[4] T. S. Chan, C. Pedersen, J. Koplik, and A. Carlson, Film deposition and dynamics of a self-propelled wetting droplet on a conical fibre, J. Fluid Mech. **907**, A29 (2021).

[5] Y.-E. Liang, H.-K. Tsao, and Y.-J. Sheng, Drops on hydrophilic conical fibers: Gravity effect and coexistent states, Langmuir **31**, 1704 (2015).

[6] J. McCarthy, D. Vella, and A. A. Castrejón-Pita, Dynamics of droplets on cones: Self-propulsion due to curvature gradients, Soft Matter **15**, 9997 (2019).

[7] P. Renvoisé, J. W. M. Bush, M. Prakash, and D. Quéré, Drop propulsion in tapered tubes, Europhys. Lett. **86**, 64003 (2009).

[8] T.-H. Chou, S.-J. Hong, Y.-E. Liang, H.-K. Tsao, and Y.-J. Sheng, Equilibrium phase diagram of drop-on-fiber: Coexistent states and gravity effect, Langmuir **27**, 3685 (2011).

[9] J.-L. Liu, R. Xia, B.-W. Li, and X.-Q. Feng, Directional motion of droplets in a conical tube or on a conical fibre, Chin. Phys. Lett. **24**, 3210 (2007).

[10] X.-F. Wu and Y. A. Dzenis, Droplet on a fiber: Geometrical shape and contact angle, Acta Mech. **185**, 215 (2006).

[11] Y. Zheng, H. Bai, Z. Huang, X. Tian, F.-Q. Nie, Y. Zhao, J. Zhai, and L. Jiang, Directional water collection on wetted spider silk, Nature (London) **463**, 640 (2010).

[12] A. R. Parker and C. R. Lawrence, Water capture by a desert beetle, Nature (London) **414**, 33 (2001).

[13] H. Chen, T. Ran, Y. Gan, J. Zhou, Y. Zhang, L. Zhang, D. Zhang, and L. Jiang, Ultrafast water harvesting and transport in hierarchical microchannels, Nat. Mater. **17**, 935 (2018).

[14] L. Guo and G. H. Tang, Experimental study on directional motion of a single droplet on cactus spines, Int. J. Heat Mass Transf. **84**, 198 (2015).

[15] J. Ju, H. Bai, Y. Zheng, T. Zhao, R. Fang, and L. Jiang, A multi-structural and multi-functional integrated fog collection system in cactus, Nat. Commun. **3**, 1247 (2012).

[16] C. Luo, Theoretical exploration of barrel-shaped drops on cactus spines, Langmuir **31**, 11809 (2015).

[17] Z. Pan, W. G. Pitt, Y. Zhang, N. Wu, Y. Tao, and T. T. Truscott, The upside-down water collection system of syntrichia caninervis, Nat. Plants **2**, 16076 (2016).

[18] F. T. Malik, R. M. Clement, D. T. Gethin, D. Beysens, R. E. Cohen, W. Krawszik, and A. R. Parker, Dew harvesting efficiency of four species of cacti, Bioinspir. Biomim. **10**, 036005 (2015).

[19] M. E. R. Shanahan, On the behavior of dew drops, Langmuir **27**, 14919 (2011).

[20] X. Tan, T. Shi, Z. Tang, B. Sun, L. Du, Z. Peng, and G. Liao, Investigation of fog collection on cactus-inspired structures, J. Bionic Eng. **13**, 364 (2016).

[21] Y. Chen, L. Wang, Y. Xue, L. Jiang, and Y. Zheng, Bioinspired tilt-angle fabricated structure gradient fibers: Micro-drops fast transport in a long distance, Sci. Rep. **3**, 2927 (2013).

[22] H. Bai, X. Tian, Y. Zheng, J. Ju, Y. Zhao, and L. Jiang, Direction controlled driving of tiny water drops on bioinspired artificial spider silks, Adv. Mater. **22**, 5521 (2010).

[23] M. Cao, J. Ju, K. Li, S. Dou, K. Liu, and L. Jiang, Facile and large-scale fabrication of a cactus-inspired continuous fog collector, Adv. Funct. Mater. **24**, 3235 (2014).

[24] X. Heng, M. Xiang, Z. Lu, and C. Luo, Branched zno wire structures for water collection inspired by cacti, ACS Appl. Mater. Interfaces **6**, 8032 (2014).

[25] Y. Hou, L. Gao, S. Feng, Y. Chen, Y. Xue, L. Jiang, and Y. Zheng, Temperature-triggered directional motion of tiny water droplets on bioinspired fibers in humidity, Chem. Commun. **49**, 5253 (2013).

[26] J. Ju, K. Xiao, X. Yao, H. Bai, and L. Jiang, Bioinspired conical copper wire with gradient wettability for continuous and efficient fog collection, Adv. Mater. **25**, 5937 (2013).

[27] T. Xu, Y. Lin, M. Zhang, W. Shi, and Y. Zheng, High-efficiency fog collector: Water unidirectional transport on heterogeneous rough conical wires, ACS Nano **10**, 10681 (2016).

[28] T.-S. Wong, S. H. Kang, S. K. Y. Tang, E. J. Smythe, B. D. Hatton, A. Grinthal, and J. Aizenberg, Bioinspired self-repairing slippery surfaces with pressure-stable omniphobicity, Nature (London) **477**, 443 (2011).

[29] D. Dowson, *History of Tribology*, 2nd ed. (Wiley, London, 1998).

[30] K. J. Ruschak, Coating flows, Annu. Rev. Fluid Mech. **17**, 65 (1985).

[31] D. Quéré, Fluid coating on a fiber, Annu Rev. Fluid Mech. **31**, 347 (1999).

[32] S. J. Weinstein and K. J. Ruschak, Coating flows, Annu. Rev. Fluid Mech. **36**, 29 (2004).

[33] J. H. Snoeijer, J. Ziegler, B. Andreotti, M. Fermigier, and J. Eggers, Thick Films of Viscous Fluid Coating a Plate Withdrawn from a Liquid Reservoir, Phys. Rev. Lett. **100**, 244502 (2008).

[34] E. Rio and F. Boulogne, Withdrawing a solid from a bath: How much liquid is coated? Adv. Colloid Interface Sci. **247**, 100 (2017).

[35] P.-G. de Gennes, F. Brochart-Wyart, and D. Quéré, *Capillarity and Wetting Phenomena: Drops, Bubbles, Pearls, Waves* (Springer, New York, 2003).

[36] L. D. Landau and B. V. Levich, Dragging of a liquid by a moving plate, Acta Phys.-Chim. USSR **17**, 42 (1942).

[37] B. V. Derjaguin, On the thickness of a layer of liquid remaining on the walls of vessels after their emptying, and the theory of the application of photoemulsion after coating on the cine film, Acta Phys.-Chim. USSR **20**, 349 (1943).

[38] M. Maleki, M. Reyssat, F. Restagno, D. Quéré, and C. Clanet, Landau-Levich menisci, J. Colloid Interface Sci. **354**, 359 (2011).

[39] A. De Ryck and D. Quéré, Inertial coating of a fibre, J. Fluid Mech. **311**, 219 (1996).

[40] A. Q. Shen, B. Gleason, G. H. McKinley, and H. A. Stone, Fiber coating with surfactant solutions, Phys. Fluids **14**, 4055 (2002).

[41] F. P. Bretherton, The motion of long bubbles in tubes, J. Fluid Mech. **10**, 166 (1961).

[42] G. K. Batchelor, *An Introduction to Fluid Dynamics* (Cambridge University Press, Cambridge, 1967).

[43] A. Oron, S. H. Davis, and S. G. Bankoff, Long-scale evolution of thin liquid films, Rev. Mod. Phys. **69**, 931 (1997).

[44] A. Logg, K.-A. Mardal, and G. Wells, *Automated Solution of Differential Equations by the Finite Element Method: The FEniCS Book* (Springer Science & Business Media, Berlin, 2012), Vol. 84.

Chapter 6

Buckling instabilities in moving chains of bubbles

Carmen L. Lee and Kari Dalnoki-Veress
To be submitted.

6.1 Paper introduction

The final paper of this thesis studies the buckling of a chain of bubbles as it moves through an aqueous bath. Inspired by the coiling of ropes and viscous threads [105, 106, 107, 98], this project studies how a 'granular' rope bends and buckles. Micron-scale air bubbles are produced out of an orifice, and the bubbles rise due to buoyancy. If the bubbles are produced quickly, they come into contact with one another and stick together due to short range adhesive forces and rise through an aqueous bath. Increasing the bubble production speed further, the chain begins to buckle. As the chain moves upwards due to buoyancy, drag force opposes the motion and induces a compressive force on the bubble chain. Because the chain does not have a bending modulus and the bubbles are frictionless as they move around each other, the chain should not be able to sustain any axial compression and should buckle in a random manner. We instead found that when the chain moved through the fluid, a regular buckling pattern developed. In this paper, we develop a simple model that considers viscous drag to both drive the buckling instability and to stabilize the chain. We have shown that in the absence of a bending modulus, hydrodynamic effects still create a regularly buckled structure. From the model, we can predict the conditions required for buckling, the speed of the chain as it moves through the bath and the amplitude of the buckling. We compare measured values from the experiment to the values predicted by the model and find excellent agreement.

I conducted the experiments, data analysis and theory included in this paper, with theory inputs from Kari Dalnoki-Veress. I wrote the original draft with editing of subsequent versions of the manuscript done by myself and Kari Dalnoki-Veress.

Buckling instabilities in moving chains of bubbles

Carmen L. Lee
Department of Physics & Astronomy, McMaster University, Hamilton, Ontario, L8S 4M1, Canada

Kari Dalnoki-Veress*
Department of Physics & Astronomy, McMaster University, Hamilton, Ontario, L8S 4M1, Canada and UMR CNRS Gulliver 7083, ESPCI Paris, PSL Research University, 75005 Paris, France

(Dated: July 22, 2022)

A slender object undergoing an axial compression will begin to buckle to alleviate the compression, and the buckling is balanced by bending stiffness for solids or viscosity for liquid threads. We study a chain of uniform sticky bubbles that undergoes a buckling instability in a viscous bath notably in the absence of both bending and viscous resistance within the chain. Producing the bubbles quickly induces a compressive stress as viscous drag exceeds buoyant forces and due to the frictionless nature of the bubble chain, it buckles easily. Using low Reynolds number hydrodynamics and geometric arguments, we predict the critical buckling speed, the terminal speed of a buckled chain and the amplitude of the buckles.

Slender objects, like strands of hair, rope or blades of grass are easy to buckle and bend if they are compressed along the axial direction. Buckling can occur on a multitude of length scales from macroscopic, like a rope hitting the ground [1, 2], to microscopic, like the bending of flagella while micro-organisms swim [3–6]. If the stress on the slender object is regular, it will undergo a regular deformation, for example a rope fed at a constant speed through a frictional nozzle will bend with a characteristic wavelength determined by the experienced friction and bendability of the rope [7]. Interestingly, this phenomenon is not confined only to solid materials and can also be seen with thin viscous threads of liquid. For instance, a stream of honey coils when it falls onto a piece of toast [8–15]. Here the viscosity of the liquid resists the bending of the thread, and a regular coiling is developed [14]. In addition to buckling and coiling due the presence of a barrier, viscous drag has been shown to induce buckling of slender structures as the structure is moved through the liquid, as shown in the work by Gosselin *et al.* [16] for solid threads and Chakrabarti *et al.* [11] for gelling structures. Viscous drag causes a stress along the length of the thread, rather than localizing it at the location of the barrier. Coiling and buckling has applications from orogeny in geosciences to the coiling of DNA structures and is a common concern of those building bridges and other structures [5]. Coiling and buckling of slender fibers has continues to be explored for applications in the context of easily creating metamaterials [17, 18] to creating nanostructures through 3D printing [19–21] and electrospinning [22, 23].

In this Letter, we experimentally investigate the buckling of a slender chain of sticky, uniform air bubbles in an aqueous bath (Fig 1a)-e)). The bubbles are produced at the bottom of the chamber from a small orifice and rise upwards, and by producing the bubbles quickly such that each subsequent bubble is produced before the other bubble has risen by a distance of one diameter, the two adhere due to short-range depletion forces. Producing several bubbles in a row create a linear chain (Fig 1a). Upon increasing the bubble production speed further, the hydrodynamic drag force exceeds the buoyant force for a given length, the linear chain is no longer stable, and begins to buckle (Fig1b)-e). From three-dimensional reconstructions (Fig1f)-j), buckling takes place in a two dimensional plane and takes the shape of a granular sinusoid. The planar buckling of the chain is likely due to a breaking of symmetry due to the direction that the bubbles are initially expelled from the production orifice, creating an initial direction of preferred motion. We note that the buckling here is due to viscous drag on the chain, similar to the work by Gosselin *et al.* [16] and Chakrabarti *et al.* [11] with the important distinction that instead of a continuous medium with intrinsic material properties, whereas our system is a granular material held together with only short range attractions, and thus there is no intrinsic cost to deformation. We first investigate the balance between hydrodynamic drag and buoyancy in the terminal velocity of the chain. We then explore the relationship between bubble size, production speed and viscosity and identify a critical speed that the chain needs to be produced to induce buckling. Finally, we relate the buckling amplitude to the excess amount of chain created. In all of these models, we consider solely hydrodynamic interactions, and the proposed scaling behaviour are in excellent agreement with our experiments.

Sample images of our buckling experiment are shown in Fig. 1a)-e).A chain of bubbles with radius R is produced at speed q and moves with terminal speed v in the vertical direction and buckles with an amplitude A and wavelength λ (as described in Fig. 1 k)) is created by forcing air through a thin, double-pulled micropipette (Narishige, capillary tubes from World Precision Instruments) into an aqueous bath (density $\rho = 1$ kg/m^3, viscosity 1.5 mPa s $< \eta <$ 2.0 mPa s) composed of HPLC water (Sigma-Aldrich), 1.5% by weight NaCl (Caledon)

---

[*] Corresponding author: dalnoki@mcmaster.ca

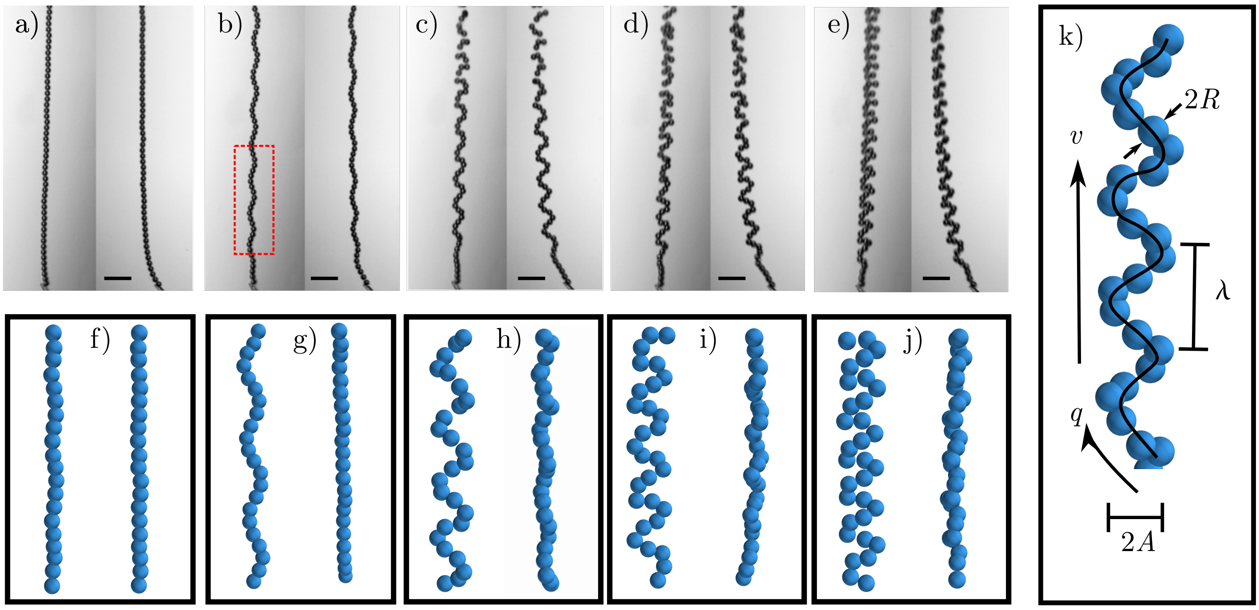

FIG. 1. Panels a)-e) show images of a bubble chain undergoing a buckling instability as the bubble production speed is increased from left to right ranging from 7.8 mm/s to 27.2 mm/s. Each panel shows images of the same chain taken at two orthogonal planes to allow for 3-dimensional reconstruction. Faster bubble production speed increases the buckling amplitude. Scale bar corresponds to 250 μm. Panels f)-j) show the 3-dimensional reconstruction of a short segment (size of reconstruction is shown in panel b) by the red dashed box) of the bubbles rotated to show the angle with maximum buckling amplitude, and the corresponding orthogonal angle. Each reconstructed panel corresponds to the matching images above. Panel k) shows the relevant geometric values including the terminal velocity v, chain production speed q, bubble radius R, wavelength λ and amplitude A.

and a range of sodium dodecyl sulfate (SDS, Bioshop) from 1% to 8% concentration by weight. Changing the concentration of SDS changes the adhesion between bubbles [24]. The adhesion is used to keep the chain attached and to resist breaking apart due to viscous torque on different parts of the chain. The pressure through the micropipette is kept constant over each of the trials by using a syringe and plunger. We note that for the small amounts of air being expelled through the micropipette, we can treat the amount of air as an infinite reservoir and thus constant, this is confirmed by the constant bubble size over time frame of the trial [25, 26]. Changing the size of the micropipette orifice creates bubbles with radius R range over $16 < R < 38$ μm, and at these small length scales the bubbles have a Laplace pressure large enough that we can treat them as hard, incompressible spheres as evidenced by Bond numbers $<< 1$. In the studied system with droplets on the order of 30 μm in size, viscosity of the bath of 1.5-2.0 mPa s, the Reynolds number is $\mathrm{Re} = \frac{\rho g R v}{\mu} < 1$, and viscous forces dominate inertial ones. The aqueous bath is held by a mirrored chamber with two mirrors set at 22.5° to the normal plane to allow for simultaneous imaging of two orthogonal planes of the bubble chain. Image analysis was done with a combination of edge detection, particle tracking techniques with an in-house python script.

Critical production speed for buckling onset- We first focus on understanding the critical speed q_c that the chain needs to be extruded to transition between an unbuckled chain at low q and a buckled chain at higher q. At low bubble production speeds q, the bubbles naturally align in the vertical direction due to buoyant forces F_b. The buoyancy per bubble is $dF_b = \frac{4}{3}\,\pi\,R^3\,\Delta\rho\,g\,dn$, where $\Delta\rho$ is the difference in buoyancy between the air and the bath, g is the gravitational acceleration, and n is the number of bubbles. Given the small Re in these experiments, we expect the hydrodynamic drag per unit length that is opposing the motion upwards takes the general expression of $dF_d = c\,q\,\mu\,dl$, where μ is the viscosity of the bath, q is the that the chain is being produced, c is a dimensionless drag coefficient, and l is the length of the chain [27, 28]. To compare the drag force to the buoyant forces, we can use the conversion of $dl = 2R\,dn$ which relates the axial length of the chain to the diameter of the bubbles and the number of bubbles present in that chain segment.

Initially, bubbles form a straight chain (Fig. 1a)) but as the bubble production rate q increases, the chain speed increases as the newly produced bubbles begin to push on the bottom of the chain, a competition between drag and buoyancy creates a compressive force along the axial direction of the chain, which is alleviated by buckling the chain out of the axial direction. The addition of one more bubble means that there's a greater number of bubbles pulling upward, but also a greater length for the drag to be acting on. The compressive force

$dF_c = 2\pi R^2 \Delta\rho g\, dl/3 - c_n \mu q\, dl$. We note that these bubbles are frictionless and able to move rotate around the other freely, and as such there is no bending cost to the chain like a solid rope [1] would nor internal viscous cost like a viscous thread [14]. In this case, hydrodynamic drag in the normal direction prevents the bubble chain from collapsing on itself. We can understand then that the axial compression will turn into a buckle when the compressive force is equal to the force required to move one of the bubbles out of line of the chain. The force required to do this is simply the drag force acting on the bubble as it moves a distance of R at a speed of q, the same speed that the chain is moving. Using Stokes' law, we know that the shear drag force required to do this is $dF_s = c_o\, q\, R\, \mu$, where c_o is the normal drag coefficient. Equating the compressive force with the shear drag force and rearranging for the critical bubble production speed q_c gives

$$q_c = \frac{2\pi\, R^2\, \Delta\rho\, g}{3c_s\, \mu}, \tag{1}$$

where c_s is a drag coefficient as a combination between the axial and normal drag coefficients. Figure 2 shows data for the bubble production speed as a function of the relationship outlined in equation 1. The data points corresponding to a dark color blue are those for unbuckled chains, the lighter pink color corresponds to data for buckled chains. The resulting data creates a phase diagram, separated by the predicted relation in equation 1, with a dimensionless fit factor of 1.85 ± 0.02 corresponding to the drag coefficients present in the axial and normal directions. The excellent agreement between the data and theory indicate that we can predict the critical bubble production speed required to begin buckling a chain of bubbles. We note here that there is no bending, as compared to previous work on buckling of slender objects, and this makes an agreement using hydrodynamics instead.

The terminal velocity of the chain- As the bubbles are produced, the effect of the increased production speed is only sustained over the first small number of bubbles, this makes sense, as anyone who has tried to push the end of a rope knows that the buckling happens near the location of the push. Well beyond the production orifice, each of the bubbles only moves in the vertical direction and does not translate along the arc length of the chain *i.e.* each bubble only has a vertical component to its velocity. Since Re is small for this system and there will be fluid entrained between the spaces of the bubbles, it is informative to treat the buckled chain as a ribbon moving upwards through the liquid. The motion of the chain is driven by the buoyant force acting on the bubbles. We can consider the buoyant force per unit length along the vertical direction of the chain $\hat{x}$, using the conversion between the number of bubbles along the axial length $ds = 2R\, dn$ and the requirement that the amount of length must be conserved. Because the chain is moving with a constant speed, we can balance the buoyant force unit length with the drag force per unit length and derive an expression for the expected terminal velocity of the chain. Considering the global motion of the chain v is determined by the drag force on the chain as a whole, created by the drag force acting on the whole chain, which we can approximate as $c\, \mu\, v\, dx$, where μ is the viscosity of the bath, c is a drag coefficient taken to be constant for all of the chains, v is the terminal velocity of the chain, and dx is the infinitesimal length in the vertical direction. Balancing these two forces gives the speed as a function of the bubble radius, production rate and viscosity,

$$v \propto \sqrt{\frac{R^3 q}{\mu}}. \tag{2}$$

The proposed scaling is plotted in figure 3, for several data sets at varying q, and R and μ. We expect that the terminal speed will increase with increasing chain production speed based on the images in figure 1, as the bubbles are more densely packed and therefore the buoyancy per unit length should increase. We note that we did not set out to vary the viscosity of the bath, but in changing the concentration of the SDS in the bath, the increased number of micelles also changed the viscosity [29]. The expected relationship defined in equation 2 and the measured data show excellent agreement, with the only fit factor being the drag coefficient. Although the hydrodynamic drag has been coarse-grained in this equation as we have modelled this as a ribbon with drag coefficient c, this proves to be an adequate approxima-

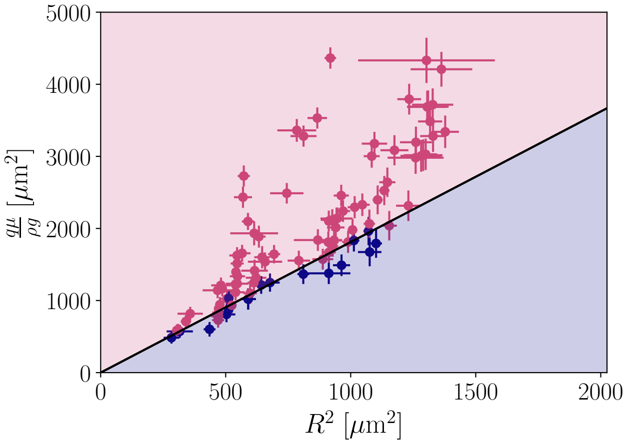

FIG. 2. A phase diagram showing the critical chain production speed q_c normalized by the ratio of inertial forces to viscous forces, as a function of the bubble radius R squared. The dark blue data points indicate an unbuckled chain, where the light pink data points indicate buckled chains. The black line corresponds to the predicted theoretical relationship in equation 1 with a constant fit parameter corresponding to the dimensionless drag coefficient 1.85 ± 0.02.

tion due to the agreement between the model and the experiment as well as the large amount of fluid entrainment between the bubbles of the chain. We note that a full understanding of the hydrodynamics could be studied using simulation however this is outside of the scope of this current study.

Buckling amplitude- From figure 1, one can see that the buckling amplitude A increases with increasing chain productions speed q and to understand the relationship between A and q we consider a geometric argument. We reason that the buckling occurs because of an excess of chain length that is produced relative to the speed that the chain can move upwards. For the amount of chain length that is produced, some amount translates in the vertical direction, x, and the rest must translate in the horizontal direction. If there is chain produced faster than the chain can move globally, i.e. $q > v$, there will be an excess of length that must move in the horizontal direction. In this system, the buckling is confined to two dimensions, and we choose to model the buckled shape of the chain as a zigzag with a wavelength λ and amplitude A. By calculating the arc length s for one wavelength, and rearranging for the amplitude, we find $A^2 \approx (s^2 - \lambda^2)/4$.

Due to variations in the data and noise in defining wavelengths with a granular curve, we focus instead how the amplitude should scale with increasing q and v. We argue that a zigzag moving with constant speed along the direction of motion that is being produced at a constant rate will make an equivalent zigzag with velocities, where it is moving along the x direction with velocity v, at an axial speed q, and moving with horizontal speed w.

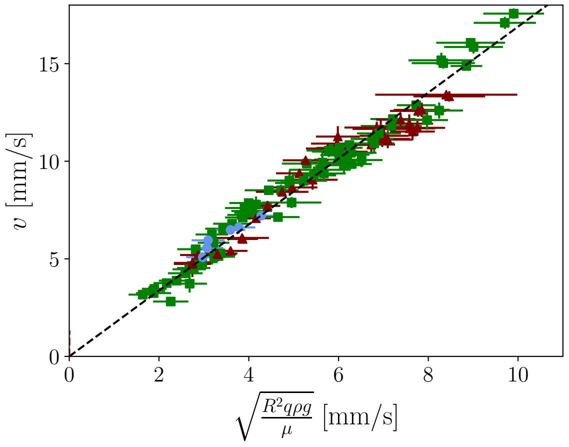

FIG. 3. Dependence of the global chain speed v on the bubble radii R chain productions speed q and the viscosity of the bath μ. Bubble sizes range from $16 < R < 38$ μm, viscosities are indicated by the marker shape with ○ being 1.5 mPa s, □ 1.6 mPa s and △ 2.0 mPa s as measured using Stokes' drag. The black dashed line indicates the relationship described in equation 2 with a single, non-dimensional fit parameter of 1.6889 ± 0.0002.

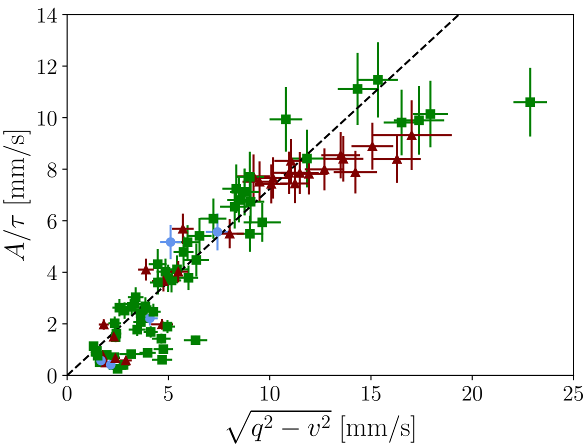

FIG. 4. Dependence of the buckling amplitude A normalized by the characteristic timescale τ on the chain productions speed q and the terminal speed v. Bubble sizes range from $16 < R < 38$ μm, viscosities are indicated by the marker shape with ○ being 1.5 mPa s, □ 1.6 mPa s and △ 2.0 mPa s as measured using Stokes' law. The black dashed line indicates the relationship described in equation 3 with a slope of 0.723 ± 0.001.

While q and v are both quantities that we can measure in our experiment, where w is not. We assert that $w \propto A/\tau$, where $\tau \propto R\Delta\rho g/\mu$ is a characteristic timescale determined by Stokes' Law, using similar arguments as in the discussion for the buckling onset calculation. Converting the lengths to velocities, we find that the amplitude is related to the two relevant velocities in this system,

$$\left(\frac{A}{\tau}\right) \sim \sqrt{q^2 - v^2} \tag{3}$$

We find that the buckling amplitude A per characteristic time τ follows a relationship that depends on the difference in the chain production speed q and terminal speed v. This relationship is shown in figure 4. We see that for a variety of bubble sizes, chain speeds and production speeds the experimentally obtained amplitude closely agrees with the predicted relationship in equation 3. At large differences between the production speeds and chain speeds we see a deviation from the predicted theory, indicating that there is unaccounted non-linear behaviour at the largest amplitudes.

To conclude, we have studied the buckling instability that a slender chain of bubbles undergoes when travelling through a viscous bath. The instability arises when a compressive force due to an imbalance in buoyant forces to drag force acting along the axial direction exceeds the amount force required to move one bubble out of the line of the chain, which is equal to the Stokes' drag on a bubble. Because only hydrodynamic drag serves to stabilize the vertical chain buckling happens over a small length-scale, relative to the length of the chain, directly after the bubbles are extruded. After the buckles are formed, the chain moves as a ribbon through the bath and the terminal velocity can be calculated using a simple balance between buoyancy and drag. The predicted terminal velocities agree extremely well with experiment values. Finally, we have predicted the amplitude of the buckles based on the speed that the bubbles are produced relative to the terminal speed of the chain. We have studied a system that shows buckling just like many other familiar systems, like honey coiling on toast or the coiling of a tendril of a cucumber vine when growing into a boundary. Unlike other systems in which buckling is opposed by either bending energy or viscous dissipation, this is the first study to our knowledge that examines the onset of drag-induced buckling with only viscous drag external to the structure to stabilize the formation.

ACKNOWLEDGMENTS

C.L.L. and K.D.-V. acknowledge financial support from the Natural Science and Engineering Research Council of Canada. C.L.L. acknowledges funding from the Vanier Canada Graduate Scholarship.

[1] L. Mahadevan and J. B. Keller, Coiling of flexible ropes, Proceedings of the Royal Society of London. Series A: Mathematical, Physical and Engineering Sciences **452**, 1679 (1996).

[2] M. K. Jawed, F. Da, J. Joo, E. Grinspun, and P. M. Reis, Coiling of elastic rods on rigid substrates, Proceedings of the National Academy of Sciences **111**, 14663 (2014).

[3] J. Gray and G. J. Hancock, The propulsion of sea-urchin spermatozoa, J Exp Biol **32**, 802 (1955).

[4] A. T. Chwang and T. Y. Wu, A note on the helical movement of micro-organisms, Proceedings of the Royal Society of London. Series B. Biological Sciences **178**, 327 (1971).

[5] O. du Roure, A. Lindner, E. N. Nazockdast, and M. J. Shelly, Dynamics of flexible fibers in viscous flows and fluids, Annual Review of Fluid Mechanics **51**, 539 (2019).

[6] E. M. Purcell, The efficiency of propulsion by a rotating flagellum, Proceedings of the National Academy of Sciences **94**, 11307 (1997).

[7] J. Miller, T. Su, E. D. V., J. Pabon, N. Wicks, K. Bertoldi, and P. Reis, Buckling-induced lock-up of a slender rod injected into a horizontal cylinder, International Journal of Solids and Structures **72**, 153 (2015).

[8] M. Skorobogatiy and L. Mahadevan, Folding of viscous sheets and filaments, Europhysics Letters **52**, 532 (2000).

[9] N. M. Ribe, M. Habibi, and D. Bonn, Stability of liquid rope coiling, Physics of Fluids **18**, 084102 (2006).

[10] G. Barnes and R. Woodcock, Liquid rope-coil effect, American Journal of Physics **26**, 205 (1958).

[11] A. Chakrabarti, S. Al-Mosleh, and L. Mahadevan, Instabilities and patterns in a submerged jelling jet, Soft Matter **17**, 9745 (2021).

[12] M. Habibi, S. H. Hosseini, M. H. Khatami, and N. M. Ribe, Liquid supercoiling, Physics of Fluids **26**, 1 (2014).

[13] N. M. Ribe, H. E. Huppert, M. A. Hallworth, M. Habibi, and D. Bonn, Multiple coexisting states of liquid rope coiling, Journal of Fluid Mechanics **555**, 275 (2006).

[14] L. Mahadevan, W. S. Ryu, and A. D. Samuel, Fluid 'rope trick' investigated, Nature **392**, 140 (1998).

[15] N. M. Ribe, Coiling of viscous jets, Proceedings of the Royal Society of London. Series A: Mathematical, Physical and Engineering Sciences **460**, 3223 (2004).

[16] F. P. Gosselin, P. Neetzow, and M. Paak, Buckling of a beam extruded into highly viscous fluid, Phys. Rev. E **90**, 052718 (2014).

[17] I. Mehdipour, H. Atahan, N. Neithalath, M. Bauchy, E. Garboczi, and G. Sant, How clay particulates affect flow cessation and the coiling stability of yield stress-matched cementing suspensions, Soft Matter **16**, 3929 (2020).

[18] J. K. Nunes, H. Constantin, and H. A. Stone, Microfluidic tailoring of the two-dimensional morphology of crimped microfibers, Soft Matter **9**, 4227 (2013).

[19] K. H. Y., M. Lee, K. J. Park, S. Kim, and L. Mahadevan, Nanopottery: Coiling of electrospun polymer nanofibers, Nano Letters **10**, 2138 (2010).

[20] P.-T. Brun, B. Audoly, N. M. Ribe, T. Eaves, and J. R. Lister, Liquid ropes: A geometrical model for thin viscous jet instabilities, Physical Review Letters **114**, 10.1103/physrevlett.114.174501 (2015).

[21] M. K. Jawed, P.-T. Brun, and P. M. Reis, A geometric model for the coiling of an elastic rod deployed onto a moving substrate, Journal of Applied Mechanics **82**, 10.1115/1.4031363 (2015).

[22] Q. Liu and K. K. Parker, A viscoelastic beam theory of polymer jets with application to rotary jet spinning, Extreme Mechanics Letters **25**, 37 (2018).

[23] T. Han, D. H. Reneker, and A. L. Yarin, Buckling of jets in electrospinning, Polymer **48**, 6064 (2007).

[24] J.-C. O. dit Biot, T. Lorand, and K. Dalnoki-Veress, Continuum model applied to granular analogs of droplets and puddles, Physical Review Letters **125**, 10.1103/physrevlett.125.228001 (2020).

[25] T. Tate, On the magnitude of a drop of liquid formed under different circumstances, The London, Edinburgh, and Dublin Philosophical Magazine and Journal of Science **27**, 176 (1864).

[26] J. Yuan, Y. Li, N. Wang, Y. Cheng, and X. Chen, Effect of orifice diameter on bubble generation process in melt gas injection to prepare aluminum foams, Metallurgical and Materials Transactions B **47**, 1649 (2016).

[27] B. Huner and R. G. Hussey, Cylinder drag at low reynolds number, The Physics of Fluids **20**, 1211 (1977).

[28] T. J. Ui, R. G. Hussey, and R. P. Roger, Stokes drag on a cylinder in axial motion, The Physics of Fluids **27**, 787 (1984).

[29] Y. Ruiz-Morales and A. Romero-Martínez, Coarse-grain molecular dynamics simulations to investigate the bulk viscosity and critical micelle concentration of the ionic surfactant sodium dodecyl sulfate (SDS) in aqueous so-

lution, The Journal of Physical Chemistry B **122**, 3931 (2018).

Chapter 7

Conclusions

The work presented in this thesis focuses on the motion of drops and bubbles. First, I presented work on capillary driven flow of oil droplets on conical fibers. Many different aspects of this system were studied, including the motion of single droplets, the formation and interaction of multiple droplets and the coating film deposited when the droplets move along the fiber. I also presented a study on the buckling of a 'granular' chain of air bubbles. All of these systems are governed by hydrodynamics with slow laminar flow.

The first paper (Chapter 3) in this thesis studies the spontaneous motion of a silicone oil droplet on a conical fiber. The silicone oil totally wets the glass fiber, causing the oil to move to maximize the contact with the glass, and thus travels toward the base of the fiber. In this system, capillarity drives motion, and viscous dissipation opposes it. By balancing the driving and resisting forces, the speed of the droplet is modelled as a function of droplet size, fiber geometry, liquid viscosity, and surface tension. In this study, we tracked the speed of the droplets in experiment and compared with the predicted speed from the simple surface tension based model. In addition, by sampling a large number of droplet sizes and fiber radii, we experimentally confirmed the relationship between droplet height and fiber radius for a droplet in equilibrium, as predicted by Carroll in 1976 [78].

In an extension of the geometry in explored in the first paper, in Chapter 4 the conical fiber geometry was studied with multiple droplets on the same fiber. In nature, it is rare for a single droplet to be present, and typically multiple droplets will coat a slender structure. Here, the break up of a fluid film coating a conical fiber is studied. It is found that break up follows the wavelength predicted by the Plateau-Rayleigh instability. As a result, droplet formation cascades from the tip to the base of the fiber. In addition, thicker films created satellite droplets which appear between large principal droplets. According to the theory for single droplet motion, larger droplets have a greater driving force than smaller droplets, causing large droplets to move more quickly and catch up with the smaller ones. The large and small droplets merge together where a bridge forms between the two. Due to Laplace pressure gradients between the two drops, flow will continue until the two drops combine into one. We studied the merging of the droplets using a combination of numerical simulation and experiment. The dynamics was tracked by measuring the height of the bridge between the two merging droplets. This is the first work that combines the different aspects of film break up and droplet merging of barrel-shaped droplets in a conical geometry.

The third paper, contained in Chapter 5, is a continuation of the same conical fiber geometry. However instead studying the droplet, we chose to study the film of fluid that the droplet leaves behind. Silicone oil droplets were placed on a glass conical fiber and the deposited film shape and thickness was recorded for several droplets. We matched our results to standard Landau-Levich-Derjaguin (LLD) film deposition theory and found for large droplets, relative to the fiber radius, the length scale that sets the thickness of the film matches LLD theory for a fiber pulled from an infinite bath. However for small droplets, the curvature of the droplet affects the film deposition. This paper is the first work to our knowledge that considers a LLD film deposited from a curved, self-propelled reservoir.

In the final paper (Chapter 6), we move to study micron-scale air bubbles that are attached in a chain. The chain is produced faster than hydrodynamic drag allows the bubbles to move upwards through the bath, which creates a compression along the axial direction of the chain. The bubble chain buckles in a regular pattern as a result of the compression. We found that the buckling of the chain was induced by hydrodynamic drag in the axial direction but also stabilized by drag in the transverse direction. This system has many analogs to coiling of solid and viscous ropes.

There are many possible extensions to the droplet on conical fiber projects.

Recent work by Jeong *et al.* involves sorting particles using dipcoating [130]. By pulling the fiber at different speeds from a bidisperse particle-laden bath, the authors found that depending on the dipcoating speed, and thus the film thickness, particles could preferentially be entrained based on particle size. Using this phenomenon, there are several interesting applications to the conical fiber system with regards to passive coating and patterning. For example, an oil droplet laden with particles moving on a fiber may deposit particles only at certain locations along the fiber. There is also an interesting extension regarding particle deposition during the break up of a film on a fiber. As a particle-laden film breaks up into droplets, particles may migrate toward the drop and may pose the question of where the particles would preferentially deposit on a fiber.

Other questions that are still present in the conical fiber system are regarding dissipation. In this thesis, care was taken to only consider droplets that totally wet the fiber substrate; however, a partially wetting droplet would experience dissipation along the contact line, in addition to viscous dissipation. The droplet motion may serve as another tool to measure dissipation of contact lines. For instance, a fiber could be coated in an elastomeric material and the change in droplet motion can provide insight into the dissipation caused by elastic wetting ridges. Elastocapillarity and dissipation during flow due to elastic wetting ridges is a current hot topic in soft matter physics [131, 132].

Finally, the buckled chain of bubbles system can be explored further. An unexplored avenue at this time is to study how a bubble chain buckles as it impacts a boundary, which would be an interesting geometry to use to push the limits of the granular rope analogy. If the analogy holds, one might expect to see coiling, like a solid rope impacting a surface, one might expect that adhesion strength between bubbles becomes important. In addition, it would be interesting to do a similar experiment as the one presented in this thesis, but using a viscoelastic bath, rather than a Newtonian fluid. Since the buckling is a direct probe of the hydrodynamics in the system, the way a bubble chain buckles in a viscoelastic bath might have interesting properties. It is not clear if the buckling will be amplified or suppressed in the presence of the elasticity.

As has been shown in this thesis, the motion of droplets and bubbles are an excellent tool to study hydrodynamics systems. In the systems I studied that are inspired by nature, we see a richness of phenomena that still have so much more to be explored.

Appendix A

Papers not included in this thesis

The following papers consist of studies and work that I have been involved in but are not included as the core papers of my thesis. Two papers were conducted in collaboration with a behavioural ecologist, Dr. Grant Doering, to study the dynamic behaviour of small colonies of ants. Specific species of ants exhibit rhythmic cycles in colony activity, meaning there are periods of time where the majority of ants in the colony are inactive, followed by periods of high activity. Paper A1 studies quantifying and modelling the activity cycles for a variety of species and colonies using an agent-based model. I was not the main contributor to this study, my contribution was in discussing the agent-based model and in reviewing and editing the manuscript. Paper A2 studies the same system of ants, but in this manuscript, we studied one of the possible evolutionary reasons for the activity cycles through the study of spatial inaccessibility. Here, we considered the inactive ants as an obstacle for the active ants when doing tasks around the nest, like tending brood. We found that the introduction of activity cycles decreased the inaccessible areas in the nest. I wrote the original code for the agent-based simulation and contributed to the manuscript editing and review. The final paper, Paper A3, is a discussion regarding the equity, diversity and inclusion work I have been contributing to during my tenure at McMaster University. We outline the work done by graduate students in the department in regards improving the environment for underrepresented groups in physics and astronomy.

A1 Paper 1

Noise resistant synchronization and collective rhythm switching in a model of animal group locomotion

G. N. Doering, B. Drawert, C. L. Lee, J. N. Pruitt, L. R. Petzold and K. Dalnoki-Veress R. Soc. Open. Sci. 9(3), (2022), 211908. https://doi.org/10.1098/rsos.211908

A2 Paper 2

Synchronized locomotion can improve spatial accessibility inside ant colonies

G. N. Doering, C. L. Lee, K. Dalnoki-Veress, submitted.

A3 Paper 3

Equity, Diversity, and Inclusion: A Graduate Student Perspective

S. Dawson, C. Lee, W. Kirkby, J. Wightman and R. Pillsworth Physics in Canada 77(1) (2021), 24-25. https://pic-pac.cap.ca/index.php/Issues/showpdf/article/v77n1.0-a4137.pdf

Bibliography

[1] R. A. Jones. *Soft condensed matter*. Vol. 6. Oxford University Press, 2002.

[2] M. Scheel, R. Seemann, M. Brinkmann, M. D. Michiel, A. Sheppard, B. Breidenbach, and S. Herminghaus. Morphological clues to wet granular pile stability. *Nature Materials* 7(3) (Feb. 2008), 189–193. DOI: 10.1038/nmat2117.

[3] D. J. Hornbaker, R. Albert, I. Albert, A.-L. Barabási, and P. Schiffer. What keeps sandcastles standing? *Nature* 387(6635) (June 1997), 765–765. DOI: 10.1038/42831.

[4] P. A. Rühs, J. Bergfreund, P. Bertsch, S. J. Gstöhl, and P. Fischer. Complex fluids in animal survival strategies. *Soft Matter* 17(11) (2021), 3022–3036. DOI: 10.1039/d1sm00142f.

[5] B. Chan, N. J. Balmforth, and A. E. Hosoi. Building a better snail: Lubrication and adhesive locomotion. *Physics of Fluids* 17(11) (Nov. 2005), 113101. DOI: 10.1063/1.2102927.

[6] Q. Wang, X. Yao, H. Liu, D. Quéré, and L. Jiang. Self-removal of condensed water on the legs of water striders. *Proceedings of the National Academy of Sciences* 112(30) (July 2015), 9247–9252. DOI: 10.1073/pnas.1506874112.

[7] Y.-T. Cheng and D. E. Rodak. Is the lotus leaf superhydrophobic? *Applied Physics Letters* 86(14) (Apr. 2005), 144101. DOI: 10.1063/1.1895487.

[8] D. Quéré and M. Reyssat. Non-adhesive lotus and other hydrophobic materials. *Philosophical Transactions of the Royal Society A: Mathematical, Physical and Engineering Sciences* 366(1870) (Jan. 2008), 1539–1556. DOI: 10.1098/rsta.2007.2171.

[9] S. Haefner, O. Bäumchen, and K. Jacobs. Capillary droplet propulsion on a fibre. *Soft Matter* 11(35) (2015), 6921–6926. DOI: 10.1039/c5sm01228g.

[10] D. Barona and A. Amirfazli. Producing a superhydrophobic paper and altering its repellency through ink-jet printing. *Lab on a Chip* 11(5) (2011), 936. DOI: 10.1039/c0lc00335b.

[11] K. Zhang, K. Fang, M. N. Bukhari, R. Xie, Y. Song, Z. Tang, and X. Zhang. The effect of ink drop spreading and coalescing on the image quality of printed cotton fabric. *Cellulose* 27(16) (Sept. 2020), 9725–9736. DOI: 10.1007/s10570-020-03446-6.

[12] T. Xu, Y. Lin, M. Zhang, W. Shi, and Y. Zheng. High-Efficiency Fog Collector: Water Unidirectional Transport on Heterogeneous Rough Conical Wires. *ACS Nano* 10(12) (Oct. 2016), 10681–10688. DOI: 10.1021/acsnano.6b05595.

[13] X. Tan, T. Shi, Z. Tang, B. Sun, L. Du, Z. Peng, and G. Liao. Investigation of Fog Collection on Cactus-inspired Structures. *Journal of Bionic Engineering* 13(3) (Sept. 2016), 364–372. DOI: 10.1016/s1672-6529(16)60309-8.

[14] J. Ju, H. Bai, Y. Zheng, T. Zhao, R. Fang, and L. Jiang. A multi-structural and multi-functional integrated fog collection system in cactus. *Nature Communications* 3(1) (Jan. 2012). DOI: 10.1038/ncomms2253.

[15] J. D. Paulsen, V. Démery, C. D. Santangelo, T. P. Russell, B. Davidovitch, and N. Menon. Optimal wrapping of liquid droplets with ultrathin sheets. *Nature Materials* 14(12) (Aug. 2015), 1206–1209. DOI: 10.1038/nmat4397.

[16] P. M. Reis, J. Hure, S. Jung, J. W. M. Bush, and C. Clanet. Grabbing water. *Soft Matter* 6(22) (2010), 5705. DOI: 10.1039/c0sm00895h.

[17] C. Py, P. Reverdy, L. Doppler, J. Bico, B. Roman, and C. N. Baroud. Capillary Origami: Spontaneous Wrapping of a Droplet with an Elastic Sheet. *Physical Review Letters* 98(15) (Apr. 2007). DOI: 10.1103/physrevlett.98.156103.

[18] A. Antkowiak, B. Audoly, C. Josserand, S. Neukirch, and M. Rivetti. Instant fabrication and selection of folded structures using drop impact. *Proceedings of the National Academy of Sciences* 108(26) (June 2011), 10400–10404. DOI: `10.1073/pnas.1101738108`.

[19] A. Fortais, K. Charlesworth, R. D. Schulman, and K. Dalnoki-Veress. Spontaneous Elastocapillary Winding of Thin Elastic Fibers in Contact with Bubbles. *Physical Review Letters* 127(21) (Nov. 2021). DOI: `10.1103/physrevlett.127.218001`.

[20] H. Elettro, F. Vollrath, A. Antkowiak, and S. Neukirch. Drop-on-coilable-fibre systems exhibit negative stiffness events and transitions in coiling morphology. *Soft Matter* 13(33) (2017), 5509–5517. DOI: `10.1039/c7sm00368d`.

[21] R. D. Schulman, A. Porat, K. Charlesworth, A. Fortais, T. Salez, E. Raphaël, and K. Dalnoki-Veress. Elastocapillary bending of microfibers around liquid droplets. *Soft Matter* 13(4) (2017), 720–724. DOI: `10.1039/c6sm02095j`.

[22] A. Sauret, F. Boulogne, K. Somszor, E. Dressaire, and H. A. Stone. Drop morphologies on flexible fibers: influence of elastocapillary effects. *Soft Matter* 13(1) (2017), 134–140. DOI: `10.1039/c6sm00921b`.

[23] A. Keiser, L. Keiser, C. Clanet, and D. Quéré. Drop friction on liquid-infused materials. *Soft Matter* 13(39) (2017), 6981–6987. DOI: `10.1039/c7sm01226h`.

[24] N. Savva and S. Kalliadasis. Droplet motion on inclined heterogeneous substrates. *Journal of Fluid Mechanics* 725 (May 2013), 462–491. DOI: `10.1017/jfm.2013.201`.

[25] D. J. Acheson. *Elementary fluid dynamics*. Oxford University Press, 1990.

[26] A. M. Jaffe. The millennium grand challenge in mathematics. *Notices of the AMS* 53(6) (2006), 652–660.

[27] R. D. Knight. *Physics for scientists and engineers*. Pearson Higher Ed., 2017.

[28] A. Thorley and C. Tiley. Unsteady and transient flow of compressible fluids in pipelines—a review of theoretical and some experimental studies. *International Journal of Heat and Fluid Flow* 8(1) (Mar. 1987), 3–15. DOI: `10.1016/0142-727x(87)90044-0`.

[29] J. M. Weiss and W. A. Smith. Preconditioning applied to variable and constant density flows. *AIAA Journal* 33(11) (Nov. 1995), 2050–2057. DOI: `10.2514/3.12946`.

[30] S.-I. Pai. *Theoretical Computational Dynamics*. Chapman and Hall/CRC, Nov. 2020. DOI: `10.1201/9781003062158`.

[31] R. Clift, J. R. Grace, and M. E. Weber. *Bubbles, drops, and particles*. Academic Press, Inc., 1978.

[32] J. K. Nunes, H. Constantin, and H. A. Stone. Microfluidic tailoring of the two-dimensional morphology of crimped microfibers. *Soft Matter* 9(16) (2013), 4227. DOI: `10.1039/c3sm27579e`.

[33] J. T. Pham, A. Morozov, A. J. Crosby, A. Lindner, and O. du Roure. Deformation and shape of flexible, microscale helices in viscous flow. *Physical Review E* 92(1) (July 2015). DOI: `10.1103/physreve.92.011004`.

[34] P.-G. De Gennes, F. Brochard-Wyart, D. Quéré, et al. *Capillarity and wetting phenomena: drops, bubbles, pearls, waves*. Vol. 315. Springer, 2004.

[35] A. Oron, S. H. Davis, and S. G. Bankoff. Long-scale evolution of thin liquid films. *Rev. Mod. Phys.* 69 (3 July 1997), 931–980. DOI: `10.1103/RevModPhys.69.931`.

[36] N. Y. Lin, B. M. Guy, M. Hermes, C. Ness, J. Sun, W. C. Poon, and I. Cohen. Hydrodynamic and Contact Contributions to Continuous Shear Thickening in Colloidal Suspensions. *Physical Review Letters* 115(22) (Nov. 2015). DOI: `10.1103/physrevlett.115.228304`.

[37] H. Nakamura, S. Makino, and M. Ishii. Continuous shear thickening and discontinuous shear thickening of concentrated monodispersed silica slurry. *Advanced Powder Technology* 31(4) (Apr. 2020), 1659–1664. DOI: `10.1016/j.apt.2020.01.032`.

[38] B. Huner and R. G. Hussey. Cylinder drag at low Reynolds number. *Physics of Fluids* 20(8) (1977), 1211. DOI: 10.1063/1.862001.

[39] T. J. Ui, R. G. Hussey, and R. P. Roger. Stokes drag on a cylinder in axial motion. *Physics of Fluids* 27(4) (1984), 787. DOI: 10.1063/1.864706.

[40] J. Gray and G. J. Hancock. The Propulsion of Sea-Urchin Spermatozoa. *Journal of Experimental Biology* 32(4) (Dec. 1955), 802–814. DOI: 10.1242/jeb.32.4.802.

[41] J. D. McGraw, N. M. Jago, and K. Dalnoki-Veress. Capillary levelling as a probe of thin film polymer rheology. *Soft Matter* 7(17) (2011), 7832. DOI: 10.1039/c1sm05261f.

[42] J. D. McGraw, T. Salez, O. Bäumchen, E. Raphaël, and K. Dalnoki-Veress. Self-Similarity and Energy Dissipation in Stepped Polymer Films. *Physical Review Letters* 109(12) (Sept. 2012). DOI: 10.1103/physrevlett.109.128303.

[43] V. Bertin, C. L. Lee, T. Salez, E. Raphaël, and K. Dalnoki-Veress. Capillary levelling of immiscible bilayer films. *Journal of Fluid Mechanics* 911 (Jan. 2021). DOI: 10.1017/jfm.2020.1045.

[44] A. Liu, Y. Yao, J. Yao, and T. Liu. Droplet Spreading Induced Wrinkling and Its Use for Measuring the Elastic Modulus of Polymeric Thin Films. *Macromolecules* 55(10) (May 2022), 3877–3885. DOI: 10.1021/acs.macromol.2c00345.

[45] Y. Timounay, A. R. Hartwell, M. He, D. E. King, L. K. Murphy, V. Démery, and J. D. Paulsen. Sculpting Liquids with Ultrathin Shells. *Physical Review Letters* 127(10) (Sept. 2021). DOI: 10.1103/physrevlett.127.108002.

[46] C. Henkel, J. H. Snoeijer, and U. Thiele. Gradient-dynamics model for liquid drops on elastic substrates. *Soft Matter* 17(45) (2021), 10359–10375. DOI: 10.1039/d1sm01032h.

[47] D. J. Srolovitz and S. A. Safran. Capillary instabilities in thin films. I. Energetics. *Journal of Applied Physics* 60(1) (July 1986), 247–254. DOI: 10.1063/1.337689.

[48] S. J. Leib and M. E. Goldstein. The generation of capillary instabilities on a liquid jet. *Journal of Fluid Mechanics* 168(1) (July 1986), 479. DOI: 10.1017/s0022112086000472.

[49] K. C. Chaudhary and T. Maxworthy. The nonlinear capillary instability of a liquid jet. Part 3. Experiments on satellite drop formation and control. *Journal of Fluid Mechanics* 96(2) (Jan. 1980), 287–297. DOI: 10.1017/s0022112080002121.

[50] M. V. Berry. The molecular mechanism of surface tension. *Physics Education* 6(2) (Mar. 1971), 79–84. DOI: 10.1088/0031-9120/6/2/001.

[51] A. Marchand, J. H. Weijs, J. H. Snoeijer, and B. Andreotti. Why is surface tension a force parallel to the interface? *American Journal of Physics* 79(10) (Oct. 2011), 999–1008. DOI: 10.1119/1.3619866.

[52] S. Das, A. Marchand, B. Andreotti, and J. H. Snoeijer. Elastic deformation due to tangential capillary forces. *Physics of Fluids* 23(7) (July 2011), 072006. DOI: 10.1063/1.3615640.

[53] J. Gerber, T. Lendenmann, H. Eghlidi, T. M. Schutzius, and D. Poulikakos. Wetting transitions in droplet drying on soft materials. *Nature Communications* 10(1) (Oct. 2019). DOI: 10.1038/s41467-019-12093-w.

[54] G. McHale, N. J. Shirtcliffe, S. Aqil, C. C. Perry, and M. I. Newton. Topography Driven Spreading. *Physical Review Letters* 93(3) (July 2004). DOI: 10.1103/physrevlett.93.036102.

[55] A. W. Adamson, A. P. Gast, et al. *Physical chemistry of surfaces*. Vol. 150. Interscience publishers New York, 1967.

[56] I. Klenk and P. Grathwohl. Transverse vertical dispersion in groundwater and the capillary fringe. *Journal of Contaminant Hydrology* 58(1-2) (Sept. 2002), 111–128. DOI: 10.1016/s0169-7722(02)00011-6.

[57] M. I. Haque. *Mechanics of groundwater in porous media*. CRC Press, Taylor & Francis Group, 2015.

[58] I. P. Pavlova, S. S. Nair, N. Kyprianou, and A. K. Tewari. The Rapid Coronavirus Antibody Test: Can We Improve Accuracy? *Frontiers in Medicine* 7 (Sept. 2020). DOI: 10.3389/fmed.2020.00569.

[59] T. L. van Neel and A. B. Theberge. Programmable capillary action controls fluid flows. *Nature* 595(7865) (June 2021), 31–32. DOI: 10.1038/d41586-021-01708-2.

[60] W. R. Gardner and C. F. Ehlig. The influence of soil water on transpiration by plants. *Journal of Geophysical Research* 68(20) (Oct. 1963), 5719–5724. DOI: 10.1029/jz068i020p05719.

[61] W. Tanner and H. Beevers. Transpiration, a prerequisite for long-distance transport of minerals in plants? *Proceedings of the National Academy of Sciences* 98(16) (July 2001), 9443–9447. DOI: 10.1073/pnas.161279898.

[62] M. Maleki, E. Reyssat, D. Quéré, and R. Golestanian. On the Landau-Levich Transition. *Langmuir* 23(20) (Aug. 2007), 10116–10122. DOI: 10.1021/la700822y.

[63] J. E. Seebergh and J. C. Berg. Dynamic wetting in the low capillary number regime. *Chemical Engineering Science* 47(17-18) (Dec. 1992), 4455–4464. DOI: 10.1016/0009-2509(92)85123-s.

[64] S. Reddy, P. R. Schunk, and R. T. Bonnecaze. Dynamics of low capillary number interfaces moving through sharp features. *Physics of Fluids* 17(12) (Dec. 2005), 122104. DOI: 10.1063/1.2140691.

[65] J. D. Berry, M. J. Neeson, R. R. Dagastine, D. Y. Chan, and R. F. Tabor. Measurement of surface and interfacial tension using pendant drop tensiometry. *Journal of Colloid and Interface Science* 454 (Sept. 2015), 226–237. DOI: 10.1016/j.jcis.2015.05.012.

[66] C. E. Stauffer. The Measurement of Surface Tension by the Pendant Drop Technique. *The Journal of Physical Chemistry* 69(6) (June 1965), 1933–1938. DOI: 10.1021/j100890a024.

[67] D. Staicopolus. The computation of surface tension and of contact angle by the sessile-drop method. *Journal of Colloid Science* 17(5) (June 1962), 439–447. DOI: 10.1016/0095-8522(62)90055-7.

[68] R. Tadmor and P. S. Yadav. As-placed contact angles for sessile drops. *Journal of Colloid and Interface Science* 317(1) (Jan. 2008), 241–246. DOI: 10.1016/j.jcis.2007.09.029.

[69] F. Heslot, N. Fraysse, and A. M. Cazabat. Molecular layering in the spreading of wetting liquid drops. *Nature* 338(6217) (Apr. 1989), 640–642. DOI: 10.1038/338640a0.

[70] J. R. Hernandez-Aguilar, R. Cunningham, and J. A. Finch. A test of the Tate equation to predict bubble size at an orifice in the presence of frother. *International Journal of Mineral Processing* 79(2) (May 2006), 89–97. DOI: 10.1016/j.minpro.2005.12.003.

[71] J. Yuan, Y. Li, N. Wang, Y. Cheng, and X. Chen. Effect of Orifice Diameter on Bubble Generation Process in Melt Gas Injection to Prepare Aluminum Foams. *Metallurgical and Materials Transactions B* 47(3) (Mar. 2016), 1649–1660. DOI: 10.1007/s11663-016-0638-5.

[72] A. C. Alfaro. Byssal attachment of juvenile mussels, Perna canaliculus, affected by water motion and air bubbles. *Aquaculture* 255(1-4) (May 2006), 357–361. DOI: 10.1016/j.aquaculture.2005.11.059.

[73] T. Gilet, D. Terwagne, and N. Vandewalle. Droplets sliding on fibres. *The European Physical Journal E* 31(3) (Mar. 2010), 253–262. DOI: 10.1140/epje/i2010-10563-9.

[74] H.-J. Butt, K. Graf, and M. Kappl. *Physics and Chemistry of Interfaces*. Wiley, Sept. 2003. DOI: 10.1002/3527602313.

[75] C. G. Viejo, D. D. Torrico, F. R. Dunshea, and S. Fuentes. Bubbles, Foam Formation, Stability and Consumer Perception of Carbonated Drinks: A Review of Current, New and Emerging Technologies for Rapid Assessment and Control. *Foods* 8(12) (Nov. 2019), 596. DOI: 10.3390/foods8120596.

[76] R. Zenit and J. Rodrıguez-Rodrıguez. The fluid mechanics of bubbly drinks. *Physics Today* 71(11) (Nov. 2018), 44–50. DOI: 10.1063/pt.3.4069.

[77] P.-B. Bintein, H. Bense, C. Clanet, and D. Quéré. Self-propelling droplets on fibres subject to a crosswind. *Nature Physics* 15(10) (Aug. 2019), 1027–1032. DOI: 10.1038/s41567-019-0599-0.

[78] B. Carroll. The accurate measurement of contact angle, phase contact areas, drop volume, and Laplace excess pressure in drop-on-fiber systems. *Journal of Colloid and Interface Science* 57(3) (Dec. 1976), 488–495. DOI: 10.1016/0021-9797(76)90227-7.

[79] A. B. Kostinski and R. A. Shaw. Raindrops large and small. *Nature Physics* 5(9) (Sept. 2009), 624–625. DOI: 10.1038/nphys1385.

[80] T. Sanada, M. Watanabe, T. Fukano, and A. Kariyasaki. Behavior of a single coherent gas bubble chain and surrounding liquid jet flow structure. *Chemical Engineering Science* 60(17) (Sept. 2005), 4886–4900. DOI: 10.1016/j.ces.2005.04.010.

[81] N. M. Aybers and A. Tapucu. The motion of gas bubbles rising through stagnant liquid. *Wärme- und Stoffübertragung* 2(2) (June 1969), 118–128. DOI: 10.1007/bf01089056.

[82] J. Lee and H. Park. Flow induced by the single-bubble chain depending on the bubble release frequency. *Physics of Fluids* 34(3) (Mar. 2022), 033312. DOI: 10.1063/5.0083281.

[83] M. Liu, B. Wang, and L. Tan. Correlation of drag coefficient between rising bubbles in chain. *Physics of Fluids* 34(4) (Apr. 2022), 043314. DOI: 10.1063/5.0088375.

[84] Q. Liu, J. H. Y. Lo, Y. Li, Y. Liu, J. Zhao, and L. Xu. The role of drop shape in impact and splash. *Nature Communications* 12(1) (May 2021). DOI: 10.1038/s41467-021-23138-4.

[85] É. Lorenceau and D. Quéré. Drops on a conical wire. *Journal of Fluid Mechanics* 510 (July 2004), 29–45. DOI: 10.1017/s0022112004009152.

[86] S. I. Tamim and J. B. Bostwick. Plateau–Rayleigh instability in a soft viscoelastic material. *Soft Matter* 17(15) (2021), 4170–4179. DOI: 10.1039/d1sm00019e.

[87] S. Haefner, M. Benzaquen, O. Bäumchen, T. Salez, R. Peters, J. D. McGraw, K. Jacobs, E. Raphaël, and K. Dalnoki-Veress. Influence of slip on the Plateau–Rayleigh instability on a fibre. *Nature Communications* 6(1) (June 2015). DOI: 10.1038/ncomms8409.

[88] T. S. Chan, J. H. Snoeijer, and J. Eggers. Theory of the forced wetting transition. *Physics of Fluids* 24(7) (July 2012), 072104. DOI: `10.1063/1.4736531`.

[89] C. Brinker, G. Frye, A. Hurd, and C. Ashley. Fundamentals of sol-gel dip coating. *Thin Solid Films* 201(1) (June 1991), 97–108. DOI: `10.1016/0040-6090(91)90158-t`.

[90] J. C. Gimel and W. Brown. A light scattering investigation of the sodium dodecyl sulfate-lysozyme system. *The Journal of Chemical Physics* 104(20) (May 1996), 8112–8117. DOI: `10.1063/1.471496`.

[91] W. L. Bragg and J. F. Nye. A dynamical model of a crystal structure. *Proceedings of the Royal Society of London. Series A. Mathematical and Physical Sciences* 190(1023) (1947), 474–481.

[92] W. L. Bragg and W. M. Lomer. A dynamical model of a crystal structure. II. *Proceedings of the Royal Society of London. Series A. Mathematical and Physical Sciences* 196(1045) (Mar. 1949), 171–181. DOI: `10.1098/rspa.1949.0022`.

[93] J.-C. Ono-dit-Biot, T. Lorand, and K. Dalnoki-Veress. Continuum Model Applied to Granular Analogs of Droplets and Puddles. *Physical Review Letters* 125(22) (Nov. 2020). DOI: `10.1103/physrevlett.125.228001`.

[94] S. Takagi and Y. Matsumoto. Surfactant Effects on Bubble Motion and Bubbly Flows. *Annual Review of Fluid Mechanics* 43(1) (Jan. 2011), 615–636. DOI: `10.1146/annurev-fluid-122109-160756`.

[95] K. Holmberg. *Surfactants*. July 2019. DOI: `10.1002/14356007.a25_747.pub2`.

[96] H.-C. Chang, Y.-Y. Lin, C.-S. Chern, and S.-Y. Lin. Determination of Critical Micelle Concentration of Macroemulsions and Miniemulsions. *Langmuir* 14(23) (Oct. 1998), 6632–6638. DOI: `10.1021/la971109w`.

[97] S. Asakura and F. Oosawa. Interaction between particles suspended in solutions of macromolecules. *Journal of Polymer Science* 33(126) (Dec. 1958), 183–192. DOI: `10.1002/pol.1958.1203312618`.

[98] M. Skorobogatiy and L. Mahadevan. Folding of viscous sheets and filaments. *Europhysics Letters (EPL)* 52(5) (Dec. 2000), 532–538. DOI: 10.1209/epl/i2000-00470-4.

[99] J. Miller, T. Su, E. D. V., J. Pabon, N. Wicks, K. Bertoldi, and P. Reis. Buckling-induced lock-up of a slender rod injected into a horizontal cylinder. *International Journal of Solids and Structures* 72 (Oct. 2015), 153–164. DOI: 10.1016/j.ijsolstr.2015.07.025.

[100] I. Mehdipour, H. Atahan, N. Neithalath, M. Bauchy, E. Garboczi, and G. Sant. How clay particulates affect flow cessation and the coiling stability of yield stress-matched cementing suspensions. *Soft Matter* 16(16) (2020), 3929–3940. DOI: 10.1039/c9sm02414j.

[101] M. K. Jawed, P.-T. Brun, and P. M. Reis. A Geometric Model for the Coiling of an Elastic Rod Deployed Onto a Moving Substrate. *Journal of Applied Mechanics* 82(12) (Sept. 2015). DOI: 10.1115/1.4031363.

[102] H.-Y. Kim, M. Lee, K. J. Park, S. Kim, and L. Mahadevan. Nanopottery: Coiling of Electrospun Polymer Nanofibers. *Nano Letters* 10(6) (May 2010), 2138–2140. DOI: 10.1021/nl100824d.

[103] J. L. Campos, L. Urpı, T. Sanmartın, C. Gouyette, and J. A. Subirana. DNA coiled coils. *Proceedings of the National Academy of Sciences* 102(10) (Feb. 2005), 3663–3666. DOI: 10.1073/pnas.0500496102.

[104] F. Tanaka and H. Takahashi. Elastic theory of supercoiled DNA. *The Journal of Chemical Physics* 83(11) (Dec. 1985), 6017–6026. DOI: 10.1063/1.449637.

[105] G. Barnes and R. Woodcock. Liquid Rope-Coil Effect. *American Journal of Physics* 26(4) (Apr. 1958), 205–209. DOI: 10.1119/1.1996110.

[106] N. M. Ribe, M. Habibi, and D. Bonn. Stability of liquid rope coiling. *Physics of Fluids* 18(8) (Aug. 2006), 084102. DOI: 10.1063/1.2336803.

[107] N. M. Ribe, H. E. Huppert, M. A. Hallworth, M. Habibi, and D. Bonn. Multiple coexisting states of liquid rope coiling. *Journal of Fluid Mechanics* 555 (May 2006), 275. DOI: 10.1017/s0022112006009153.

[108] F. P. Gosselin, P. Neetzow, and M. Paak. Buckling of a beam extruded into highly viscous fluid. *Phys. Rev. E* 90(5) (2014), 052718.

[109] A. Chakrabarti, S. Al-Mosleh, and L. Mahadevan. Instabilities and patterns in a submerged jelling jet. *Soft Matter* 17(42) (2021), 9745–9754. DOI: `10.1039/d1sm00517k`.

[110] M. M. Denn. Continuous Drawing of Liquids to Form Fibers. *Annual Review of Fluid Mechanics* 12(1) (Jan. 1980), 365–387. DOI: `10.1146/annurev.fl.12.010180.002053`.

[111] E. Neher and B. Sakmann. The Patch Clamp Technique. *Scientific American* 266(3) (Mar. 1992), 44–51. DOI: `10.1038/scientificamerican0392-44`.

[112] B. G. Kornreich. The patch clamp technique: Principles and technical considerations. *Journal of Veterinary Cardiology* 9(1) (May 2007), 25–37. DOI: `10.1016/j.jvc.2007.02.001`.

[113] J. Shao and R. Hochmuth. Micropipette suction for measuring piconewton forces of adhesion and tether formation from neutrophil membranes. *Biophysical Journal* 71(5) (Nov. 1996), 2892–2901. DOI: `10.1016/s0006-3495(96)79486-9`.

[114] M. Backholm, D. Molpeceres, M. Vuckovac, H. Nurmi, M. J. Hokkanen, V. Jokinen, J. V. I. Timonen, and R. H. A. Ras. Water droplet friction and rolling dynamics on superhydrophobic surfaces. *Communications Materials* 1(1) (Sept. 2020). DOI: `10.1038/s43246-020-00065-3`.

[115] S. Barkley, S. J. Scarfe, E. R. Weeks, and K. Dalnoki-Veress. Predicting the size of droplets produced through Laplace pressure induced snap-off. *Soft Matter* 12(35) (2016), 7398–7404. DOI: `10.1039/c6sm00853d`.

[116] C. T. Kreis, M. L. Blay, C. Linne, M. M. Makowski, and O. Bäumchen. Adhesion of Chlamydomonas microalgae to surfaces is switchable by light. *Nature Physics* 14(1) (Sept. 2017), 45–49. DOI: `10.1038/nphys4258`.

[117] M. Backholm and O. Bäumchen. Micropipette force sensors for in vivo force measurements on single cells and multicellular microorganisms. *Nature Protocols* 14(2) (Jan. 2019), 594–615. DOI: `10.1038/s41596-018-0110-x`.

[118] M. J. Colbert, A. N. Raegen, C. Fradin, and K. Dalnoki-Veress. Adhesion and membrane tension of single vesicles and living cells using a micropipette-based technique. *The European Physical Journal E* 30(2) (Sept. 2009). DOI: 10.1140/epje/i2009-10514-7.

[119] T. Tate. On the magnitude of a drop of liquid formed under different circumstances. *The London, Edinburgh, and Dublin Philosophical Magazine and Journal of Science* 27(181) (Mar. 1864), 176–180. DOI: 10.1080/14786446408643645.

[120] URL: https://scikit-image.org/docs/stable/api/skimage.filters.html#skimage.filters.sobel.

[121] URL: https://docs.scipy.org/doc/scipy/reference/generated/scipy.signal.correlate.html.

[122] A. Papoulis. *The Fourier integral and its applications.* Polytechnic Institute of Brooklyn, McCraw-Hill Book Company Inc., USA, ISBN: 67-048447-3, 1962.

[123] URL: https://scikit-image.org/docs/0.9.x/auto_examples/plot_template.html.

[124] E. Q. Li and S. T. Thoroddsen. The fastest drop climbing on a wet conical fibre. *Physics of Fluids* 25(5) (2013), 052105. DOI: 10.1063/1.4805068.

[125] Y.-E. Liang, H.-K. Tsao, and Y.-J. Sheng. Drops on hydrophilic conical fibers: gravity effect and coexistent states. *Langmuir* 31(5) (2015), 1704–1710. DOI: 10.1021/la504552d.

[126] S. Michielsen, J. Zhang, J. Du, and H. J. Lee. Gibbs free energy of liquid drops on conical fibers. *Langmuir* 27(19) (2011), 11867–11872. DOI: 10.1021/la202952e.

[127] J. McCarthy, D. Vella, and A. A. Castrejón-Pita. Dynamics of droplets on cones: self-propulsion due to curvature gradients. *Soft Matter* 15 (2019), 9997. DOI: 10.1039/c9sm01635j.

[128] M. A. Hack, W. Tewes, Q. Xie, C. Datt, K. Harth, J. Harting, and J. H. Snoeijer. Self-Similar Liquid Lens Coalescence. *Physical Review Letters* 124(19) (May 2020). DOI: 10.1103/physrevlett.124.194502.

[129] J. F. Hernández-Sánchez, L. A. Lubbers, A. Eddi, and J. H. Snoeijer. Symmetric and Asymmetric Coalescence of Drops on a Substrate. *Physical Review Letters* 109(18) (Nov. 2012). DOI: 10.1103/physrevlett.109.184502.

[130] D.-H. Jeong, M. K. H. Lee, V. Thiévenaz, M. Z. Bazant, and A. Sauret. Dip coating of bidisperse particulate suspensions. *Journal of Fluid Mechanics* 936 (Feb. 2022). DOI: 10.1017/jfm.2022.79.

[131] J. Bico, É. Reyssat, and B. Roman. Elastocapillarity: When Surface Tension Deforms Elastic Solids. *Annual Review of Fluid Mechanics* 50(1) (Jan. 2018), 629–659. DOI: 10.1146/annurev-fluid-122316-050130.

[132] B. Andreotti, O. Bäumchen, F. Boulogne, K. E. Daniels, E. R. Dufresne, H. Perrin, T. Salez, J. H. Snoeijer, and R. W. Style. Solid capillarity: when and how does surface tension deform soft solids? *Soft Matter* 12(12) (2016), 2993–2996. DOI: 10.1039/c5sm03140k.